Simulation and Analysis of the Aerodynamic Interactions between Distributed Propellers and Wings

Jan-Sören Fischer

Technische Universiteit Delft

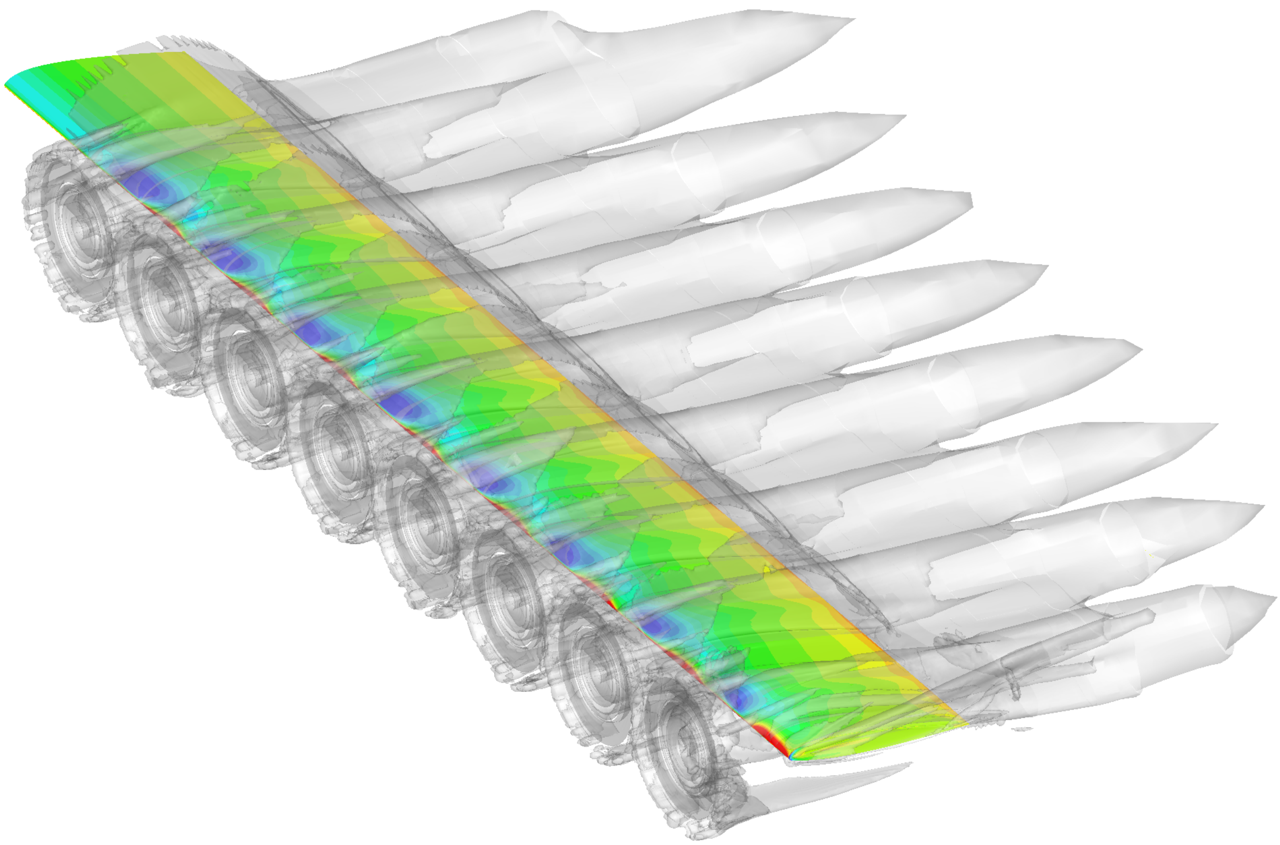

Delft University of Technology

THE FRENCH AEROSPACE LAB

Challenge the future

Simulation and Analysis of the Aerodynamic Interactions between Distributed Propellers and Wings

by

Jan-Sören Fischer

in partial fulfillment of the requirements for the degree of

Master of Science
in Aerospace Engineering

at the Delft University of Technology,
to be defended publicly on Tuesday December 8, 2017 at 01:30 PM.

Student number:	4152638	
Project duration:	February 14, 2017 – December 8, 2017	
Thesis registration nr.:	173#17#MT#FPP	
Supervisor:	Dr. B. Ortun,	ONERA
Thesis committee:	Prof. dr. ir. L. L. M. Veldhuis,	TU Delft
	Dr. ir. M. Voskuijl,	TU Delft
	Dr. ir. A. van Zuijlen,	TU Delft

This thesis is confidential and cannot be made public until December 8, 2017.

Preface

It was with great curiosity that I dived into the world of aerospace engineering after high school in 2011. I knew back then that the studies at TU Delft would be a big challenge in a highly demanding field that could potentially open up many doors in my future life. And this was right in many ways. The university abroad with many other internationals opened up my mind for the diversity in our world. The multidisciplinary nature of the subject taught me how interactive this world is. The studies forced me to develop as a person and asked for more dedication than any other task I had taken on up until then.

My curiosity and motivation for the discipline grew with everything I learned. Partially responsible for this is the great educational system in the Netherlands. The combination of specific engineering knowledge acquisition and continuous application of the theory in team projects taught me everything it takes to be a skilled and effective research engineer. The ability to go into my neighbour country and start studying without big hurdles is something that really initiated my appreciation as a young student towards the European idea. The biggest motivators during the studies, however, were my internships, showing me what my studies enabled me to achieve. In particular, my placement supervisors Arne Seitz (Bauhaus Luftfahrt), Peter Eisenschmidt (Airbus) and Biel Ortun (ONERA) provided me with support, trust and acknowledgement that gave me the necessary ambition and belief in myself to expect a lot from my future career and to take on big challenges in human aviation. For this and the very enjoyable time at their offices, I am very grateful.

This thesis, now, was the final challenge towards the M.Sc. degree. It was an overwhelming experience because the opportunities, responsibilities and hurdles that are inherent even to a small research project are a completely different story compared to course-work or pre-defined tasks during an internship. Despite the difficulties this brings up, the opportunity to manage an own little peace of research and adding to the body of knowledge is very rewarding. Biel was the best supervisor I could have asked for and was always available to support my activities. I would also like to thank Leo Veldhuis for his willingness to act as distant supervisor despite his sabbatical leave to the USA and for his constructive and helpful feedback towards the end of the project. Next to these work-related contributions, the whole H2T team at ONERA Centre Meudon was a great group to work with and I very much enjoyed the discussions as well as the picknicks with Mölky despite my initial troubles with the French language.

During and next to the course-work at university, friends and fellow students made the last 6 years incredibly enjoyable. Especially Jonas and Joris contributed a lot to my success and life in South Holland. Finally, a very big thank you goes to Marie who had a lot of patience with me and always encouraged me to reach for something bigger as well as to my parents, Kai and Doris, who supported me regardless of what I was doing, and by that allowing me to work on my dreams without worries or need to defend my path. Having said that, I now feel well prepared and excited to take on a bigger portion of responsibility and to carry out a larger research project in form of a Ph.D.

Jan-Sören Fischer
Oldenburg, November 2017

Abstract

The recent advances in complementary technologies have given a new impulse in the research activities related to distributed propulsion. Light electric engines, whose performance is rather insensitive to scaling, improved battery capacities and autonomous flight all contribute to this trend. Promising concepts featuring electrically powered distributed propellers along the wings are expected to improve aero-propulsive efficiency, high-lift capability, vertical take-off & landing capability and operating costs.

Problems associated to the exploitation of these benefits are, among others, the many new design freedoms and the associated growing design space. The design space exploration requires new tools that are capable of dealing with lifting surfaces, interacting strongly with multiple propellers. Furthermore, the tool's ability to include viscous and thickness-effects is crucial for understanding and assessing the new vehicle architectures.

The goal of this thesis is twofold and starts with the implementation and validation of a body-force approach to model propellers in a (U)RANS simulation by volumetric source terms. A coupled lifting-line code, being executed in the extracted RANS flowfield, provides the propeller blade forces that are acting on the fluid. The validation is performed by comparing the simulation method on closely coupled propeller-wing configuration with a meshed-propeller URANS simulation. The comparison shows a very good agreement for the two different approaches. A further comparison to an experimental set-up of an over-the-wing propeller provides further confidence in the methods capability of modelling propellers in the close vicinity of a lifting surface.

The second goal is the better understanding of the flow phenomena for selected promising configurations. On the one hand, wing-tip mounted propellers in pusher and tractor arrangements are compared for non-twisted and ideally-twisted wings. The thrust-drag balanced configurations show that the total required shaft power is less for a pusher arrangement in case of a non-twisted wing. For the ideally-twisted wing, the two arrangements are equally good in reducing required shaft power. The tractor arrangements have a wing drag reduction of 10% while the pusher arrangements show an increase in propulsive efficiency of 8-9%. The isolated lifting-line simulations showed that the tool is capable of capturing the trends but that it cannot achieve the accuracy of a viscous analysis.

On the other hand, lift-augmenting propellers have been installed in front of the leading edge as well as on different chord-wise positions over the wing. The over-the-wing installed propellers showed the highest increase in lift coefficient (up to 107%) whilst strongly decreasing wing-drag. A more upstream positioned propeller achieved a higher drag reduction but a downstream positioned propeller showed higher lift augmentation. The leading edge propellers had the highest lift increase (60%) when being contra-rotating. For the high-lift propeller configurations, the lifting-line code was able to capture major trends.

The performed work shows for the first time a viscous analysis on how wing-tip mounted propellers can improve the aero-propulsive efficiency of a configuration and compares trimmed pusher and tractor arrangements. It was further shown, how the new body-force approach can lead to very accurate viscous simulations of distributed propeller-wing configurations with relatively low computational effort.

Contents

List of Figures

List of Tables

NOMENCLATURE

Parameter	Description	Units
A	Area	[m^2]
b	Wing span/body force	[m]/[N]
c	Chord length/Weibull shape parameter	[m]/[-]
C_D	Drag coefficient	[-]
C_L	Lift coefficient	[-]
C_M	Moment coefficient	[-]
C_p	Pressure coefficient	[-]
C_P	Power coefficient	[-]
C_p	Pressure coefficient	[-]
C_T	Thrust coefficienct	[-]
D	Diameter/drag	[m]/[N]
E	Energy	[J]
e	Internal energy	[J]
F	Resultant force	[N]
F_N	Net thrust	[N]
F_y	Horizontal propeller in-plane load	[N]
F_z	Vertical propeller in-plane load	[N]
g	Gravitational acceleration	[m/s^2]
J	Advance ratio	[-]
k	External energy/factor	[J]/[-]
L	Lift	[N]
M	Mach number	[-]
m	Mass	[kg]
n	Number/number of rotations per time/normal vector	[-]/[1/s]/[-]
N	Number	[-]
P	Power/Pressure	[W]/[N/m^2]
Q	Torque/Velocity	[Nm]/[m/s]
q	Heat flux vector	[W/m^2]
R	Radius	[m]
r	Radial position	[m]
S	Surface	[m^2]
T	Thrust/stress tensor	[N]/[N/m^2]
t	Time/thickness	[s]/[m]
u	Axial velocity	[m/s]
v	Velocity	[m/s]
V	Velocity/volume	[m/s]/[m^3]
w	Up-wash/down-wash	[m/s]
y_+	Normalised wall distance	[-]
α	Angle of attack/Weibull scale parameter	[deg]/[-]
β	Inflow angle	[deg]
$\beta_{0.75R}$	Propeller twist at 75% radius	[deg]
η_P	Propeller efficiency	[-]
Γ	Circulation	[m^2/s]
λ	Wing taper ratio	[-]
Ω	Rotational speed/Twist	[rad/s]/[deg]
ω	Vorticity/washout	[s^{-1}]/[deg]
ϕ	Pitch angle	[deg]

Parameter	Description	Units
Φ_{vortex}	Tip vortex swirl angle	[-]
Ψ	Azimuth	[deg]
ρ	Density	[kg/m^3]
θ_{prop}	Slipstream swirl angle	[deg]
ξ_0	Weibull location parameter	[-]

Subscript	Description
∞	Free stream
θ	Tangential
a	Axial
ac	Aircraft
$ac-w$	Aircraft less wing
A/C	Aircraft
com	Combined
des	Design
eff	Effective
i	Induced
in	Inflow
inf	Free stream
$intern$	Internal
iso	Isolated
$L=0$	Zero-lift
n	Normal
P	Propeller
qc	Quarter chord
r	Radial
s	Static
t	Tangential/total
w	Wing

Abbreviation	Description
BC	Boundary condition
BEM	Blade element momentum
BF	Body-force
CFD	Computational fluid dynamics
DAAA	Department for Aerodynamics, Aeroelasticity & Aeroacoustics
DP	Distributed propulsion
DEP	Distributed electric propulsion
EIS	Entry into service
GA	General aviation
HTS	High temperature superconducting
LE	Leading edge
LEAPTech	Leading edge asynchronous propeller technology
NS	Navier-Stokes
OEI	One engine inoperative
ONERA	Office National d'Etudes et de Recherches Aérospatiales
RANS	Reynolds averaged Navier-Stokes
STOL	Short take-off and landing
TE	Trailing edge
TeDP	Turbo-electric distributed propulsion
URANS	Unsteady Reynolds averaged Navier-Sokes
VLM	Vortex latice method
VTOL	Vertical take-off and landing

1

Introduction

"The search for synergistic integration of the propulsion system at aircraft level through tightly interlaced coupling with the airframe as well as with the other systems on-board the aircraft are expected to lead to dramatic shifts in contemporary aircraft design paradigms."

Clement Pornet (2015) [2]

This report summarises the work that has been conducted in the framework of a master thesis at TU Delft and ONERA. The 9 months lasting project started off with a literature study the conclusion of which are summarised in this chapter. This includes a description of the three topics distributed propulsion, aerodynamic propeller-wing interaction, as well as, simulation strategies. Subsequently, the research objective of the project and its scope are derived. Finally, the outline for the remainder of the report is given.

1.1. Background

This section gives a general introduction to the topic of distributed propulsion. Its historical background and current views on the subject are given first. Afterwards complementary technologies are detailed which are regarded as key enablers for the success of distributed propulsion concepts. Finally, general principles, studied configurations and their anticipated performance benefits are explained.

1.1.1. Distributed Propulsion

The term 'distributed propulsion' is not uniquely defined and has been used in countless different cases. These are mainly aircraft concepts that are characterised by multiple propulsion units (e.g. more that two engines per semi-span), different types of propulsion units and/or different placements of the later. The general goal of these concepts is to improve the aero-propulsive performance of the vehicle by achieving beneficial interaction of the propulsion units and the rest of the airframe. The idea of distributing propulsion is far from new but was so far not implemented in produced products such that its full benefits were exploited. This can be attributed to multiple reasons among which are the complexity of the involved aerodynamics, the fact that the dominating thermal engines loose efficiency when being distributed and reduced in size, and a less integrated classical aircraft design approach. As shall be seen in the following, these obstacles have vanished to a large extend in recent years as computational methods and complementary technologies have improved greatly.

Degree of Electrification Before the idea of electric flight seemed feasible, thermal engines with means to distribute the propulsive jet have been developed. This has been done by simply installing many thermal engines on different locations on the airframe [3]. A recent study by Wick et al. found efficiency improvements in transonic cruise of up to 8% for over-the-wing installation [4]. This concept group also includes a single-core multi-fan approach where mechanical links distribute the core power of fewer thermal engines to multiple fans that can be distributed. Another approach is to have a distributed exhaust with a single-core single-fan engine with ducted nozzles that distribute the exhaust jet over the airframe. The later two concepts, however, suffer from heavy and complex mechanics as well as from efficiency penalties because of mechanical/aerodynamic losses [5–7].

Next to the purely thermal or electric concepts, hybrid-electric aircraft may be a feasible alternative to gain performance improvements from the combined benefits of thermal and electric propulsion. Such concepts have been proposed for example by Airbus and NASA and are also labelled turbo-electric distributed propulsion (TeDP) concepts [8]. They allow the use of a large turbofan engine consuming energy dense kerosene or alternative fuels. The battery is, hence, not required to store the energy for the whole trip and can significantly be reduced in size. The turbofan engine can constantly run at its design point achieving maximum efficiency since its operation is decoupled from the aircraft operations. Distributed electric engines can then be powered with the provided electric power. This concept is especially interesting for higher range requirements when the energy density of batteries become a limiting factor for the feasibility of electric flight. A downside of this idea is the added amount of systems which results in increased propulsion system weight [9] and design effort. Jones et al. [10] present a study on different system architectures. Studies employing TeDP are countless (e.g. [11–18]).

Next to the serial system arrangements that have been mentioned until here, also parallel systems exist where the linkage between the systems is realised with mechanical nodes. The installation of electric motors inside a thermal engine to support/drive e.g. the low pressure shaft could lead to efficiency increases[2, 19]. Another approach is to have classical thermal engines assisted by further propulsors that are electrically driven. This decouples the engine design from the electric components, reducing significantly the design complexity and is identified as being well suited for DP applications [2, 11].

Universally electric aircraft, i.e. electric propulsion with purely electric power supply, are the last group of concepts. The high overall propulsion efficiency of up to 90% that can be reached with this technology is its strongest point [20]. However, the limited gravimetric as well as volumetric energy density of the energy storage media imposes a big weight problem on this idea. This may limit its application to short range missions where the weight penalty is less pronounced [21].

Boundary Layer Ingestion One category of distributed propulsion is related to boundary layer ingestion. There exist two main concepts in this area. The first is the ingestion of the fuselage boundary layer by distributing the propulsion units at the top rear fuselage. This is mostly integrated in blended wing body concepts as illustrated in Figure and has been investigated in many studies [9, 22–28]. The second category adds one big propulsor at the end of a regular tube fuselage, ingesting its entire boundary layer. These concepts are dubbed propulsive fuselage by Bauhaus Luftfahrt [29] or wake-propeller by NASA [30]. Since this approach has fundamentally different flow physics from propeller-wing interactions to be studied in this project, no further details on this approach is given and the reader is referred to the above-given literature.

Propulsion Integration into the Wing Other distributed propulsion concepts focus on integrating the propulsion unit directly into the wing (also called embedded distributed propulsion). Examples of these are Kuchemann's jet wing aircraft that features jet engines between the upper and lower surfaces of the wing [31] (also see [32–34]) or Hancock's cross flow fan concept [35] (and similar concepts by Bauhaus Luftfahrt [36] or Fanwing Ltd [37, 38]) which incorporates several cross flow fans in front of the flap hinge line. Since these are powered by wing-tip mounted gas turbines, this is also a hybrid form of distributed propulsion. The jet flap variant (as installed on the Hunting H.126) pushes a jet sheet out of a TE slot in the wing to increase circulation and high-lift capability [8]. Also some ducted fan concepts that are becoming more visible in publications may be considered to fall under this category. An example is the Aurora LightningStrike. Variable nozzle areas allow efficient operation at different flight speeds while small control surfaces at the outlets give an additional control mechanism.

Propeller Distribution Finally, the group of distributed propeller concepts exists. These propellers can be distributed somewhere along a lifting surface. Proposed ideas so far included wing-tip propellers, counter-acting the wing-tip vortices to reduce the induced drag. Other concepts have high-lift propellers that are distributed in front of the leading edge to blow over a large fraction of or over the entire wing surface with the goal to increase the maximum lift coefficient. Also other configurations like over-the-wing propellers or pusher propellers could be thought of. Furthermore, many concepts feature a combination of some of these types. It is this group of distributed propulsion concepts that this research project focusses on. For the rest of the report, the term 'distributed propulsion' will be used to describe this limited group of concepts. A first reason for this focus is the lower degree of uncertainty that the employment of several propellers imposes on the design. Furthermore, the many different configurations that can already be thought of with this approach are already more than can be analysed in a single project. Also the promising performance improvements that are expected to result from this technology make it an attractive candidate. Finally, the relatively straight forward way of analysing the distributed propellers are a good starting point to assess DP instead of directly jumping into highly integrated architectures. Examples under investigation are NASA's SCEPTOR project and the JOBY S2 concept (see Figures 1.1 and 1.2).

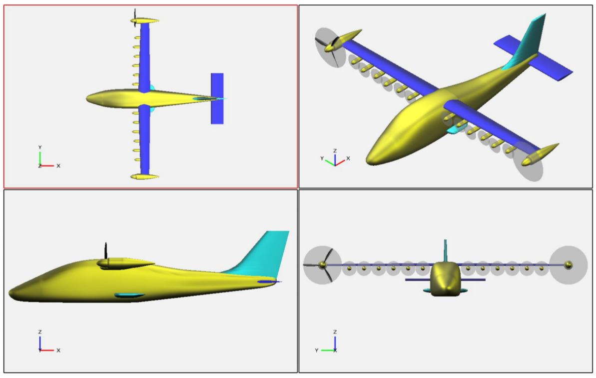

Figure 1.1: NASA SCEPTOR concept showing tip-mounted cruise propellers and leading-edge high-lift propellers [39]

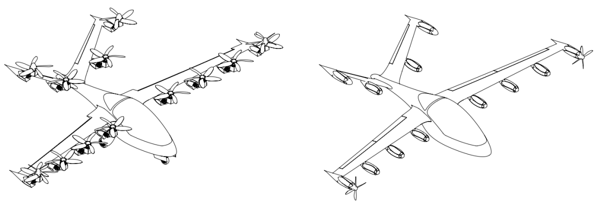

Figure 1.2: JOBY S2 concept showing foldable high-lift propellers and propeller tilt-mechanism for VTOL [40]

Figure 1.3b shows three different possibilities of integration, where the first option is structurally complicated to realise while probably performing best in achieving high lift coefficients. The second option is structurally less problematic but wake ingestion from wing as well as from the flap could raise the noise levels considerably. Since the concept was to be studied by Moore et al. on aircraft level with low-fidelity methods to explore the design space, the third option was chosen and the other versions were ignored at first [41]. The choice for the tractor propeller configuration is justified by Moore, not because it is regarded as most promising, but because it incorporates the least uncertainties. The result of these LEAPTech studies featuring high-lift tractor propellers, wing-tip pusher propellers, a wake-propeller and a variable-incidence wing can be seen in Figure 1.3. Since the project of this report limits itself to the aerodynamic analysis, however, also above-wing/pusher concepts can be studied to see the isolated difference in aero-propulsive efficiency and performance. A lot more about the involved principles is presented in Chapter 2.

(a) Selected configuration

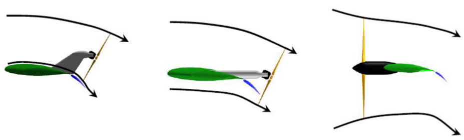

(b) Propeller wing integration concepts including over-the-wing, trailing-edge, and leading-edge installation of the propeller

Figure 1.3: NASA LEAPTech concept showing propeller integration concepts as well as selected configuration with wing-tip mounted cruise propellers and leading-edge high-lift propellers [41]

Applications Not only the way of distributed propulsion integration but also the types of aircraft to which it is applied vary a lot. Generally, the concept can be applied to any aircraft mission but is mostly considered for subsonic flight [7]. As Moore pointed out, the required technologies imply uncertainties and will most likely first be implemented in small scale applications to be scaled up later. Because of the large performance increase opportunity, the GA market is said to be a good starting point. This idea is shared in the scientific community and lead to many concepts being developed (e.g. Joby S2, Sceptor, LEAPTech, A^3 Vahana, Lilium [39–43]). Also still on a small scale, UAVs may be an early application (and it could be argued that multi-copters already have distributed propulsion characteristics) [44, 45]. Regional concepts [12, 13, 46] could be the following big step and are under investigation. Long-Range concepts are mostly (but not solely) BWBs but also tube-wing configurations (EU Dispursal project [12, 47], A350-1000 variant [48], and others).

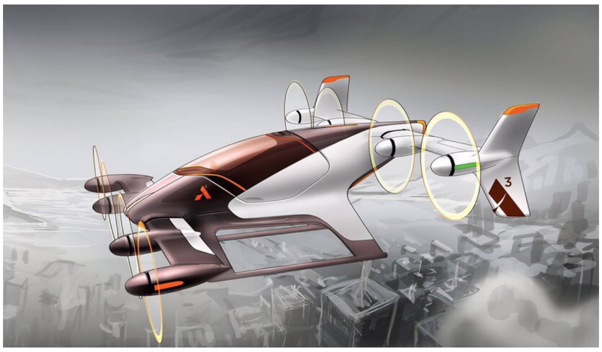

(a) A^3 Vahana concept[1]

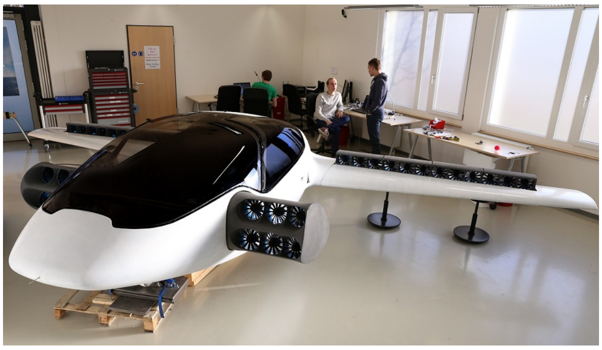

(b) Lilium Aviation prototype[2]

(c) NASA GL10 prototype[3]

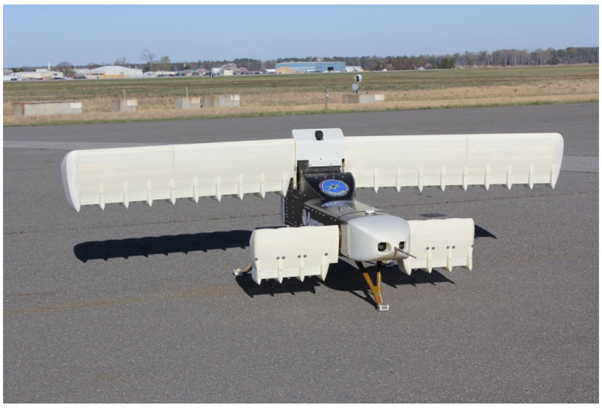

(d) Aurora LightningStrike prototype[4]

Figure 1.4: Distributed propulsion concepts featuring multiple fans/propellers and variable incidence wings

The expected time frame of entry into service differs significantly between the previously mentioned groups. GA may already be introduced in the coming years with concepts being currently tested on sub/full scale models [49] (see Figures 1.4a to 1.4d). These models already proved that the VTOL capability (including transition to forward flight) is possible. Moore states that although the electric aircraft will enter the market in the GA and drone market first because of its smaller scale and the immense performance benefits, it is realistic to expect regional/commuter aircraft within 10 years [41]. Long range concepts are a whole different category with regard to uncertainties, risks and design complexity and are expected to be viable maybe within 20 years

[4]Lyasoff, Rodin: Welcome to Vahana. A^3, 2017. URL: https://vahana.aero/welcome-to-vahana-edfa689f2b75, online, accessed April 5, 2017.
[4]Lilium GmbH: Lilium Aviation. 2017. URL: https://lilium.com/, online, accessed April 5, 2017.
[4]NASA: Ten-Engine Electric Plane Completes Successful Flight Test. 2015. URL: https://www.nasa.gov/langley/ten-engine-electric-plane-completes-successful-flight-test, online, accessed April 8, 2017.
[4]Aurora Flight Sciences: XV-24A LightningStrike: Vertical Take-off/Landing Experimental Plane. 2015. URL: http://www.aurora.aero/lightningstrike/, accessed April 8, 2017.

according to Isikveren et al. [12, 47] and other studies focussing on EIS 2035+ [18, 25, 48, 50].

Anticipated Performance Benefits As mentioned earlier, the anticipated performance benefits of distributed propulsion concepts are manifold. This comes from the added design freedom of the propulsion integration of electric machines. These freedoms can be used to place the propulsion units such that the design is optimised for key metrics like drag and noise. The following list tries to summarise the possible benefits that the scientific community has identified so far.

- **Zero in-flight emissions** are an inherent property of any distributed propulsion concept when being purely electrically powered. This is an important factor of any future means of transportation [51, 52] and is therefore a strong argument for the implementation of DEP.
- **STOL** ability can easily be achieved with lift augmentation. Thrust vectoring can even lead to a realisation of **VTOL** concepts like the JOBY S2 (see Figure 1.2) [8]. Also, the VTOL operation can be achieved more efficiently with DEP since the efficiency of electric motors is much less sensitive to the power setting than that of thermal engines [53].
- The coupling of propellers and wing can generate a benefit in **aero-propulsive efficiency**. While both induced drag reductions and propeller efficiency increases are attainable, these effects are hard to separate [41] requiring either consistent drag and thrust bookkeeping or employing other metrics like exergy analyses. Reductions in fuel consumption can also be achieved by ingesting the thick boundary layer flow and filling in the wake generated by the airframe with the distributed engine thrust stream but this will not be further discussed in this project [22].
- **Power sizing** benefits can be achieved with installing many propellers. The insensitivity to hot & high conditions of electrically powered propulsors lowers the required engine power at sea level conditions [41]. Additionally, failure modes like the OEI condition are less severe in power system sizing because of the high level of redundancy and reliability [54, 55]. Less disc-loading because of increased disc area has also been shown for the LEAPTech project, leading to higher low-speed thrust and better climb rates [41].
- The idea behind high-lift propellers is to increase the **achievable maximum lift coefficient** compared to the clean wing. This is a result of additional dynamic pressure from the propeller slipstream as well as thrust vectoring and circulation control. This is an alternative to the classical high-lift devices that are installed on basically all aircraft flying today. Making these complex, hard to design and maintenance intensive systems redundant would have several benefits. First of all the design of these systems is very costly and increases the purchase price of the aircraft. Secondly, the maintenance of these systems increases the operating costs of the aircraft. Thirdly, the wing can structurally and aerodynamically be much 'cleaner' without these systems, removing gaps, support track fairings and subsystems [41, 56].
- High-lift propellers are not only reducing the high-lift system requirements but also allow to design the wing more optimally for the cruise condition. Current GA aircraft wings are mostly sized for take-off and landing requirements making them oversized for cruise conditions. This leads to additional drag during cruise and worse ride quality because of the high gust sensitivity of the large wings. If the maximum lift coefficient can be increased such that the field length requirements can be met with smaller wings, the wings may designed more optimally for cruise conditions, yielding better **ride quality** as well as a better **lift-to-drag ratio** yielding an increase in range [41, 57, 58].
- **Control** of the aircraft may be achieved by differential thrust/thrust vectoring. This could lead to a redundancy of the classical vertical and horizontal tail configuration leading to reduced friction drag and mass. It also provides additional reliability for the control as one engine failure may easily be counteracted by the other propellers. Robust propulsive control additionally improves in low speed conditions instead of degradation This cancels the problem of high yaw moments in OEI cases like with two or four engines, making outboard installation possible for better higher gains in induced drag reduction. A different means to improve control is the installation of propellers in front of control surfaces [8, 41, 57, 59, 60].

- **Noise reduction** can be achieved with various approaches. High-lift propellers may be used to avoid the installation of sound-generating high-lift devices. Furthermore, steep or vertical take-off and landing capabilities could reduce the duration of noise exposition. Additionally, noise shielding by distributing the propulsion over the wing has been shown to significantly reduce the perceived noise levels [61–63]. There is, however, also a challenge to avoid new forms of noise generation. The interaction of propeller slipstreams because of close staggering, unsteady propeller loads because of closely coupled wings and other effects can be a source of noise as discussed by Moore & Fredericks [41] and have to be taken into account when designing new concepts. An example is the LEAPTech project which features asynchronous rpm propellers to avoid acoustic beating phenomena of the high-lift propellers.

- As mentioned before, **maintenance** can be reduced by making high-lift systems redundant. But also the propulsion units itself are less maintenance intensive than thermal engines [64]. Additionally, removing transient operations from gas turbine engines by decoupling their operation from the thrust setting reduces transient temperatures and therefore maintenance [15].

- As an overall result, the **operating costs** of distributed propulsion aircraft can be reduced compared to current alternatives. Although the purchase price may currently be higher, the previously mentioned reduction in energy consumption and maintenance work can lead to reductions in overall costs. This has been demonstrated for GA aircraft by Stoll et al. where the operating costs of a GA employing DP saves a lot in operating costs, outweighing the purchase cost increase and leading to a total costs saving for the considered missions [60].

1.1.2. COMPLEMENTARY TECHNOLOGIES

Several technologies are required to exploit the full benefits of DP. Simulation capabilities, energy storage, electric components & systems, as well as vehicle autonomy are all heavily funded research areas and have been identified to be key to the success of DP and DEP in particular. These are discussed in the following sections.

Simulation & Analysis capabilities New simulation capabilities are required for DP concept analyses. The high degree of interaction between propulsion and airframe cannot accurately be modelled with current tools. Moore states that especially detailed CFD simulations and aero-elastic analysis will be required to demonstrate that anticipated benefits can actually be realised [65]. For further details on this topic, the reader is referred to Section 2.2, dedicated to the simulation techniques for wings, propellers and their interactions.

Electric Components & Systems Electric propulsion is regarded as a key enabler for distributed propulsion. This has several reasons. First of all electric machines are relatively scale independent. This is very different from thermal engines that suffer from efficiency losses, decreased reliability and power-to-weight penalties when scaled down (decreased Reynolds number and more leakages lead to higher heat and pressure losses) [66]. This characteristic adds design freedom by allowing the distribution of the propulsion system over the airframe to achieve performance benefits. These benefits are manifold and touch not only upon energy efficiency but also include aircraft noise, reliability, maintenance, aircraft control and other areas [7].

Electric motors and generators are under heavy development. First of all, the up-scaling of current rather small electric machines is a hurdle but cryogenic high temperature superconducting (HTS) motors with power levels of several MW have been built [64]. Furthermore, the specific power is tried to be increased and studies suggest, that values similar to turbofan engines can be achieved. This requires the realisation of HTS motors which are investigated by many research groups but represents one of the biggest challenges [7, 67].

General electric machines have been found to be impractical for flight applications because of their inefficiency and weight penalties [68] although it has been shown that slight benefits can be generated with conventional technologies [69]. HTS motors have improved gravimetric specific power (estimated 3.3 [7] to 5.0 [50] times that of a modern turbofan) and efficiency and are therefore regarded as key technology for electric propulsion [64]. Also HTS lines are under consideration featuring transmission losses estimated around only 0.03% [9]. For this reason the thermal management becomes a core problem when employing electric propulsion [70]. However, having cryogenic energy sources like liquid hydrogen, beneficial interactions could be generated [13, 15]. For these reasons, Cryo-cooler development is one of the main challenges in realising HTS machines [9].

Energy Storage Energy storage systems have to satisfy performance criteria with regard to their gravimetric specific energy and power levels. The combined energy and power requirements have been noticed to give higher difficulties in design than the individual ones. Additionally, efficiency, operating temperature, safety, reliability, and discharge behaviour are important design considerations. From a sustainability point of view, the recyclability of energy storage media is a further criterion which especially for limited life-span batteries can be a problem [2].

The most promising battery candidate for the near future is the lithium battery with current energy densities of about 200 Wh/kg and predicted capability of 400 Wh/kg [2] which is also the order of magnitude used as assumption for design studies of near future electric aircraft concepts like LEAPTech (leading edge asynchronous propeller technology) [42, 60]. Open lithium-air batteries, currently only in laboratory status could reach 1000-2000 Wh/kg by 2030 [2].

But batteries are not the only possible energy source and a lot of studies for alternative or combined energy sources have been conducted. Hydrogen as future energy source is especially interesting in combination with fuel cells [7] because of the high energy density compared to batteries (2.8 times the gravimetric energy density compared to kerosene [71] while requiring 4 times the storage volume) [72]. As mentioned previously, the combination with HTS components could give the energy source a second function as coolant [15]. This hybrid strategy may, however suffer from limited power density which could outweigh the fact that efficiency levels could reach that of advanced turbofan engines [72]. It therefore remains to be seen how energy storage technologies advance over the coming years to identify which options are best suited for future aviation.

Vehicle Autonomy Vehicle autonomy has been identified as key enabler for on-demand aviation as well [65]. This is firstly based on the observation that it is expensive and time-consuming to obtain an all-weather private pilot license. The high costs also apply to hired pilots. A second reason is the high rate of accidents with human error as (at least partial) cause. When introducing vehicle autonomy, the human responsibility is transferred from the pilot to the vehicle designer, who is now required to develop highly reliable systems by anticipating countless possible circumstances. It is regarded as most likely, that semi-autonomous vehicles will first be developed that require less pilot training, less development costs and are able to manage the most probable incidents. Later, fully autonomous flying will be realised according to researchers like Moore and industry leaders like Airbus CEO Tom Enders[5].

1.1.3. CURRENT STATE

An introductory and much cited paper on electric aviation has been published by Moore [41]. The paper points out how the way of designing such aircraft is fundamentally different from conventional ones. He argues that electric propulsion allows new configurations due to the different characteristics of electric machines that can generate added value. This means that such new configurations (e.g. featuring distributed propulsion) have to be analysed to see what the benefit of electric flight can be. Simply replacing the thermal engines by electric ones will not reveal the full added value. Moore also adds, that new physics-based models will be required to analyse these new configurations. By that he gives a direct motivation for the proposed research project to push forward the simulation capabilities to analyse such highly integrated concepts. His argument, that only a multidisciplinary analysis can be used to compare electric aircraft to conventional ones on aircraft level because of their high dependence on the cross-disciplinary benefits also sets the scope for this project (i.e. not to derive or analyse full concepts but to progress on the simulation techniques and to study aerodynamic phenomena). In a previous article he further lines out why a strong demand for on-demand mobility featuring DEP exists and why this is a good entry market for this technology [65]. Gohardani

[5]Airbus: Future of urban mobility - My kind of flyover. 2016. URL: http://www.airbusgroup.com/int/en/news-media/corporate-magazine/Forum-88/My-Kind-Of-Flyover.html, online, accessed April 5, 2017.

shares this opinion and adds that, although the synergistic effects have to be studied in detail, also important milestones for the independent systems have to be reached, requiring step changes in certain areas [56].

1.2. RESEARCH OBJECTIVE

For aircraft with distributed propulsion aero-propulsive integration becomes central to aircraft performance. Knowledge in this area, together with efficient analysis tools, is a necessary skill in the process of aircraft design. Current design-order tools used in aircraft design are barely adequate to handle such new aircraft architectures. And the full potential benefits of distributed propulsion can only be attained through a good understanding of the aerodynamic interactions between propulsion and airframe. Only limited knowledge on the driving parameters and the possible benefits is available.

The literature review revealed a necessity for higher fidelity tools to simulate distributed propulsion configurations in order to better understand the aerodynamic coupling of the components. There are two main objectives that have been derived from this observation:

- **To progress in numerical methods for aerodynamic wing-propeller interaction simulation.** The objective is twofold and shall be achieved by:
  - Demonstrating the benefits of using a body-force approach in the RANS CFD simulations as a means to model the propellers and thus obtain high-fidelity aero-propulsive analyses at a lower cost than unsteady analyses in which the propellers geometry would be meshed and solved.
  - Assessing the accuracy of the lifting-line & free-wake approach to capture aero-propulsive interaction phenomena by comparing CFD results against lifting-line & free-wake results.
- **To gain knowledge on the physics of aero-propulsive phenomena and performance** by:
  - Selecting relevant configurations and parameters from literature and first simulation results.
  - Applying the different simulation strategies to simulate the configurations of interest.
  - Gaining understanding of the aerodynamic interactions through analysis of simulation results.
  - Comparing observed phenomena and trends with those found in literature.
  - Deducing trades and sensitivities for guidance in aircraft design.

1.3. SCOPE OF THESIS

The scope of this research project is to progress in both, the numerical methods to analyse the interactions of distributed propulsion and lifting surfaces as well as the analysis of sample geometries to identify driving parameters and phenomena to ultimately derive trends and design rules for future concepts.

Analysed geometries are simplified to derive general trends that are valuable for different designs instead of focussing on very specific and detailed geometries. The project excludes the generation of concepts from the gained knowledge. Also the analysis is limited to the aerodynamic interactions of the components and does not take into account other systems (e.g. the design of the electrical components, structural/acoustic considerations or others). Furthermore, time averaged simulations prohibit the inclusion of unsteady behaviour to a large extend.

Finally, the term 'distributed propulsion' has been noticed not to be uniquely defined and generally contains concepts with more than two propellers per wing, boundary layer ingesting propulsors and further ideas that feature either many propulsors or at least propulsors that are differently placed on the airframe. This thesis will limit itself to multiple propellers distributed somewhere along the wing without presence of fuselages or other geometries. This choice is supported by the relative simplicity to simulate such configurations as well as their high predicted performance gains.

1.4. THESIS OUTLINE

This report summarises all the work that has been performed during the 9-months lasting project. It contains six further chapters and covers background knowledge, tool description & validation, a results section as well as concluding remarks.

Chapter 2 begins with general background knowledge on aerodynamic propeller-wing interaction, covering classical propeller-wing configurations as well as recent advances on distributed propeller effects. The second part of the chapter is devoted to existing simulation techniques used to assess these configurations.

Subsequently, Chapter 3 elaborates on the chosen geometries and flight conditions used during the project. The methodology is presented in Chapter 4. This includes a description of the used simulation tools, the numerical settings and the convergence behaviour. Furthermore, the newly developed coupling procedure between the lifting-line and RANS tools is explained.

To show that the coupled simulation strategy is able to resolve the aerodynamic interaction effects accurately, the method's results are compared to experimental and meshed propeller URANS results in Chapter 5, devoted to the tool's validation.

In the next chapter (Chapter 6) the tool is applied to interesting configurations to assess different design choices and gain insight into the governing flow physics. Selected examples include wing-tip mounted pusher/tractor propellers as well as lift-augmenting propellers installed at the leading egde or over the wing.

Finally, important conclusions from the presented content are highlighted and recommendations for future research activities on the topic are presented in Chapter 7.

2

Background Theory

"[...] these capabilities also require aircraft that are fundamentally different than small aircraft today; and electric propulsion has the capacity to interact with all other disciplines in positive synergistic ways to overcome the current deficits and create remarkable new flying machines."

Mark D. Moore et al. (2013) [65]

2.1. Aerodynamic Propeller-Wing Interaction

This chapter elaborates on the knowledge on aerodynamic propeller-wing interaction that has been acquired by the scientific community in the past. The theory of propeller and wing aerodynamics dates back to the very beginnings of aviation and it also only took until 1921 that the interaction of both components was acknowledged by Prandtl. Since then researchers and aircraft designers try to understand the underlying flow physics and derive design methods for propeller aircraft. First, the chapter will give a theoretical background on the involved aerodynamics. Subsequently, the state of the art for conventional propeller aircraft concepts is described. Finally, the particularities and first insights into the flow physics of distributed propulsion aerodynamic interference are presented.

2.1.1. Wing Aerodynamics

The reader is assumed to have basic knowledge on general wing aerodynamics. Therefore, only some summarising words are given. Generally speaking, a wing is a means to produce lift. This is done by shaping the cross-section of the wing such that the integrated pressure distribution over the surface results in a lifting force. In order to reduce the thrust it takes to push the wing through the air, the drag is tried to be minimised. The drag has several sources. The normal force, resulting from the integrated pressure over the surface does not only have a lifting but also a tangential component, called pressure drag. Additionally, skin friction drag results from the boundary layer because of viscosity of the fluid. However, this physical drag breakdown is not always what is directly available from simulations. From a computational perspective it therefore sometimes makes sense to split the drag components into different categories. This is often done by summarising all skin friction and profile pressure drag components into the term profile drag. The induced drag resulting from the finite nature of the wing is mostly observable as the wing-tip vortex extracting kinetic energy from the flow and is a direct result of popular vortex theory based codes. For this reason, induced drag is also often called vortex drag. A third way to classify drag components is from an energy loss perspective. The profile drag is then composed of two mechanisms, the first being wake drag (stemming from the formation of wakes behind flow separation due to different reasons) and the second being wave drag (as a result of shock wave formation and associated energy losses). For further information, the reader is referred to standard textbooks like Anderson [73] or Burton & Cummings [74].

2.1.2. PROPELLER AERODYNAMICS

Propellers are a means to provide thrust by adding momentum to a certain mass flow. This is done by multiple blades which are essentially rotating wings. These blades exert a force field on the fluid. The first powered flight by the Wright brothers was powered with propellers. Albert Betz and Ludwig Prandtl continued to study their aerodynamics [75] and were the first to acknowledge the strong interaction between propeller and wing [76]. After the time of the jet engines in the 50s to 70s where the interest in this technology declined, the propulsion option continues to propel many modern aircraft until today and started to get renewed attention. This is partially connected to their high propulsive efficiency paired with high energy prices and partially to the anticipated performance benefits from proper integration as stated in the last chapter. The propeller for aircraft use was studied by many engineers and just as many simulation techniques have been brought forward as shall be seen in the next sections. However, the different applications, circumstances and requirements still lead to a lot of recent research in the area. A summarising article on the aerodynamics of propellers has been written by Wald [77].

Typical for a flow behind a propeller is the increased dynamic pressure and the added swirl component, resulting from the rotating blades that introduce rotational kinetic energy to the fluid. A good description of the slipstream of propellers is given by Veldhuis [78] and is shown in Figure 2.1a. It can be observed how the blade vortex sheet rolls up and follows a helical trajectory behind the blades. It is also shown that the stream tube contracts downstream of the propeller disc.

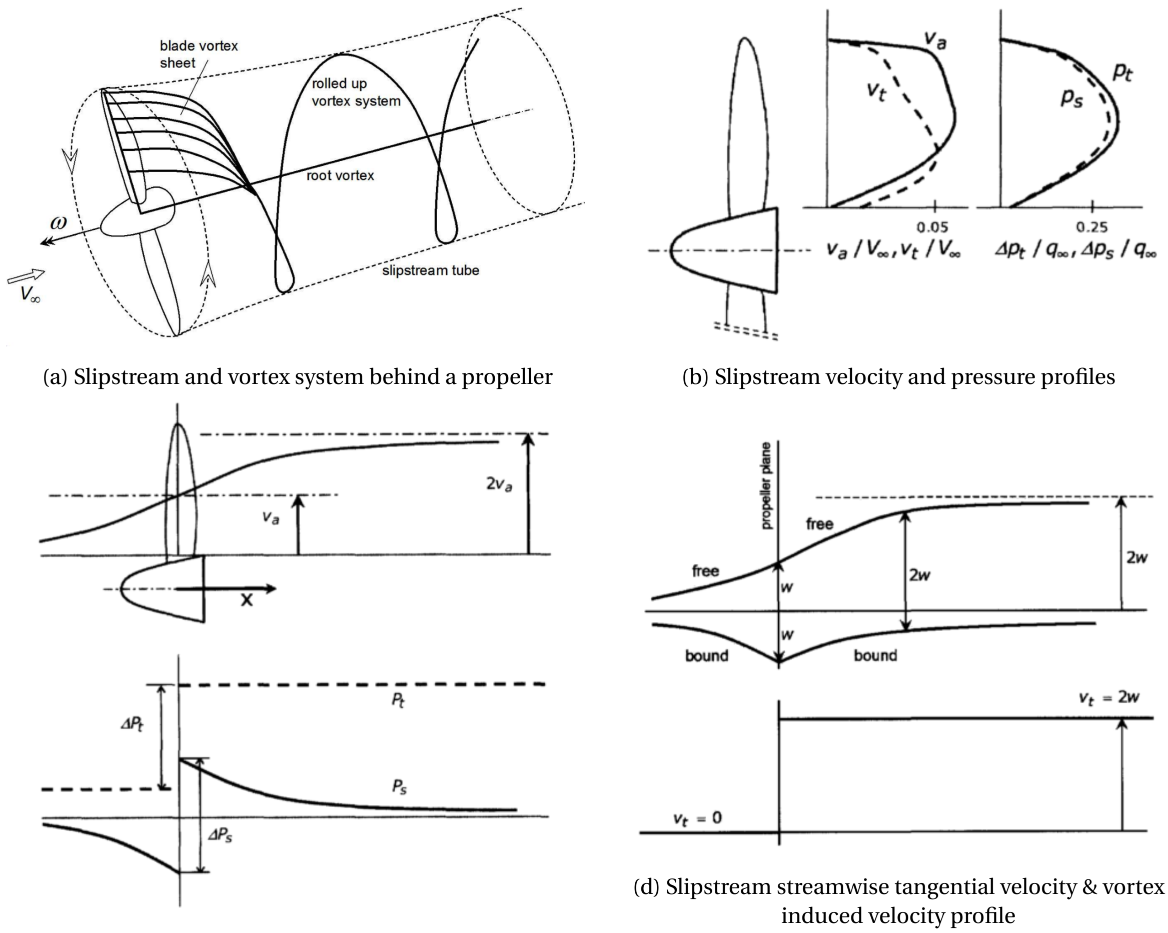

(a) Slipstream and vortex system behind a propeller

(b) Slipstream velocity and pressure profiles

(c) Slipstream streamwise axial velocity & pressure profile

(d) Slipstream streamwise tangential velocity & vortex induced velocity profile

Figure 2.1: Propeller slipstream characteristics showing vortex system as well as velocity and pressure profiles [78]

Some basic non-dimensional quantities for the description of propeller performance are given in Equations 2.1 to 2.4. J is the advance ratio and provides a ratio for the free stream velocity to the rotational velocity of the propeller (i.e. how far does the propeller travel in axial direction per revolution). The thrust coefficient C_T and power coefficient C_P are non-dimensionalised values for the thrust and power of the propeller. μ_P is the propeller efficiency and quantifies how much of the shaft power is translated into propulsive power.

$$J = \frac{v_\infty}{n \cdot D} \tag{2.1}$$

$$C_T = \frac{T}{\rho \cdot n^2 \cdot D^4} \tag{2.2}$$

$$C_P = \frac{P}{\rho \cdot n^3 \cdot D^5} \tag{2.3}$$

$$\eta_P = \frac{T \cdot v_\infty}{P} \tag{2.4}$$

The slipstream of a propeller can be characterised by the axial and swirl velocity profiles, static and total pressure distributions, vorticity, helicity and contraction. The axial velocity profile has its maximum value at the radial location of approximately 3/4R while the induced axial velocity goes to zero and the tip and the root of the blades (see Figure 2.1b). Moving downstream from the propeller, the axial velocity of the slipstream constantly increases, approaching two times the induced velocity at the propeller plane, making the longitudinal positioning of the propeller an important design variable (see Figure 2.1c). The tangential (or swirl) velocity profile shape, in contrast to the axial one, is not constant with varying propeller loading. On the other hand, the tangential velocity does not change in axial direction because of the influence of bound and free vortex as depicted in Figure 2.1d. With the changing axial velocity this leads to a gradient in swirl angle in axial direction. The static and total pressure distributions at the propeller disk have a maximum at 3/4R since the highest loading is present at this point. The static pressure is somewhat lower as the total pressure has an additional contribution stemming from the induced tangential velocity component. The axial profiles differ more, the total pressure is constant with a sudden jump at the propeller disk while the static pressure varies when approaching the propeller plane and jumps at the same. The vorticity of the flowfield behind a propeller characterises the rotational properties of the slipstream. Vorticity is found in the vortex sheet and is highest at the blade tips where the tip vortices are located. Helicity, on the other hand, is a measure of alignment between the vorticity and velocity fields. This alignment is usually high at the hub, whereas the opposite holds for the tip region. In between, nearly only weak alignment can be observed. As the velocity increases behind the propeller disk, the slipstream contracts to keep the mass-flow constant. This contraction becomes more pronounced as the propeller loading increases. The effect reduces the wing fraction immersed in the slipstream. An amplifying effect is the presence of a finite nacelle forcing the slipstream to further contract [78].

Betz and Prandtl already identified in 1919 that the condition for maximum efficiency is such that a non-deforming vortex sheet is shed behind the propeller but only had approximate solutions for lightly loaded blades [75]. Later, Goldstein found a potential flow solution for small advance ratio propellers [79]. Theodorsen removed the light loading restriction. The first practical design method was proposed by Larrabee [80] but is again limited to lightly loaded propellers. The most popular paper today by Adkins and Liebeck [81] describes a methodology for designing optimum propellers also for relatively highly loaded propellers without small angle approximation and including viscous and radial flow effects.

2.1.3. CLASSICAL PROPELLER-WING INTERACTION

The fact that the interaction between propellers and wings plays an important role in the aerodynamics was already acknowledged by Prandtl [76] who mentioned the effects of increased axial velocity and swirl on the wing. Large interest in a deeper understanding of these interactions arose in the 70s because of increasingly high oil prices. After a time of clear jet engine dominance, the propeller experienced a come back in the 70s and more research on their proper integration on the airframe started [78]. This section first lists some basic interference effects that have been identified before going into more design-oriented considerations.

Slipstream Induced Velocities over the Wing The previously described slipstream of a propeller, in typical tractor configurations, washes over the wing surface. The axial and tangential induced velocities in the propeller wake therfore interact with the wing surface. The axial velocity increase basically acts as a local increase in dynamic pressure (and hence the lift and drag components) experienced by the lifting surface. The swirl component of the slipstream causes local variations in angle of attack. The wing fraction behind the upgoing blade experiences an upwash while the fraction behind the downgoing blade experiences a downwash. Witkowski shows in his article [1] how the change in effective angle of attack leads to a change in the resultant force such that a local thrust force can be observed. The opposite happens in the the downwash area (see Figures 2.2a and 2.2).

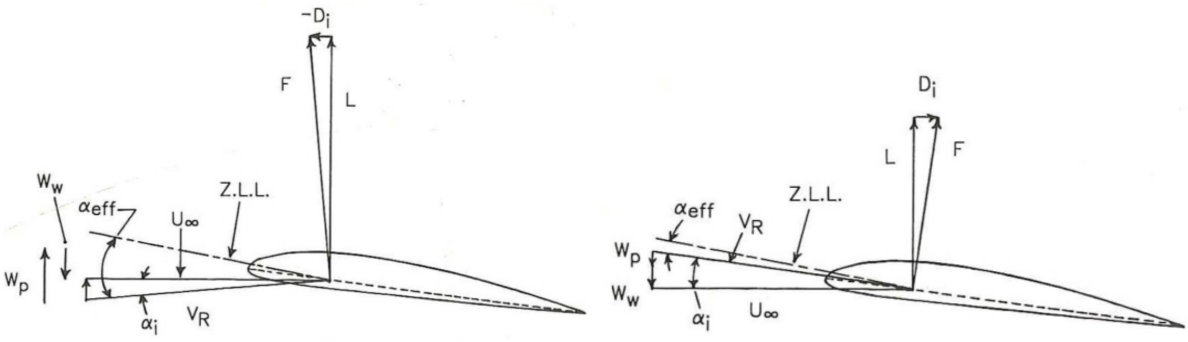

(a) Wing section in propeller upwash experiences increased effective angle of attack resulting in higher lift and lower drag

(b) Wing section in propeller downwash experiences reduced effective angle of attack resulting in lower lift and higher drag

Figure 2.2: Propeller swirl effect on wing section angle of attack and resultant forces [1]

The notional changes in wing lift distributions by the two combined effects is depicted in Figure 2.3a. The difference in the sense of rotation becomes apparent when comparing the two lift distributions. Additionally, it can be noticed that the effects extend to regions outside the slipstream (W-I & W-IV) [78]. It will be seen later in this section that these effects strongly depend on the longitudinal, lateral and vertical positioning of the propeller with respect to the wing. Catalano [82] also tested pusher configurations and showed that the upwash in front of the wing can be reduced by the presence of the propeller.

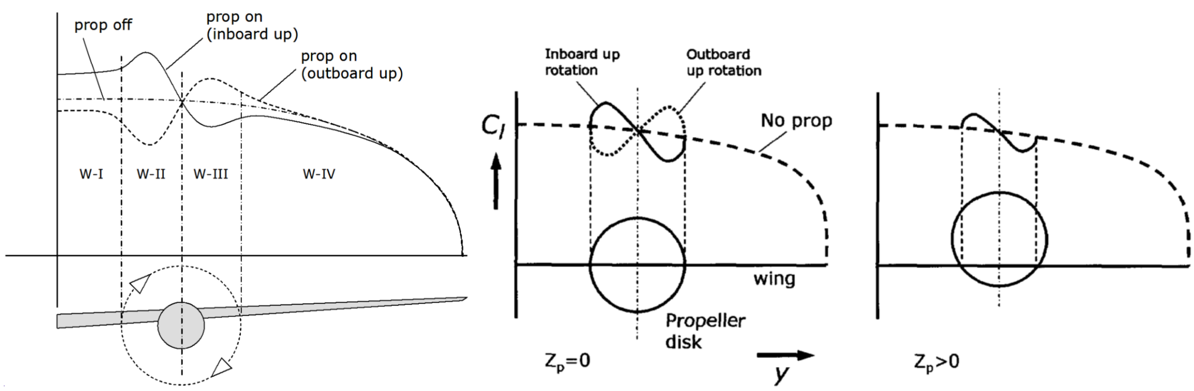

(a) Slipstream effect on wing lift distribution for propeller inboard/outboard up rotation

(b) Effect of vertical propeller position on wing lift distribution

Figure 2.3: Effect of propeller slipstream on wing lift distribution [78]

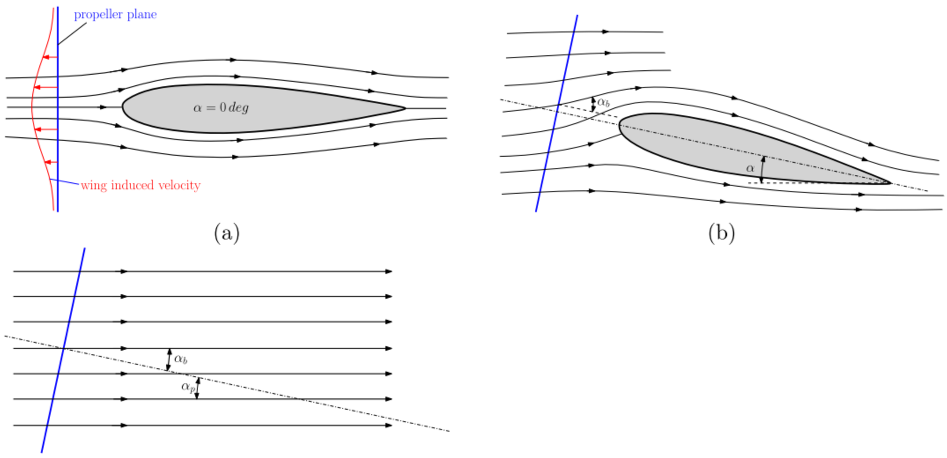

Figure 2.4: Propeller under Wing Influence showing effect of stagnation, thickness, up-wash and angle of incidence [83]

Stator Vane Effect & Swirl Recovery As explained earlier, the slipstream behind a propeller features a swirl component which does not contribute to the thrust generation and therefore is a loss term in propeller efficiency. It has been shown, however, that part of this loss can be recovered by stator vanes [84]. A wing behind a propeller can act as such a stator vane as well. Going back to Witkowski's drawings it can seen how an increase in angle of attack leads to an increase in lift and a forward rotation of the force vector. The opposite happens in case of a decrease in local angle of attack. While the change in vector angle is the same in both cases, the magnitude of the vectors is different. This combination leads to an overall decrease in angle of attack since the local thrust increment in the upwash region is larger than the local drag increment in the downwash region. This swirl recovery starts already at the leading edge of the wing such that the rear part experiences less swirl than the front part. This reduces the swirl recovery of the rear parts of the wing. The potential of reducing the induced drag of tractor propeller configurations by proper integration has been demonstrated with simulations and wind tunnel tests [1, 78, 85–88]. Design rules to achieve this performance improvement are given in this section.

Tip Vortex Attenuation As shall be seen in the following, the induced drag of the wing can be reduced by attenuating the wing tip vortex. This happens when the installed propeller rotates in the opposite direction compared to the sense of rotation of the vortex. Having the two circulations with opposite orientation has been shown to shift the tip vortex downward and outboard, decreasing its downwash effect on the wing. This effect appears to be strongest when the propeller is located at the wing tip when the interacting circulation of wing tip vortex and slipstream lead to a dissipation of the wing tip vortex. It is, however, still present for inboard installations [1, 86, 87, 89–91]. More information on this can be found in Section 2.1.5 dedicated to wing-tip mounted propellers.

Slipstream Contraction As mentioned previously, the slipstream contracts behind the propeller to maintain mass-flow at increased axial velocity. The contraction first of all implies the existence of radial velocities that again have the ability to change local angles of attack at trailing wings. Veldhuis observed this phenomenon in wind tunnel tests and noticed an increase in local lift behind an upward displaced propeller. Secondly, the contraction changes the part of the wing surface that is washed by the slipstream. The contraction is larger for higher loaded propellers but usually amounts to only a few percent [87].

Viscous Effects Catalano [82] showed how propeller slipstreams can promote early transition of the trailing wing boundary layer. He attributes the transition mainly due to boundary layer-blade wake mixing and showed that similar results can be obtained without propeller by tripping the boundary layer at the wing fraction immersed in the wake with propeller installed. Ananda [44] focussed on low reynolds number flows for UAV application and showed that profile drag can be reduced by early transition on washed wing surfaces.

The normally present laminar separation bubble at these reynolds numbers was shown to be avoided. This is also shown for the example of Catalano with a pusher configutation [82]. In this case, the formation of the separation bubble is postponed to higher angles of attack. By alleviating the adverse pressure gradients at the rear of the wing also higher stall angles were achieved.

Vortex Cutting & Bending When the helical prop-tip vortices impinge on the wing they are cut by its presence. Because of the different flow fields on the upper and lower wing surfaces the vortices are convected differently, leading to a skewing of the helix structure. The upper and lower halfs are therefore misaligned at the trailing edge but rejoin behind the wing [92]. This vortex cutting has been studied in more detail by Thom [93]. He noticed that the vortices are bent, before being cut by the wing. The stagnation region at the leading edge decelerates the axial motion of the vortex near the surface leading to a stream-wise bending. This partially aligns the vortex with the flow direction leading to a pronounced effect on the local surface pressure. The vortex is further bent parallel to the surface, followed by secondary vortices, while moving downstream. Additionally, the vortex moves inboard on the upper surface and outboard on the lower surface due to the span-wise flow induced by lift and slipstream. The sheared and bent vortex system rejoins behind the wing in a complex manner that has not been studied in detail. The bending process is depicted in Figure 2.5.

Thickness Effect So far, the focus has clearly been the propeller effects on the wing. The propeller, however, equally experiences a change in inflow characteristics. A first apparent change is the up-wash in front of a lifting wing. This increased angle of attack leads to a hub lift/propeller normal force component [92]. Thrust, torque and efficiency increase with wing angle of attack and advance ratio [83]. The cause of the effect is shown in part (b) of Figure 2.4. The up-going blade section experiences a decreased rotational velocity and therefore, a reduced angle of attack. The opposite holds for the down-going blade. This results in a periodically changing loading of the blades. The wing up-wash has similar results as equivalent isolated propeller angles of attack. The up-going blade is relieved while down-going blade is further loaded leading to less efficiency at high loadings [78].

Next to the up-wash, the propeller is also influenced by the low-pressure region in front of the wing. It leads to a reduction in axial velocity in close proximity of the wing (see part (a) of Figure 2.4) [83]. This effect varies vertically, also leading to a periodically varying loading of the propeller. Furthermore, the tilted propeller thrust line angle of attack leads to an upflow of the free stream over the propeller plane as can bee seen in part (c) of Figure 2.4 [83].

2.1.4. CLASSICAL PROPELLER INTEGRATION DESIGN VARIABLES

As mentioned before, the stator vane effect, tip vortex attenuation and other phenomena can be used to optimise the aero-propulsive efficiency of the configurations. For this, many design variables can be changed.

Sense of Rotation A first variable to think about is the sense of rotation of the propeller (see Figure 2.3). Many studies have revealed that an inboard-up rotation is beneficial for induced drag reduction. Inboard-up rotating configurations have a better recovery because of the vortex attenuation effect. This is even more pronounced when applying this to a tapered wing because now, a larger part of the wing experiences a drag reduction on the up-going side than the part that is negatively effected by the down-going part [78, 85–87, 94]. Propeller outboard-up motion has, however, been shown to be beneficial at very high loaded propeller [1].

Propeller Positioning The positioning of the propeller with respect to the wing offers a further set of variables. The axial velocity profile of a slipstream is non-uniform and therefore its effect strongly depends on vertical positioning of the propeller [78]. This is shown in Figure 2.3b. Veldhuis found that high positions result in the highest lift coefficients because of an α-increase from slipstream contraction and enhanced dynamic pressure. Drag increases when moving the propeller up or down from the chord line where the doughnut effect (wing less immersed in annulus with highest dynamic pressure) forms a local minimum.

The best L/D is achieved at high positions. A maximum propulsive efficiency is however realised at a slight low installation because of reduced inflow distortion at this location. This is especially the case at high speed conditions [87].

Lateral propeller positioning is a further strong geometric design variable. The effective aspect ratio is found to increase with outboard moving engines (provided inboard up running engines) by attenuating the wing tip vortex effects. The effect is, however relatively insignificant for small variations in lateral positioning [87]. This effect has its maximum when placing the propeller at the core of the wing tip vortex. This special case is discussed in more detail in Section 2.1.5. The drag reduction has been shown to be relatively insensitive to span-wise positioning for usual inboard located engines. This, however, changes for locations closer to the wing-tip where considerable reductions can be achieved [78].

The stream-wise position is a further degree of freedom. Positions farther away from the wing are beneficial for the propulsive efficiency. This can be attributed to the smaller effect of the wing on the propeller inflow meaning less change in angle of attack and less reduction in free stream velocity. The axial velocity on the wing increases significantly when moving the propeller away from the wing. This is simply due to the increase in axial velocity in the slipstream behind the propeller. Therefore, higher lift augmentation is achieved. The higher distortion of the inflow field of the propeller, however, has a smaller effect than the reduced distortion from increased distance, making the propulsive efficiency better for increased distances [87].

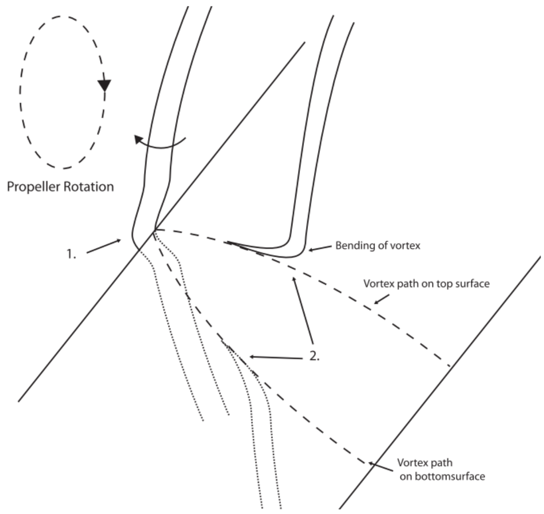

Figure 2.5: Vortex cutting & bending as observed for propeller tip vortices impinging on a lifting surgace [93]

Propeller Inclination Propeller tilt down has been suggested by Veldhuis [94] to reduce wing induced drag. The reasoning behind this approach is that the introduced asymmetry in slipstream velocity distribution is such that the slipstream is increasing the average effective wing angle of attack. By this, more lift is generated and a forward tilt of the force vector reduces induced drag. It should also be mentioned that the reduced propulsive efficiency due to increased inflow distortion and and the slight downward pointing normal force are outweighed by the L/D improvement of the wing at angles below 15 degrees. Additionally, the effect becomes larger when in high speed conditions because of a higher lift increment. Also higher thrust settings strengthen the effect since more up-wash is introduced [78]. Patterson & German [95] developed a simple sectional analysis to approximate the effect of propeller inclination. The results are based on geometric considerations ignoring swirl, finite span, non-linear behaviour, and slipstream non-uniformities. They suggest that an alignment of the propeller with the free stream features the highest lift increase combined with no stall/lift loss tendency because the lift increase is generated by an increase in dynamic pressure and circulation without tilting the lift vector. A downward tilting on the other hand yields a forward tilting of the lift vector leading to less lift but induced thrust. There are, however, also two downsides to this option as a case of propeller failure will lead to a sudden loss in lift and since part of the lift increase is generated by an increase in local angle of attack, the unblown wing fraction operates below its maximum lifting capability. An alignment of the propeller with the chord line is expected to lead to an increase of lift proportional to the increase in local flow velocity.

Wing Geometry Another option is to change the wing geometry. A trefz plane analysis for optimisation of wing geometry showed how e.g. twist distribution can lead to drag reduction although viscous effects pose a limit on this [94]. Similar results can be achieved by chord and/or camber variations. Geometric changes to attain a nearly-elliptic lift distribution, however, is not desirable. It does not yield best performance since no use is made of the stator vane effect [85]. Lower aspect ratio wings benefit more from induced drag reduction in case of inboard up rotation (more washed area, closer to the wing tip) [1].

Propeller Design With increasing thrust coefficient lift and drag coefficients of the wing become less dependent on geometric angle of attack and more local variation in the span-wise load distributions is induced. This has been discovered by George in 1967 [96] and has afterwards been supported by many studies [1, 85]. Wittkowski noticed that higher power leads to higher decrease in drag coefficient and higher increase in lift coefficient. Furthermore, the lift curve slope is increased with power [1]. Wing drag has been found to be smaller when the propeller blade was loaded more towards its inboard sections [96]. Additionally, a higher diameter-to-span ratio leads to higher slipstream recovery [85]. Due to the altered inflow conditions, propellers should be optimised taking into account the wing influence to achieve optimum performance instead of analysing the isolated propeller. The slipstream height is also depending on the propeller diameter leading to higher lift augmentation for higher diameter-to-chord ratios, especially at ratios below 1 [95].

Pusher Configurations Catalano [82] also tested pusher propellers and showed that the lift and pressure drag increase is mainly achieved at the rear part of the wing. Next to the increase velocity at the trailing edge (reducing adverse pressure gradient, postponing transition and separation; while tractor configuration have early transition) also change the upwash angle in front of the wing. Above-chord line installations create the best L/D improvements.

2.1.5. APPLICATION TO DISTRIBUTED PROPULSION

The aero-propulsive interaction for distributed propulsion concepts can differ significantly from the effects of classical tractor propeller configurations. First of all, the number of propulsors can be larger and they can interfere with each other. Secondly, not only tractor propellers but also over-the-wing propellers, pusher propellers and wing-tip-mounted propellers lead to different flow phenomena that dominate the performance of the configuration. This is shown in the following sections with some examples.

With different tasks for individual propellers and possibly also changes in sizing/performance criteria, a change in design philosophy of wing [97] and propulsor [98] is likely. The high-lift propellers (presented in the next section), for example, do not have the primary task of providing thrust but to augment the lift capabilities of the vehicle. Next to that, any negative influence during flight phases where they are not required has to be avoided. This is very different from the classical design goals of maximising thrust and efficiency.

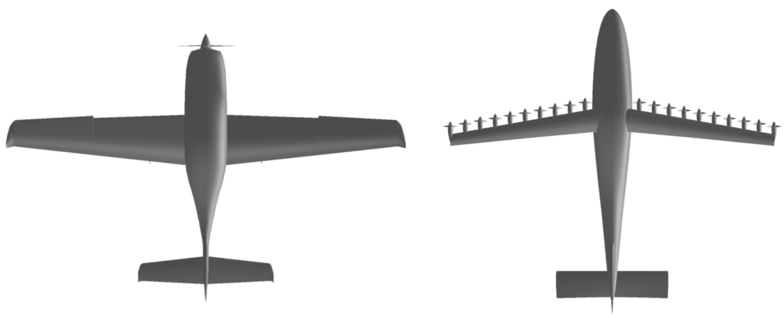

Figure 2.6: LEAPTech wing surface reduction by implementation of high-lift propellers increasing the maximum lift coefficient [99]

High-Lift Propellers Span-wise distributed propellers are commonly referred to as high-lift propellers. These can be located in front of the leading edge, behind the trailing edge or over/under the wing. The general ideas are to a) increase the dynamic pressure over a large portion of the wing, b) make use of thrust vectoring and c) to postpone stall by energizing the flow to increase the maximum lift capability of the wing. For aircraft that have a wing surface area constrained by field performance, this can lead to wing designs more optimal for cruise performance. The LAEPTech project shows this effect on a GA aircraft (see Figure 2.6). The smaller high-aspect ratio wings have reduced drag in cruise and are less gust-sensitive due to a higher wing-loading. The benefit is hence not limited to the take-off and landing conditions but extends over the whole flight envelope. Kuhn [100] showed very early how such configurations can furthermore be used to realise S/VTOL aircraft. He noticed postponed and more gradual stall behaviour and concluded that accepting partial stall on the wing, VTOL aircraft could be realised.

An existing example application of high-lift augmentation by placing multiple propellers in front of the wing is the Airbus A400M (see Figure 2.7). A large fraction of the wing surface is blown by the propellers leading to about as much lift increase as the high-lift devices themselves. In this case, counter-rotating engines with the outboard engine running downward inboard yielded the best performance compromise for cruise and take-off/landing (see Figure 2.7b) [101].

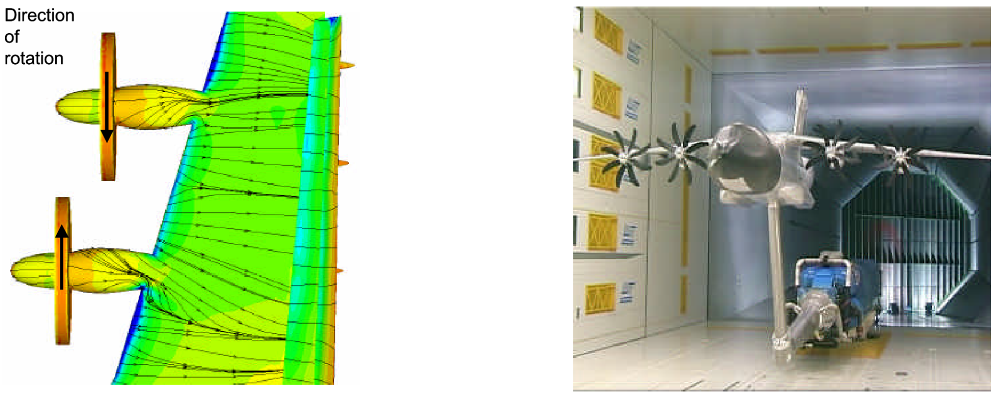

(a) high-lift propellers CFD study

(b) wind-tunnel model

Figure 2.7: A400M propeller integration [101]

In 1956, Kuhn & Draper tested a fully blown wing with two overlapping propellers under different conditions (only one propeller, wind milling, both propellers, different thrust coefficients) [100]. For a first time in 1972, Ting developed a lifting line method which was capable of simulating the effect of multiple propellers in front a wing, showing the large lift increase that can be achieved [102].

Leading-edge or tractor high-lift propellers are most effective in maximising the dynamic pressure over the blown wing part. It has also been shown that a larger blown wing fraction is beneficial. Thrust vectoring either by hinging the nacelle (e.g. Joby S2 [40] as shown in Figures 2.8 and 2.8b) or by installing a variable incident wing (LEAPTech [41]) is largely increasing the usable effect of the lift augmentation because high angles of attack can be flown due to the propeller downwash on the wing.

Pusher configurations are less effective in increasing the dynamic pressure and have the downside of ingesting the wake of the wing (in case of flow separations this is severe) causing noise generation [103]. Over/under-the-wing concepts have the benefit of blowing directly over the flap and can deflect with flap to have good augmented lift but the problem is to mount the concept and that BL from first wing half is ingested [41]. However, next to the increased lifting capabilities, over-the-wing configurations have another interesting characteristic. As shown by Müller et. al. [104], the blown wing fraction can have a negative drag coefficient stemming from a high-velocity region on the leading edge and a significant resulting forward-tilt of the resultant force. It is shown in Chapter 6 how these effects develops when implementing multiple over-the-wing propellers.

With their newly developed vortex-latice XRotor coupling tool, Patterson & German analysed two and four engined configurations. Next to the previously mentioned findings of other authors they identified that contrary to the favourable downward inboard motion of the propellers for minimum induced drag, a four-engined configuration has lowest induced drag for downward outboard rotation. Furthermore, the same required overall power leads to higher lift in case of four engines [88].

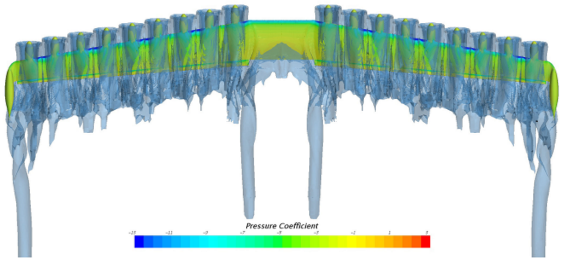

(a) CFD study with actuator discs modelling the propeller [99]

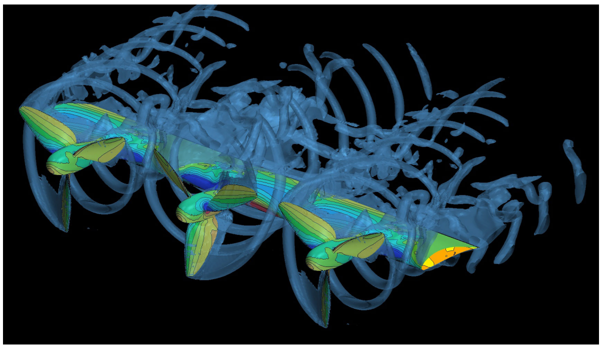

(b) CFD study with meshed propellers[1]

Figure 2.8: (U)RANS simulations of the JOBY S2 high-lift propellers with different means to include propeller effect

The propeller design may have different priorities/requirements for such applications than for standard applications [98, 105]. This is for example the production of little thrust but good lift augmentation for steep descend of DEP concepts. Also wing design may face new challenges as large aspect ratio as well as higher loading from lift augmentation and finally also added mass far outboard can lead to strength and flutter constraints that ultimately increase structural wing weight [106].

Patterson et al. investigated the change in propeller design requirements and developed a design method addressing the new demands. Not only does the main task shift from thrust production to lift augmentation, but the thrust can even be detrimental if the thrust as a side-effect of required lift augmentation is too high to descend at a certain flight speed. To maximise the lift augmentation at as low as possible power, a uniform axial velocity induction is required. Next to this, a high axial velocity is beneficial, directly leading to higher dynamic pressure over the wing. Patterson et al. showed that propellers, designed with their method require 10-20% less power and generate 10-20% less thrust for the same lift augmentation compared to propellers designed for minimum induced loss. The new propeller design method leads to a plateau-shaped induced velocity distribution instead of the typical maximum loading at 3/4 of the blade and features larger-than-usual root chords and twists [107, 108]. Although smaller propellers have the ability to provide higher axial velocities over the span, the slipstream hight also affects the achievable lift. It was found that propeller diameters close to chord length may be a good compromise [95].

The many factors involved in the assessment of a high-lift propeller concept plane make the selection of the size and number of propellers a difficult task. Factors favouring high numbers of propellers are stall speed and yaw moment with OEI or nacelle drag. Factors in favour of fewer engines are the chance of OEI and average swirl angle. Other metrics like total power have a local minimum. Additional, non-quantifiable factors like commercial availability of the components and complexity are further complicating the decision. In the analysed case by Patterson et al., the optimum number was between 12-16 but this may be different for a change in wing and propeller design [108]. A semi-analytical method for the estimation of the attainable lift coefficients, calibrated with CFD results and depending on aspect ratio, thrust, blown wing fraction, and aspect ratio of blown wing fraction per slipstream is given by Stoll and Mikic [60]. Stoll et al. found in a different study that the studied GA wing attained a maximum lift coefficient of 5.2 and a small lift gradient due to the propeller down-wash. The resulting wing geometry that is optimised more towards cruise conditions raised the aircraft lift-to-drag ratio from 11 to 20, showing the large performance improvement opportunities using DEP [99].

Fu analysed a UAV with distributed tractor propellers with multi frames of reference CFD simulations and observed a change in local angle of attack as well as increased dynamic pressure on the wake-immersed wing

[1]JOBY Aviation: LEAPTech. 2016. URL: http://www.jobyaviation.com/LEAPTech/, online, accessed March 16, 2017.

fractions leading to increased lift and drag [109].

Wing-Tip Propellers The idea of wing-tip propellers can be dated back to the 60s and tries to make use of the interaction of the tip-vortex of the wing and the slipstream of the propeller. Snyder showed in experiments that a wing-tip mounted tractor propeller counter-rotating to the tip vortex shifts this vortex downward and outboard. The increased effective aspect ratio reduces the induced drag. Furthermore, the wing lift is increased by having local upwash as well as increase dynamic pressure at the wing tip. Both force alterations are increasingly strong the further outboard the propeller is shifted [90].

Patterson showed in 1970 that a non-circulatory flow from a jet engine can also reduce the tip vorticity leading to decreased induced drag. This is achieved by releasing the high energy jet wake into the tip vortex and thereby dissipating energy from the tip vortex and reducing the downwash behind the wing [110]. Later he showed by experiment that a wing-tip mounted pusher propeller equally benefit by recovering part of the vortex energy and gaining additional thrust from the inflow swirl component (see Figure 2.9a). At that time, the integration of tractor propellers was regarded as a penalty and a pusher configuration was supposed to avoid this issue. An up to 25% reduction in required power and an induced drag reduction of up to 30% was achieved [89, 111].

1984, Loth & Loth tried to approximate the possible induced drag reduction of tip mounted propellers analytically and found that savings up to 10% could be achievable [91]. Their experiments did however not support their claims and Miranda & Brennan two years later published an article pointing out some mistakes and giving an alternative analysis [86]. The results of their inviscid code lead to a generalised stagger theorem stating that the thrust minus drag of tractor and pusher configurations is the same but higher than for the individual components. But in the tractor case, the benefit is observed as a drag reduction while the pusher case features improved thrust values. In Chapter 6, it will be shown in how far this statement holds for viscous simulations. The results also showed that the optimum lift distribution for wing-tip mounted propeller concepts is close to the elliptical one except for a slight pronunciation of the tip loading. A further observation was that high advance ratios are beneficial for the drag reduction. They also stress that no concrete number can be mentioned that can be achieved because it largely depends on a number of design variables. They found the most influential factors to be the advance ratio (with drag proportionally decreasing with increasing advance ratio) and the propeller diameter/disk loading (with increasing disk loading leading to higher drag reductions). Furthermore, the drag reduction has been shown to reduce linearly with increasing lift coefficient and to be stronger at lower aspect ratios.

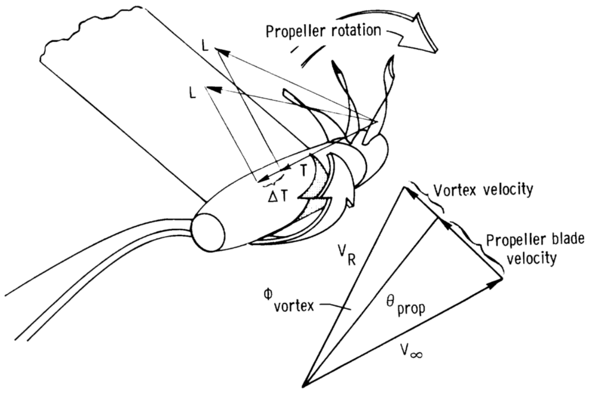

(a) Wing-tip pusher propeller experiencing increased thrust from wing-tip vortex inflow swirl [89]

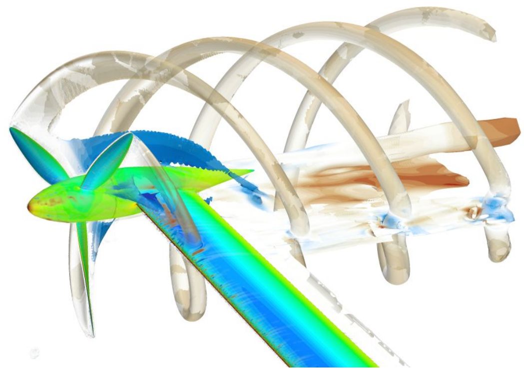

(b) Joby wing-tip tractor propeller CFD simulation showing wing drag reduction due to slipstream effect on wing[2]

Figure 2.9: Interaction between tip-mounted propellers and wings for pusher and tractor configurations

The idea has so far not been implemented because large heavy engines at the wing-tip are detrimental to

[2]Stoll, Alex M.: Promise for an electric propulsion aircraft future. SAE International, 2016, URL: `http://articles.sae.org/14580/`, online, accessed March 15, 2017.

the wings' aeroelastic performance. This is believed to change by incorporating smaller electric engines. Additionally, concerns on the directional stability of such a configuration have been raised in case of a OEI scenario [90, 111]. More recently, new energy came into the research of wing-tip mounted propellers because of the good integration opportunities into distributed propulsion concepts [39, 57]. Borer et al. show that the Sceptor concept can benefit between 5-10% in cruise lift-to-drag ratio on aircraft level with installing wing-tip mounted propellers [39]. Further, Dimchev analysed the low speed application for small aspect ratio UAVs and found relevant lift increase and drag reduction [112]. Candade recently studied the interaction of a horizontal tail with tip-mounted propellers and found that the effectiveness of the elevator was significantly increased while there was no significant change in thrust and drag measured [59].

Stoll and Mikic [60] found with CFD for their GA study that the power requirement on the tip-propellers is reduced by the fraction of total drag minus 34% of induced drag and the total drag. The effect of drag reduction strongly depends on the flight conditions. For different speeds there are different optimal thrust coefficients that lead to the best drag reduction. This can be achieved by controlling the thrust of the wing-tip mounted propellers and producing the remaining thrust requirement with other propellers. Figure 2.9 shows a URANS simulation visualisation of a configuration studied by Stoll. Borer gives a development background/history and simulated configurations with (U)RANS and RANS-actuator disk coupling to see the effects [113]. He also notes that as for high-lift propellers also wing-tip propellers can have non-thrust-centric designs [98].

It should be noted that the mentioned savings in drag are based on very different assumptions. If the reference wing is a rectangular wing with low aspect ratio, the savings in induced drag are enormous (of the order 20-30%). This is different for a wing with high aspect ratio where the drag is only reduced by 5-10%. When compared on aircraft level, this number is even smaller (in the order of several percent) as the wing drag is a smaller fraction of total aircraft drag. However, even these remaining percentages on aircraft level are significant compared to envisioned benefits by other new technologies.

2.2. SIMULATION STRATEGIES

Because of the strong need to accurately predict the aerodynamic performance of wings, propellers and their interaction, numerous simulation techniques have evolved over the years. These techniques vary largely in their complexity, their accuracy and their computational costs. More complex and expensive methods for the precise analysis of the physics and detailed design could be realised with the increase of available computational power. Still, cheaper methods are required for design space exploration and design optimisation. This leads to a large variety in available codes that all have their up- and downsides. In the following, an overview of the aerodynamic simulation strategies is presented. It should be noted that the purpose of this chapter is not to present every method in detail as this would fill several books. Instead, an overview and comparison is presented with some focus on the methods relevant to the proposed research project.

Lifting surfaces can be analysed with many different tools. This ranges from simple lifting line codes to sophisticated CFD methods. As for wings, vortex based methods are often used to simulate the aerodynamics of propellers. The most widely used group of methods, however, is a more simplified approach making use of actuator disk and momentum theory. At the higher end, also CFD tools are increasingly used to analyse propellers [114]. For conventional configurations, time-averaged simulation methods were found to be very accurate although a propeller clearly features unsteady aerodynamic phenomena [78, 86, 115, 116].

One-Way and Two-Way Interaction Before going into the different methods, some categories can be established to differentiate between them. This can for example be done by looking at what direction of interaction is taken into account. One-way interaction considers only the effect of one component onto the other but not vice-versa. For propeller-wing interaction, this means that either the propeller is modelled in isolated conditions and its effects on the flow over the wing is modelled. Hence, the propeller performance does not take into account the effect of the wing on the flowfield. Vice versa, it can also be the case that the wing is modelled in isolated conditions and only the propeller is analysed taking into account the wing effect on the flowfield. Two-way interaction goes one step further and takes into account both, the effect of the propeller on the wing as well as the effect of the wing on the propeller.

Homogeneous and Hybrid Methods Furthermore, the methods can be divided into homogeneous and hybrid ones. A homogeneous method models both, the wing and the propeller in the same way. An example is a combined unsteady CFD simulation where the whole system is solved at once. In contrast to that, hybrid methods have been developed to reduce the computational costs compared to homogeneous methods by limiting the analysis of each component to the required capabilities. The example most relevant for this project is the RANS body force approach, where the propeller is modelled with a simple BEM/lifting line/lifting surface method and coupled to a RANS simulation of the rest of the system with a body force approach. This eliminates the requirement for an unsteady RANS simulation for fully viscous analyses. These hybrid methods however can differ in their ways of interaction. In case of a two-way interaction coupling, the propeller may first be analysed in isolated conditions. Afterwards, the RANS simulation is done giving a new flowfield for the propeller. This will require several iterations until a converged state is achieved.

Table 2.1 summarises the characteristics of the methods described in the following. The three methods used throughout the project are highlighted. Clearly, URANS simulations offer the best coverage of effects and high accuracy at high computational and processing costs. The vorticiy based methods require little effort and are fast. With increasing complexity to cover more effects and larger numbers of propellers, however, the computational costs can become as large as for URANS computations without offering the same level of accuracy. The coupled RANS approaches, combine the two simulation strategies by implementing the propellers either with actuator discs or with body-forces. Especially at higher numbers of propellers, this approach has a relatively low computational cost whilst offering accurate results. Important to note is also the preprocessing effort for a RANS-BF method which is in fact not much smaller compared to a URANS simulation initially. However, design studies with changing blade geometry etc. are easily done without a need to re-mesh to configuration.

Table 2.1: Comparison of selected simulation strategies for distributed propeller-wing configurations

category	**lifting-line**	panel methods	VLM	**URANS**	RANS-AD	**RANS-BF**
viscous effects	(✓)	(✓)	(✓)	✓	✓	✓
radial flow effects	(✓)	(✓)	(✓)	✓	(✓)	(✓)
thickness effects	✗	✓	✗	✓	✓	✓
two-way interaction	✓	✓	✓	✓	✓	✓
low computational costs	(✓)	(✓)	(✓)	✗	(✓)	(✓)
little pre-/post-processing	✓	✓	✓	✗	(✓)	(✓)
accurate slipstream model	(✓)	(✓)	(✓)	✓	(✓)	✓
accurate drag prediction	✗	✗	✗	✓	✓	✓
accurate propeller perf.	(✓)	(✓)	(✓)	✓	(✓)	(✓)

2.2.1. VORTEX THEORY BASED METHODS

Lifting Line Methods Prandtl's lifting line method [117] was the first practical method to predict finite wing aerodynamics. It is a potential flow method where bound horseshoe vortices are placed along a lifting line, giving this technique its name. The resulting vortex sheet extends behind the wing. Span-wise loading distribution, induced drag and the trailing vortex system can be resolved. The theory is able to model moderate wing sweep (if extended acc. to Weissinger [118]) but is limited to high aspect ratio planforms and small angles of attack. Viscous drag is not included and has to be determined with additional means. Important results from lifting line theory are among others the decreased lift curve slope and increased induced drag for smaller aspect ratio wings. The very low computational cost to get quick estimates of wing circulation makes this method to be used a lot until this day. The fast method is limited to small sweep angles, neglects thickness effects and fails to predict low aspect ratio wing characteristics [58, 73, 119].

Lifting Surface/Panel Methods Still working with potential flow theory, the lifting surface or panel codes that are available are an extension of the lifting line model that uses vortex lines in chord and span-wise direction. Different distributions of singularities have been used to solve the flow equations. Ignoring the thickness of the wing, traditional variants place the singularities on either the mean camber or the chord line . More complex three-dimensional shapes can be represented by panels over the geometry surface [58, 119].

The method variety is large. Firstly, the type of singularities are either sources, doublets, vortices or a combination of these. Secondly, different boundary conditions can be applied. Thirdly, different wake models extist. Fourthly, the discretisation of both geometry and singularity strength can be chosen differently (e.g. with piece-wise polynomials). Finally, numerical considerations play an important role. Cut-off distances to avoid numerical singularities and division of the domain into near and far field to improve computational efficiency can be included [119]. In contrast to lifting line codes, these methods can assess higher sweep angle geometries and, in case of panel codes, also take thickness into account. This, however, comes at higher computational costs.

Vortex Latice Method Vortex latice codes are widely used and place a number of horseshoe-vortices on the wing surface. Vortex lattice methods and panel methods show similarities in that surfaces are discretised by distributing singularities on them and the strengths of these are determined by solving a system of linear algebraic equations. On the other hand, the differences are that a) its focus lies on lifting effects and it normally ignores thickness, b) boundary conditions are specified on a mean surface and the result is the pressure difference instead of upper and lower surface pressures, c) the horse-shoe vortices are not placed on the complete surface, and d) the combination of multiple surfaces is a typical application [120, 121].

Adding Viscous Drag An often used approach to add viscous drag terms in the potential flow analysis is the strip theory. According to this, a slender body can be divided into 2D strips. Either known 2D characteristics of the sections from experiments (e.g. Witkoswski in his VLM code [1] or Cho & Cho in their coupled lifting surface-VLM code [122]) or a 2D solver (e.g. flat plate friction with form factors, Xfoil, etc.) can be used. The integrated 2D coefficients over the span are an approximation of the 3D coefficients.

Application to propellers The general principle of lifting line methods as proposed by Prandtl [117] has already been discussed. Goldstein presented a formulation for the analysis of propellers [79]. In the approach, lifting lines model the blades with radially varying circulation. Theodorsen [123] included the capability to model heavily loaded propellers and Clark [124] added a free wake model to improve the results for such high loadings. As for non-rotating wings, limitations are the inviscid nature of the technique as well as the lack of thickness effect modelling. Also as described for wings, lifting surface methods model the propeller blades by a vorticity distribution on the camber/chord line of the blades allowing for blade sweep while panel methods also account for thickness by modelling the blades as vortex panels on the surface [125]. As noted by Gur & Rosen [126], all of these methods give just as good results as BEM simulations for simple geometries in forward flight. For more complex flows (e.g. flying at an angle or hovering), however, higher fidelity methods are required to capture important effects.

Because of its simplicity, availability and comparably little computational costs, a lifting-line code will be used in subsequent chapters in two different ways. First of all, as a fast tool to simulate propeller-wing combinations with a free-wake approach. For this, wing and propeller blades are discretised as lifting lines. The details of this approach are described in Chapter 4. Secondly, the higher-fidelity body-force method used during this project requires a propeller model which will be a lifting-line model without wake as will be explained at the end of this Chapter (also see Figure 2.10). The implementation will be explained in detail in Chapter 4.

2.2.2. CFD METHODS

By numerically solving the Navier Stokes equations (or the inviscid Euler equations), the flow around a defined geometry in a specified condition can be determined. This requires not only to define the geometry and the inflow conditions but a meshing of the entire domain as well as specifications of the boundary conditions. Since, the entire domain is solved for all flow quantities, a lot more information than from vortex based methods is available. This information is, however, not directly available and adds post-processing time to the already large pre-processing and simulation durations [58].

Unsteady simulations are required when having fixed and rotating surfaces. They are also necessary if the time-dependent flow behaviour like the helical vortex formation is to be studied. This increases the computational cost of this option to a large extend. Additionally, the added meshing of the propeller adds to the preprocessing effort. This leads to a rather little application if this technique for propeller-wing interaction despite its ability to resolve in detail all important flow features [93]. Some examples are the Euler simulations by Thom and Janus [93, 127] as well as the URANS study of Roosenboom [128] who compared his results to PIV measurements noticing very good agreement apart from the numerical diffusion leading to dissipation of vortical flow structures even for inviscid finely resolved examples. Therefore, URANS simulations will be used later in the report for the validation of other simulation strategies. The reader is assumed to have a basic background knowledge on CFD methods so no further discussion on this topic is given.

2.2.3. COUPLED METHODS

Since Jameson [129] studied the interactions of wings and propellers for a VTOL configuration using a deflected slipstream analysis, many studies have been published on modelling the relevant interaction effects [93]. Miranda et al. proposed to use a vortex tube model of the slipstream acting on the wing [120], Cho and Cho [122] chose a coupled vortex-latice panel code, and Lotsted [115] used an Euler code with a body force representation of the propeller. Roosenboom [128] simulated configurations with uRANS. The previously described models for wing and propeller simulation can be used and be coupled to analyse propeller-wing configurations leading to even more possible coupled codes. This variety allows to chose for a suitable method for a certain problem and given computational power and/or time. Basic principles, capabilities and restrictions of these models are given in the subsequent sections.

COUPLED VORTEX BASED METHODS

The vast majority of aerodynamic analysis tools to study the interference of propellers and wings make use of the vortex theory. Jameson developed lifting line and lifting surface codes that take into account elliptic slipstreams in 1968 and 1970 [129, 130]. 1975, Mcveigh coupled a BEM code with a lifting line code [131]. 1982, Aljabri combined the Goldstein slipstream theory with a panel code [116]. A vortex latice code for the propellers and a vortex latice code for the wing with fixed wake was used by Witkowski in 1989 [1]. In the 1990s and 2000s more variations appeared (e.g. BEM-panel code by Lötsteadt [115], BEM-free wake lifting line code by Ardito Marretta [132], lifting line-lifting line free wake code by Ardito Maretta [133], vortex latice-panel code by Cho [122], BEM-fixed wake lifting line code by Veldhuis [78], BEM-lifting line code by Hunsaker [134], BEM-fixed wake panel code [45]).

The large variety in these couplings represents the improvement in computational power on the one hand, and the different requirements on the capabilities/speed of the individual codes. It can be seen that the first codes assumed propeller performance and slipstreams and just tried to find out what the effect on the wing aerodynamics would be. Later, arbitrary propellers were studied by implementing BEM or vortex based codes. This also allows the modelling of two-way interaction. Recently, further codes have been published or are under development that are also capable of analysing the interaction between many propellers and lifting surfaces. These are aiming at serving as design space exploration and/or MDO routines for future (distributed propulsion) aircraft concepts. Among these are the vortex particle method by Calabretta and Willis [135, 136], a distributed vorticity elements code by Patterson [58], a BEM-fixed wake panel code by Ferraro [137] and a lifting line-vortex latice code by Alba [138]. None of them, however, is suitable to study the fundamental principles behind distributed propulsion as important factors like viscous effects and (apart from panel codes) the presence of a solid body are not covered.

COUPLED CFD-BASED SIMULATIONS

With the help of CFD tools arbitrary geometries and viscous effects can be modelled. When coupling simplified propeller models to a RANS simulations, the use of rotating reference frames and unsteady simulations is avoided. The RANS equations are solved and the propeller is modelled externally. The RANS simulation can introduce the effect of the propeller in different ways. Either, an actuator disc is modelled that imposes a pressure/velocity jump boundary condition at the propeller plane or body forces are included in the momentum equation. The propeller can be modelled with all kinds of methods (from BEM to panel codes), all requiring slightly different approaches for the implementation. Both approaches are detailed in the following.

Actuator Disc Boundary Condition The simplest coupled interaction method uses a RANS simulation for the lifting surface and models the propellers as actuator discs. These actuator discs are implemented in the simulation as pressure [139] or velocity [140] jump boundary conditions. The terms that are imposed at the boundary conditions for the velocity jump represent an axial, a tangential and a radial component. With this form, a radial loading distribution can be modelled. The increments are only a function of the free stream velocity, radial position, rotational speed, blade number, element thrust, tangential induced velocity in the far wake and the induced axial velocity at the propeller plane. These quantities are all known or can be derived from the actuator disc theory [140].

In both cases, the propeller model needs an initial inflow velocity to determine the induced velocities/pressure jump of the propeller. Afterwards, the RANS simulation is run with the actuator disc boundary condition giving a new inflow velocity for the propeller model. This system has to be iterated until the inflow does not change any more.

A clear benefit of the boundary condition approach is the easy implementation procedure. The fan boundary conditions in the commercial CFD software FLUENT[3], for example, as used by Lino [140] facilitates quick implementation of the jump terms. The described velocity jump approach does take into account variations in axial, radial and tangential directions. Hence, effects like slipstream swirl and contraction can adequately be represented. This is not the case in the pressure jump variant where the swirl component is not included. This will influence the result of the RANS simulation significantly and does not allow to analyse major effects of propeller wing interaction. Further, by having only a radial variation in induced velocity/pressure change no asymmetric loading of the propeller is represented in the slipstream. This will again influence the flow experienced by the wing and therefore change the result.

Body Force Approach The body-force approach is a second way to couple simple momentum or vortex-based methods for the propeller simulation to CFD computations. The body forces are included as volumetric source-terms in the RANS equations. To the author's knowledge, Sparenberg [141] did the first coupling method with an actuator disk after preliminary work of other researchers. Also Schetz & Favin [142, 143] brought the approach forward by analysing ship-propeller interaction. Whitfield et al. [144] have made use of the method in 1983 by studying propeller-wing interaction with an Euler code that simulated the propeller by including body-forces from known propeller performance data. Further work to mention are the studies by Stern et al. [145, 146] using a coupled vortex latice code and Zawadzki [147] using unsteady BEM.

In the beginning, the body-force approach was mainly used to simulate propeller-hull-rudder interaction in ship engineering [139, 141–143, 145–154]. These codes all couple different propeller simulation models (BEM, lifting line & lifting surface) to a RANS solver by means of body forces. With regard to aircraft design, it took until very recently that the method attracted the attention of more users. The analysis of BWBs with distributed propulsion was performed by Liu and Rong in 2013 and 2016 [28, 155]. Chadha used an actuator disc-RANS coupling in 2016 to analyse propeller-wing interaction effects [156] (also done by Borer [113]).

The procedure of Rijpkema et al. [151] has a non-integrated propeller model. The RANS simulation is first run without the propeller effect. Afterwards, the nominal wake field at the propeller plane is determined and used for the propeller model as inflow field. The model, in this case, is an unsteady BEM method that feeds back a time-averaged non-uniform force distribution. The force distribution is now interpolated onto the RANS grid with body forces in the volume swept by the blades. Different methods for this force redistribution can be used as discussed by Starke & Bosschers [157]. Proceeding the next RANS simulation, a new total wake field can be derived and by subtracting the time-averaged induced velocities from the BEM simulation, the effective wake field is found. This is the new inflow field for the BEM simulation. This procedure is then repeated until convergence of the effective wake field is reached. The methods of Starke & Bosschers [157] and Simonsen & Strern [153] follow a similar approach but the latter make use of a potential flow propeller

[3]ANSYS: Ansys Fluent. 2017. URL: `http://www.ansys.com/Products/Fluids/ANSYS-Fluent`, online, accessed April 5, 2017.

model instead of a BEM analysis. Also their convergence criterion differs and is composed of x-force balance, propeller rotational speed and loading distribution.

Methods by Wöckner-Kluwe [158] and Greve [152] employ a more integrated (implicit) coupling approach. Only one URANS simulation is run. A first iteration without propeller is needed to have an initial flow field and afterwards, the propeller model is updated at each time step. An additional feature of Wöckner-Kluwe's methodology is the more elaborate representation of the blades in the URANS simulation. Instead of always applying the time-averaged force distribution of the propeller panel code to the flow, the forces are applied at the current blade positions that are adapted every time-step. This facilitates a more accurate capturing of ventilating or submerged propellers. The continuity equation remains unchanged as no additional mass is added by the propeller (see Equation 2.5 which states that the rate of change of mass in the control volume equals the flux of mass across the volume's boundary). The volumetric body forces (**b**) are included in the momentum equation as shown in Equation 2.6. The resulting discrete force distribution induces the velocity and pressure changes that are known from the propeller momentum theory [158].

$$\frac{\partial}{\partial t}\int_V \rho dV = -\int_S \rho \mathbf{v}\cdot\mathbf{n} dS \tag{2.5}$$

$$\frac{\partial}{\partial t}\int_V \rho \mathbf{v} dV + \int_S \rho \mathbf{v}\mathbf{v}\cdot\mathbf{n} dS = \int_S T\cdot\mathbf{n} dS + \int_V \rho \mathbf{b} dV \tag{2.6}$$

The first term on the left-hand side of Equation 2.6 represents the rate of change of momentum in the control volume. The flux of momentum through the control volume's boundaries is included as the second term. On the right-hand side the stress forces (T being the stress tensor) acting on the boundary and the body forces acting on the volume are included. It is the last term that is prescribed by the propeller body-force model. The energy equation is shown in Equation 2.7. The first term on the left-hand side is the sum of internal and external energy contained in the volume. The second term represents the flow of internal and external energy accross the volume's boundaries. The right-hand side includes the work done by stresses (T being the stress tensor) as well as by heat flux (**q** being the heat flux vector) at the boundary. Finally, the work done by the body forces of the propeller model is included as the last term.

$$\frac{\partial}{\partial t}\int_V \rho(e+k) dV + \int_S \rho \mathbf{v}\left(e+\frac{P}{\rho}+k\right)\cdot\mathbf{n} dS = \int_S (T\cdot\mathbf{v}-\mathbf{q})\cdot\mathbf{n} dS + \int_V \rho \mathbf{b}\cdot\mathbf{v} dV \tag{2.7}$$

Work by Thom [93] showed that an actuator disk model, as expected, does not resolve the tip vortex structures of the propeller, greatly simplifying the computations. Furthermore, he notes that the artificial viscosity to stabilise the simulation has a non-negligible effect on the results because of early dissipation of the vortical structures. However, the combined work of the previously mentioned authors shows that the body force approach is well capable of predicting propeller-lifting surface interactions for the considered configurations with significantly reduced effort at comparable accuracy as URANS simulations.

The body-force approach will be used in the following to model the interaction of multiple propellers and the airframe. The approach in this thesis (as shown schematically for a wing-tip mounted propeller in Figure 2.10) will be the coupling of a lifting-line code and a RANS solver. However, contrary to the majority of the previously described implementations, this coupling will not work with an effective wake field. When running a code that calculates the induced velocities, these have to be substracted from the RANS flow field to avoid taking them into account twice. A second possibility is to not let the propeller model calculate induced velocities since they are already included in the RANS flow field that it uses as input. This approach is taken in the following chapters. While the problem for the effective wake field is where to determine the field to avoid singularity effects, the problem shifts to a proper chord-wise distribution of the body-forces to obtain the correct induced velocities at the propeller disc. This will become more clear in Chapter 4. Before diving into the implementation of the method, a closer look on the configurations of interest is taken in Chapter 3 to understand why the method is designed as presented subsequently and how it will be used.

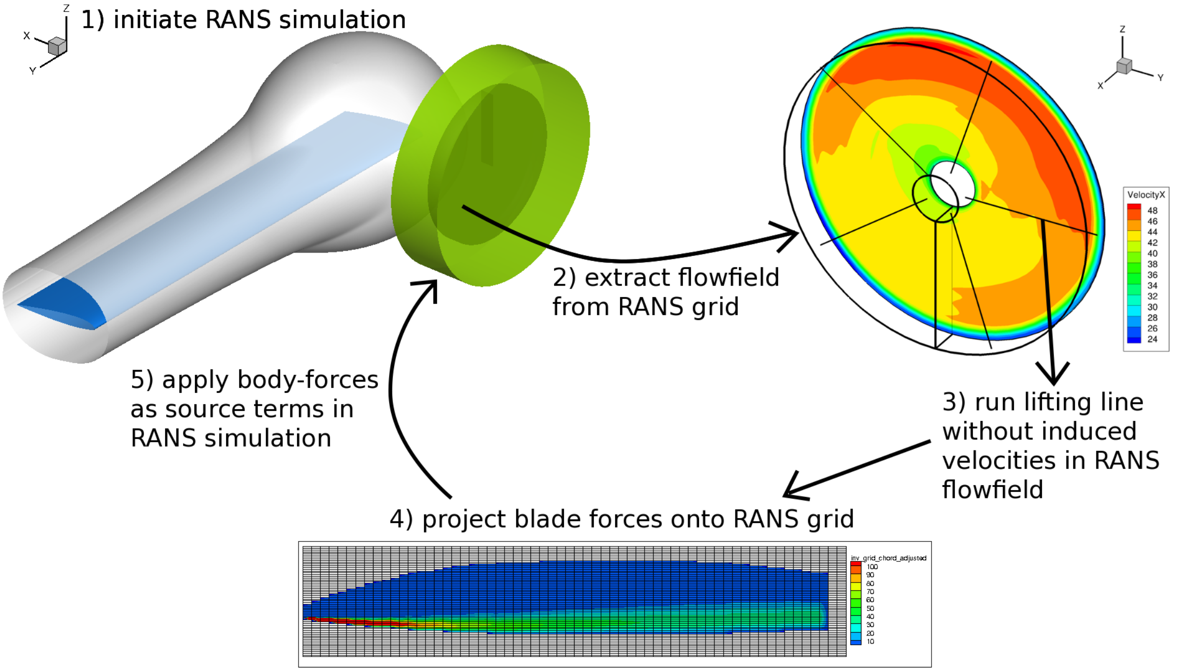

Figure 2.10: Body-force approach coupling procedure schematic

3

Configurations and Conditions

To study the general flow physics and trends connected to distributed propulsion, a reference geometry is required that can be analysed under a selected set of conditions with the different aerodynamic tools. For this purpose, a representative flight condition, a propeller design and a wing design are presented in the following sections.

3.1. Flight Conditions

First of all, the flight conditions are presented. The type of aircraft under consideration is a short range commuter flying in highly congested areas and is expected to fly at low altitudes close to sea level. This is why ISA sea level conditions are assumed for all calculations. Furthermore, the maximum expected travel speed of these vehicles is $M = 0.3$ in cruise as could be observed for the proposed configurations in literature. The high-lift velocity is assumed to be 61 kts or $M = 0.092$ being a stall speed limit in the FAR Part 23 regulations[1]. As has been shown in the introductory chapters, one benefit of the introduction of DEP configurations is the ability to fly at higher wing loadings. The wing is hence assumed to fly at a lift coefficient of 0.6, higher than that of most current general aviation aircraft.

Table 3.1: Flight conditions selected for cruise and high-lift flight phases as used in the subsequent chapters

variable	**cruise**	**high-lift**
M [-]	0.3	0.092
v [m/s]	102.1	31.4
ρ [kg/m^3]	1.225	1.225
T [K]	288.15	288.15
P [Pa]	101325	101325
ν [Pa/s]	$1.81 \cdot 10^5$	$1.81 \cdot 10^5$
Re [-]	$6.9 \cdot 10^6$	$2.2 \cdot 10^6$

3.2. Propeller Design

The propeller implemented as wing-tip propeller is designed according to Adkins et al. [81] for a tip radius of 0.8 meters, three blades, a hub radius of 0.12 meters, a tip Mach number of 0.5, and a target thrust of 1800N. The tip Mach number is a compromise between propeller performance and the increased noise levels at higher speeds. The resulting shape is altered for finite root/tip chords and a smoother chord distribution

[1] Federal Aviation Administration: Small Airplanes Regulations, Policies & Guidance. URL: `https://www.faa.gov/aircraft/air_cert/design_approvals/small_airplanes/small_airplanes_regs/`, online, accessed November 11, 2017

according to Borer et al. [105]. The airfoils used in the propeller design are ONERA internal propeller airfoils for which tabulated data from 2D viscous CFD simulations is available. Six different airfoils are used as tabulated in Table 3.2. The undisclosed airfoil shapes and performance data are not presented in this report. The propeller design procedure was already in place at the beginning of the project.

Figure 3.1a shows a three-dimensional view of the propeller. The propeller has no sweep or dihedral. The untwisted blade shape as well as thickness, twist, and chord distributions are presented in Figures 3.1b to 3.1e.

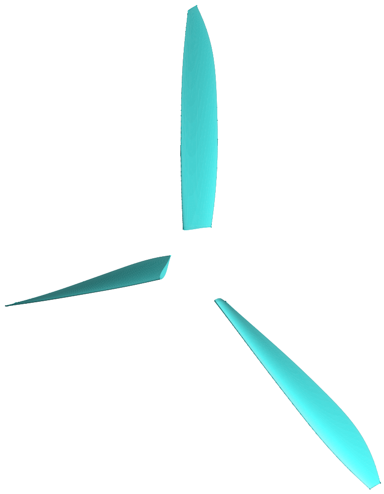

(a) Isometric view

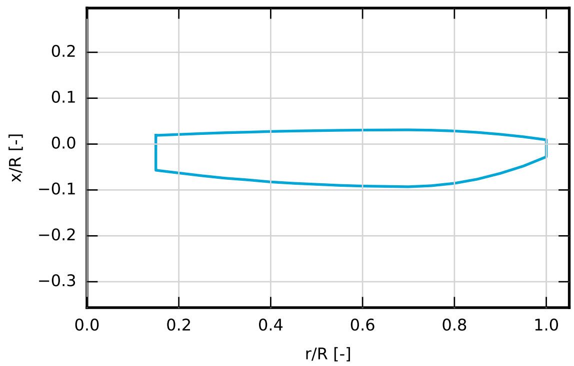

(b) Untwisted blade shape

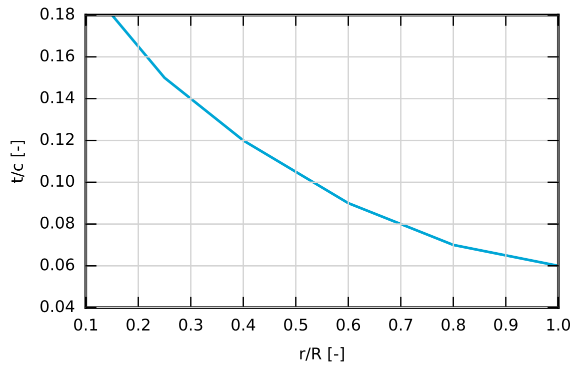

(c) Thickness distribution

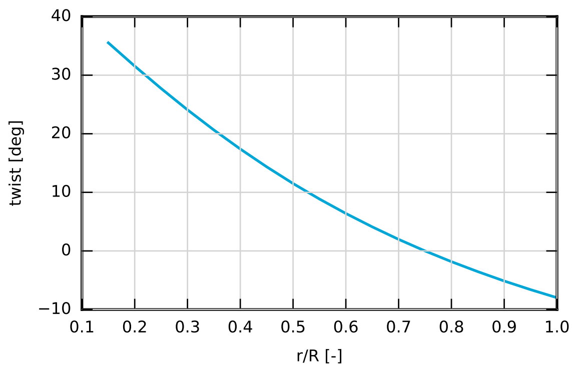

(d) Twist distribution

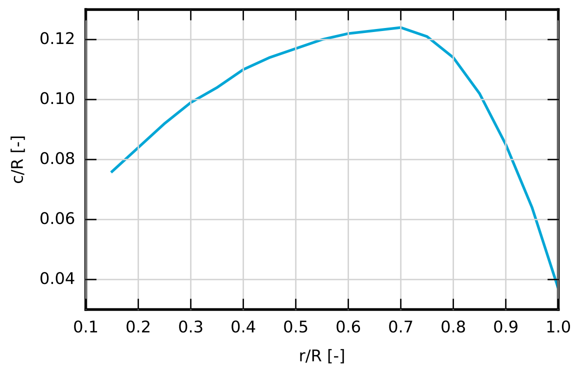

(e) Chord distribution

Figure 3.1: Geometry definition of minimum induced loss propeller designed acc. to Adkins et al. [81] (assuming $R_{tip} = 0.8$m, $R_{hub} = 0.12$m, $M_{tip} = 0.5$, $M_{\infty} = 0.3$, $T = 1800$N, applied finite tip chord and Borer smoothing method [105]) showing an isometric view, the untwisted blade shape, thickness distribution, twist distribution and chord distribution

Table 3.2: ONERA propeller airfoils used throughout remainder of the report

name	t/c [-]	r/R [-]
OH2318 [-]	0.18	0.15
OH2315 [-]	0.15	0.25
OH2312 [-]	0.12	0.40
OH2309 [-]	0.09	0.60
OH2307 [-]	0.07	0.80
OH2306 [-]	0.06	1.00

An advance ratio sweep was performed with the free-wake lifting-line code PUMA under the specified cruise conditions to obtain the isolated propeller performance. The results are presented in Figure 3.2. The used advance ratio in the following sections is 1.884 as a result of the assumed free stream and propeller tip Mach number.

The propellers used as lift-augmenting propellers have been designed with the same methodology according to Adkins et al. The same tip Mach number and tip-to-hub radius ratio were used ($M_{tip} = 0.5$ & $r_{hub}/r_{tip} = 0.15$). However, they differ in their geometry depending on the required size and disk loading. Also no chord distribution smoothing as described for the wing-tip propeller was applied. The size is determined using the number of propellers, the spacing between the propellers and the free wing span. The spacing is set to 10% of the propeller diameter. So far, no clear indication of an ideal spacing is given in literature such that a first guess had to be made. Further, the free wing span is assumed to be 88% of the total span, leaving a space for the integration on the fuselage of 1.8m. A five-bladed design is assumed to allow for a higher disk loading. A certain assumed disk loading defines the thrust for which the propeller is designed.

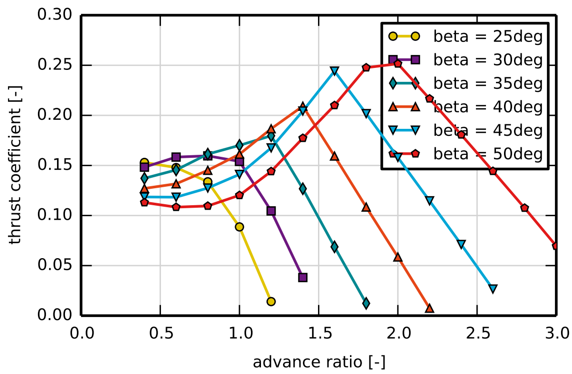

(a) Thrust map

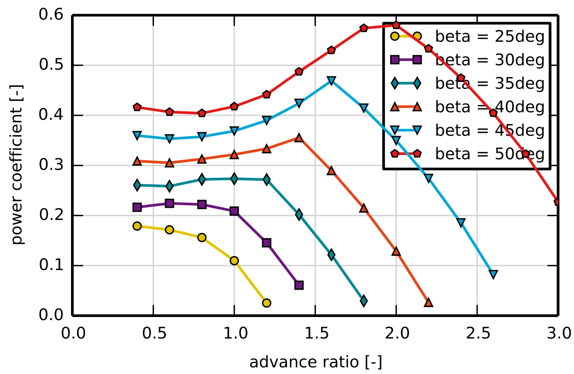

(b) Power map

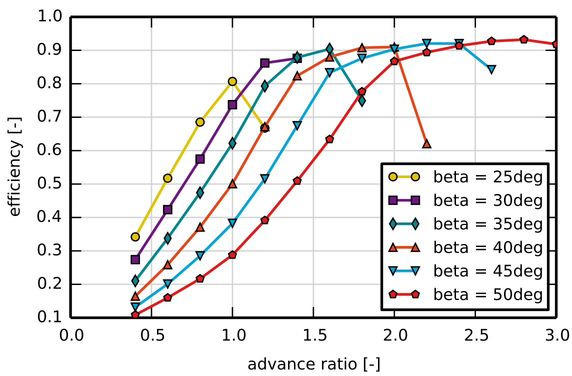

(c) Performance map

Figure 3.2: Isolated performance of the minimum induced loss propeller showing the thrust, power and performance maps as obtained with free-wake lifting-line simulations for pitch angles between 25 and 50 degrees

No hub is used for the propeller. This is justified for the body-force and lifting-line codes both having a model for free/end-plate options for lifting surface ends. For the meshed propeller, this is less easily justified since the root sections will behave differently. However, the effect on propeller & wing performance is barely visible when comparing to body-force results as will become apparent in Chapter 5. Furthermore, the meshed propeller simulations are only a reference for validation. Hence, the effort of implementing a hub is not justified for this project. It should be mentioned, however, that for actual designs for future concepts this assumption cannot be made. While the current study is interested in relative trends and general interaction effects, the effect of a propeller support structure are non-negligible for design studies requiring accurate absolute performance predictions.

3.3. WING GEOMETRY

The wing geometry is defined by a NACA23012 airfoil, being a popular airfoil suited for applications as considered in this project. First, an untwisted, untapered and unswept wing is assumed. Later, an ideal twist distribution computed for the isolated wing without propeller according to Phillips et. al [159] is added. Phillips showed that with the presented method, a wing with arbitrary planform achieves the same minimum drag as an untwisted elliptic wing with the same aspect ratio. With Equation 3.1, the normalised twist distribution is determined assuming a taper ratio of 1. The optimum total washout is determined with Equation 3.2. The twist distribution is optimised for a lift coefficient of 0.5 and assuming a lift curve slope for the untwisted wing determined with a lifting-line free wake polar yielding $C_{L_{\alpha,\ no-twist}} = 0.117\text{deg}^{-1}$. The resulting washout is 5.44 degrees and its span-wise distribution is shown in Figure 3.3. The initial wing has a span of 10m and a constant chord of 1m yielding a surface area of 10m^2. A higher aspect ratio variant with 15m span and 15m^2 surface are is assumed for the high-lift configurations.

$$\omega(y) = 1 - \frac{\sqrt{1-(2y/b)^2}}{1-(1-\lambda)|2y/b|} \tag{3.1}$$

$$\Omega_{opt} = (2(1+\lambda)/\pi C_{L_{\alpha,\ no-twist}}) C_{L_{des}} \tag{3.2}$$

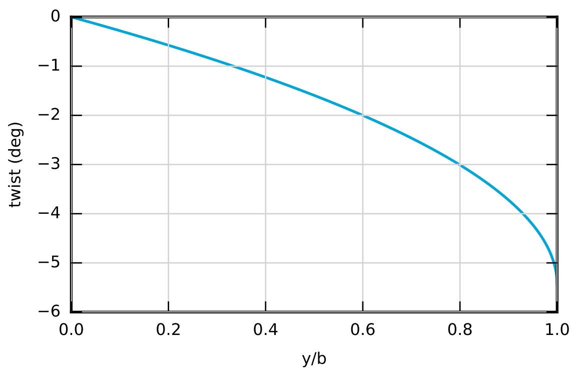

Figure 3.3: Wing optimal twist distribution acc. to Phillips et al. [159] for a rectangular wing with 10m span, 1m chord, flight Mach number $M = 0.3$ and design lift coefficient $C_L = 0.5$ at sea-level conditions

3.4. CONFIGURATIONS

Two general groups of configurations are considered for this project. First, the effect of wing-tip mounted propellers on the overall configuration performance is assessed. In a second phase, the effect of lift-augmenting propellers is analysed.

3.4.1. WING-TIP PROPELLERS

Wing-tip mounted propellers are compared for installation at one radius upstream (tractor) and downstream (pusher) of the wing. Both configurations are shown in Figure 3.4. Both cases are simulated on an untwisted as well as on an ideally-twisted wing. As shown, a line in axial direction and going through the quarter chord point is the reference line on which the propeller is shifted without being displaced in span-wise or vertical direction. The blade azimuth is zero when it points outboard, parallel to the y-axis and goes positive clockwise when seen from upstream. The thrust is balanced with the overall aircraft drag while staying at the same wing lift coefficient. How this is done is explained in the next section.

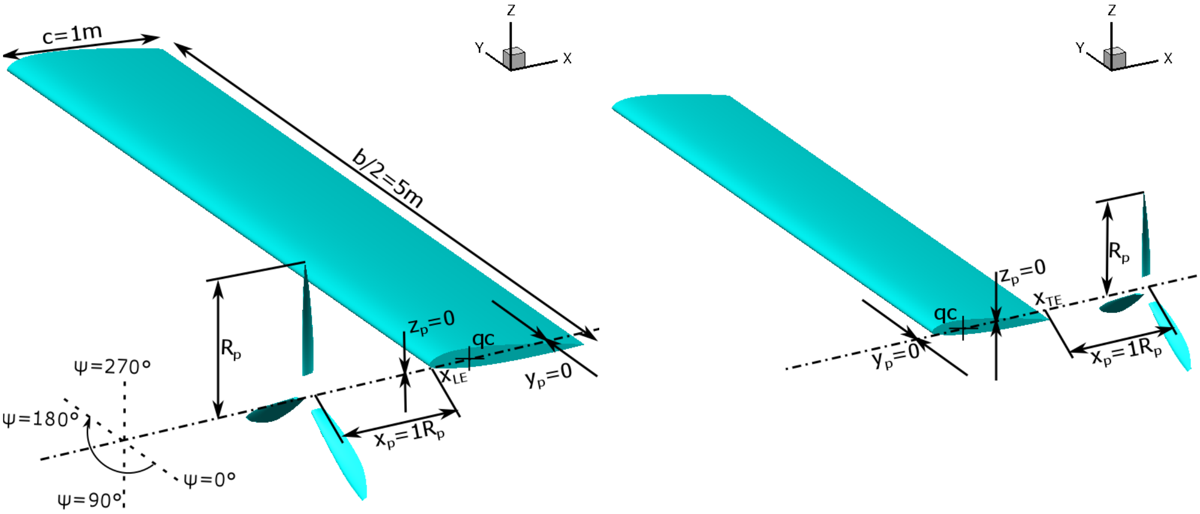

(a) Wing-tip tractor configuration

(b) Wing-tip pusher configuration

Figure 3.4: Wing-tip tractor and pusher propeller configurations selected for numerical simulations

3.4.2. LIFT-AUGMENTING PROPELLERS

The lift-augmenting propellers (see Figure 3.5) are considered at two different locations: in front of the leading-edge and over the wing. The leading-edge mounted propellers are installed one radius in front of the wing with a spacing between the propellers of 10% of the propeller diameter. The over-the-wing propellers are installed 1% chord lengths above the wing surface at an axial position of 20, 40, 60 or 80% of the chord. The diameter of the propellers is determined with Equation 3.3 and assuming the number of propellers, the free fraction of the wing span b_{free} and the spacing between the propellers as fraction of the propeller radius $k_{gap} = dy_{gap}/R_P$.

$$D_p = b_{free}/(N_p \cdot k_{gap}) \tag{3.3}$$

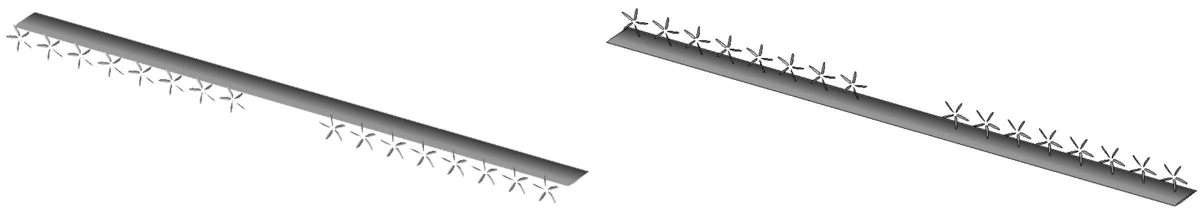

(a) Leading-edge propeller configuration

(b) Over-the-wing propeller configuration

Figure 3.5: High-lift propeller configurations with 16 propellers installed $1R$ in front of the leading edge or at different chord-wise locations above the wing surface (assumed 88% free wing surface and $0.1R$ clearance between the propellers)

3.5. THRUST-DRAG BOOKKEEPING & PERFORMANCE ASSESSMENT

One benefit of the body-force approach is the direct access to net thrust values and the ability to trim it to a target value during the simulation. This allows for a straight forward trim procedure for a thrust-drag balance.

In order to have a fair comparison between a pusher and a tractor configuration for wing-tip mounted propellers, the drag and thrust forces during cruise have to be balanced. This requires the total aircraft drag which is estimated using a fixed drag term for the non-resolved parts of the airframe (fusalage, tail, ...). This term is determined assuming an overall lift-to-drag ratio during cruise. The isolated wing results from CFD are then used to determine the wing fraction of the drag. The remaining fraction of the total drag is taken as fixed additional drag for all other configurations with propellers installed. Assuming $(L/D)_{ac} = 16.8$ and taking $D_{ac-w} = D_{ac} - D_w$ with the results for the isolated wing from Table 5.2 we have that $D_{ac-w} = 924\text{N}$ with the isolated wing results from Chapter 6.

To compare the effect of the different configurations, the relative change in drag, propeller efficiency and power consumption of the propeller-wing combination (com) with respect to the isolated wing and propeller (iso) are compared (see Equations 3.4 to 3.6). It should be kept in mind that this always neglects the influence of a nacelle on the configuration which will have a significant effect on the performance as well.

$$\Delta C_D = C_{D_{com}} - C_{D_{iso}} \tag{3.4}$$

$$\Delta \eta_p = \eta_{p_{com}} - \eta_{p_{iso}} \tag{3.5}$$

$$\Delta P_p = P_{p_{com}} - P_{p_{iso}} \tag{3.6}$$

The lift and drag coefficient of the wing, are defined as the integrated pressure and skin friction on the surface and as such include all possible interaction effects. The propeller efficiency, thrust and power are a result of the interaction with the wing in case of a propeller-wing configuration and as such are the effective installed metrics. The definition of shaft and propeller power as well as the propeller efficiency are given in Equations 3.7 to 3.9.

$$P_{shaft} = 2\pi n Q \tag{3.7}$$

$$P_p = T v_\infty \tag{3.8}$$

$$\eta_p = \frac{P_p}{P_{shaft}} \tag{3.9}$$

4

NUMERICAL SIMULATION SET-UP

"While computational aerodynamics would indicate that engineers have had a capability to analyse such coupling for many years, this is only true with extensive modelling efforts, with each analysis case requiring a week of execution time on a cluster with hundreds of processors. Performing conceptual design and optimization of these DEP configurations requires more rapid analyses that can still capture the interactions with similar trends across the key parameters of interest."

Mark D. Moore et al. (2014) [41]

After the introduction into the thesis contents and introducing the configurations that are of special interest, this chapter contains a description of the simulation tools that are used to study the configurations of interest. This includes a description of the pre-existing tools, their numerical settings, convergence studies, as well as coupling procedures. At first, the lifting line code PUMA is discussed. Subsequently, the RANS solver elsA [160] and its coupling to PUMA for the body-force approach are described. Finally, it is shown how the meshed-propeller URANS simulations have been set up.

4.1. LIFTING LINE CODE

The readily available free-wake lifting-line code PUMA, developed at ONERA, was used for the lifting line simulations. It is the lowest-fidelity tool used in this project and serves mainly as a quick tool to see trends. In the further parts of the report, its performance to capture the interaction effects will be compared to higher fidelity tools. This section gives a general code description, followed by a convergence study and the numerical settings used for the simulations in the subsequent chapters.

4.1.1. CODE DESCRIPTION

PUMA is python based and is embedded in a multi body system (allowing easy implementation of different axes systems, rotating/non-rotating parts, inflow angles, etc.). The free wake can take into account interactions of different wakes (rotor/rotor, rotor/wing, ...) and using multilevel fast multipole method to improve computational time. Furthermore, fixed and free wake computations are possible with each surface having an own optional shedding frequency. The lifting surfaces (propeller blades or wings) are defined in the tool by n 2D airfoil sections (see Figure 4.1a) with corresponding look-up tables for the Mach and Reynolds number dependent aerodynamic forces. These look-up tables were available for the used propeller and wing airfoils and have been created from 2D viscous RANS simulations using the Spalart turbulence model. Large angle-of-attack data is added from experimental NACA23012 data for code robustness during transient simulation phases with extreme inflow angles. For the wing, only one airfoil section is used such that everywhere along the surface, the same airfoil data is applied. For the propellers, six different airfoil look-up tables corresponding to the airfoils in Table 3.2 are used. Additionally, a 3D geometry of the lifting surfaces with m span-wise locations with corresponding chord, twist, sweep and dihedral values are required. Corrections are available for Mach number and sweep angle. Code is validated with CFD results for the configurations studied in this project. Individual wake models are created for each lifting surface which all take into account the induced velocities by the other wakes and all act on each lifting surface. Figure 4.1b shows this for 16 propellers in front of a wing. The blue propeller wakes and the green wing wake interact strongly and deform moving downstream.

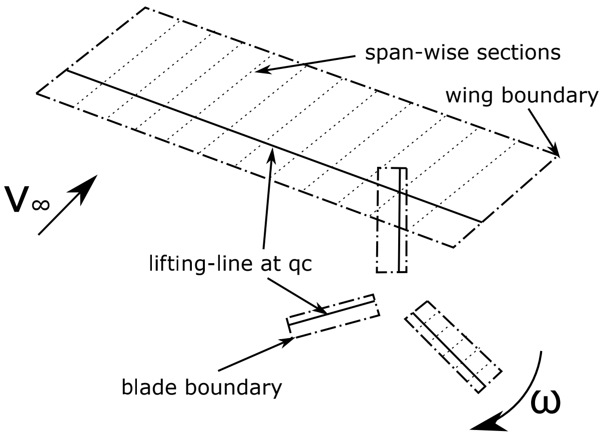

(a) Lifting-line model for a wing-tip mounted propeller showing the discretisation of the lifting surfaces into span-wise sections on the quarter-chord line

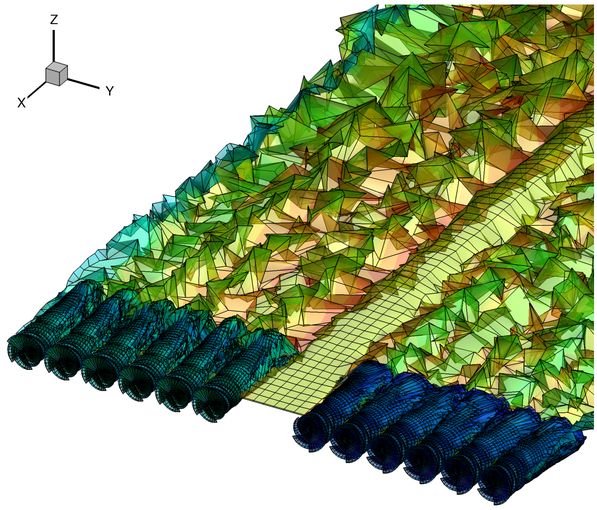

(b) Resulting free wake model for 16 leading-edge mounted propellers in front of a wing with clear wing-wake deformation

Figure 4.1: Exemplary lifting-line model of a wing-tip mounted propeller and the resulting free wake structure of the converged solution for 16 leading-edge mounted propellers

Another capability of the code is to trim a parameter to a target value by manipulating a prescribed variable. This was used to achieve constant lift and thrust values for different configurations for better comparability. Further capabilities are Mach correction and the handling of singularities such that no big convergence issues occurred during the simulations.

The wing model of the lifting-line code determines the lift, drag, moment, effective angle-of-attack, velocity vector, Mach number and further information at each span-wise section and also provides the global load coefficients as resulting from the integrated sectional values. The results contain viscous effects included in the look-up tables for the airfoil sections but otherwise do not take into account any 3D-viscous, thickness or span-wise flow effects. The propeller model provides, next to the sectional lift, drag, effective angle-of-attack, velocity vector, Mach number etc. at each blade section also the thrust, torque, power, efficiency, pitch, in-plane loads and other performance metrics of the propeller. These global metrics are again integrated values from the sectional blade information. As for the wing, these results cover 2D section viscous effects into account but else neglect 3D-viscous effects. Additionally, no thickness or radial-flow effects.

4.1.2. CONVERGENCE STUDY & NUMERICAL SETTINGS

As can be seen in the following several span-lengths with shedding frequency corresponding to a distance between to wakes of a fraction of a span-length have to be travelled for a wing to have converged lift and drag values. Also, it is known from experience that multiple propeller rotations are required with a certain wake shedding frequency to have converged propeller performance. For small propellers with high rotational speeds and high-aspect ratio wings this leads to a high computational cost. It is therefore important to assess the convergence of the results for different numerical parameters. Figure 4.2 shows the convergence for propeller rotation size, propeller sections, wing translation step size and wing sections for a non-twisted rectangular wing with aspect ratio 10 and 12 propellers installed one radius in front of the leading edge.

As a compromise between accuracy and computational costs, the wing-tip propeller cases were analysed with a rotation step size of 6 degrees, 16 propeller section, a wing translation step of 0.1 spans and 50 wing sections. These settings were too demanding for cases with multiple high-lift propellers such that for these cases the settings were alleviated. The propeller rotation step size is increased to 10 degrees, the propeller sections are reduced to 12 sections, the wing translation step size and number of wing sections remained as before. The simulation was performed for 24 spans travelled such that the solver reached convergence. The resulting parameters of interest (e.g. lift, drag, thrust, propeller efficiency, ...) were determined taking the mean value over the last propeller rotation or the last period in case of an otherwise fluctuating solution due to the aerodynamic interactions (e.g. due to the periodic passing of the slipstream wake panels by the wing).

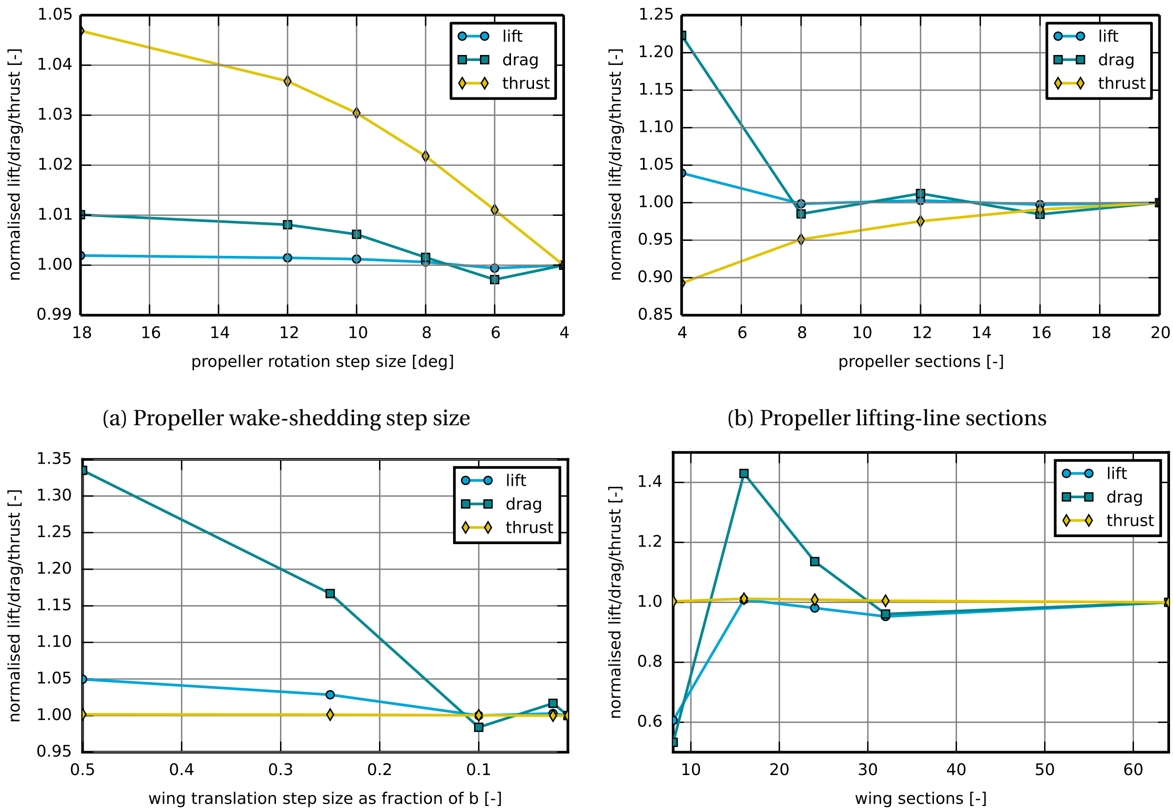

(a) Propeller wake-shedding step size

(b) Propeller lifting-line sections

(c) Wing wake-shedding step size

(d) Wing lifting-line sections

Figure 4.2: Lifting line convergence study for propeller and wing lifting-line and wake discretisation

4.2. RANS-LIFTING LINE COUPLING WITH BODY FORCES

The body-force approach for the coupled lifting line-RANS simulations is the intermediate-fidelity tool in this project. Since it is a rather new way to simulate the effects of propellers for propeller-wing configurations, it was necessary to explore the required discretisation and numerical set-up parameters to achieve converged solutions. Additionally, one goal of the thesis is to show what effects are captured by this approach and where it fails to predict the real flow physics. For the RANS computations, the solver elsA [160] developed by Onera, Airbus and Safran is employed. The propeller is modelled with the previously described PUMA code. This section starts with a general description of elsA. Afterwards, the numerical RANS settings are given. Additionally, a description of the mesh including a convergence study is presented. The coupling procedure between the two codes is explained subsequently. Finally, convergence criteria for the simulations are given. A minimum working example of the coupling procedure was already implemented for a single propeller and a wing at the beginning of the thesis work.

4.2.1. ELSA RANS SOLVER

The RANS solver that was used for the meshed propeller URANS simulations as well as for the coupled body-force method is elsA. This solver is a cell-centred structured CFD code. The user interface is python based allowing flexible implementation of the coupling procedure.

4.2.2. NUMERICAL RANS SETTINGS

The numerical RANS settings in elsA are set as follows. The Jameson scheme is selected for the spatial discretisation. The artificial dissipation parameters at convergence are χ_2=0.5 and χ_4=0.008 (with initial χ_4=0.064 for faster & stable convergence). A backward Euler scheme with Gear sub-iterations is applied for the temporal discretisation. The time step is set to two degrees propeller rotation angle with 20 sub-iterations. The Kok k-ω turbulence model is used to close the RANS equations. A shear stress transport (SST) correction as well as a Zheng limiter is applied. The turbulence intensity factor is set to 0.0005 and the viscosity ratio is equal to 0.1. The Courant-Friedrichs-lewy value is set to 10 in case of steady simulations.

Parallel computing was employed during the computations. The blocks were optimally distributed over processors until no further time-saving could be achieved by increasing the number of processors. The computations were first carried out on ONERA's Stelvio machine featuring 8000 Intel Xenon cores (2.5-3.06GHz) distributed over 704 computing nodes, 35 Tbytes of memory, and shared disk space of 300 Tbytes. Later, the new Sator facility featuring 17,360 Intel Xenon processors (14 cores with 2.5GHz), 77.5 Tbytes of memory and 1,000 Tbytes of shared disk space was used [1]. Typically, the optimum number of processors lay between 40 and 60.

4.2.3. GRID

A structured mesh was used to discretise the domain. A overset grid was constructed consisting of a wing grid, a cartesian background grid, and a propeller background grid for each propeller. In case of a meshed propeller, additional blade grids were added using the propeller background grid as a buffer grid. With this approach, the wing grid is identical for all configurations and easy configuration manipulations are possible. The overset is realised with a 2-cell interpolation depth to transfer the flow information from one partial grid to the other. In case of occurrence (only for very close wing-propeller coupling in the order of millimetres), orphan points are averaged from the neighbouring cells.

For the wing, an O-grid was generated with Pointwise[2] featuring a first cell hight designed for a y+ value of 0.5. As shown in Figure A.12, the first boundary layer mesh height is indeed large enough with a y+ value ranging between 0 and 1 for the converged solution. A convergence study for the wing grid was done and the results are presented in Table 4.1. The intermediate refinement was used for the simulations in the remainder of the document. While there is still a slight variation of the resultant forces, a further refinement and its associated computational cost is not justified. The aim is to see the interaction effects between propellers and wings and no detailed design study of a specific configuration.

Table 4.1: Wing grid convergence comparing resultant forces and mesh sizes for three different mesh refinements but similar first cell height

	coarse	**intermediate**	**fine**
$n_{nodes,span-wise}$ [-]	101	141	251
$n_{nodes,chord-wise}$ [-]	101	141	251
$n_{nodes,radial}$ [-]	51	61	81
$n_{nodes,wing}$ [-]	$1.3 \cdot 10^6$	$3.2 \cdot 10^6$	$11.6 \cdot 10^6$
$n_{nodes,chimera}$ [-]	$13.4 \cdot 10^6$	$14.2 \cdot 10^6$	$24.3 \cdot 10^6$
C_L [-]	0.6016	0.6055	0.6057
C_D [-]	0.02141	0.02133	0.02139
L/D [-]	28.10	28.39	28.32

[1] ONERA: Supercomputing facilities. URL: http://www.onera.fr/en/supercomputing-facilities, online, accessed July 28, 2017
[2] Pointwise: The Choice for CFD Meshing. URL: http://www.pointwise.com/, online, accessed July 28, 2017.

The propeller grids are cylindrical blocks with a diameter of the propeller and a thickness to accommodate chord and sweep of the propeller. Additionally, transitional blocks at the inlet, the outlet and the outer radial surface are added for a smooth increase in cell size to the cartesian background grid. The grids are generated analytically using the XTree and Cassiopee toolboxes [161]. The body force grids have undergone a convergence study (see Appendix A.1.2 for flow field comparisons).

The cartesian background grid consists of blocks with varying densities to closely match cell sizes of neighbouring blocks. It is generated automatically using the Cassiopee toolbox. For details and illustrations of the assembled and individual grids see Chapter A.

The boundary conditions have been selected as follows. A farfield boundary condition (conservative variables density, x-y-z momentum, and energy stagnation density prescribed) is applied on the cartesian background grid surfaces. Only its symmetry plane is subject to a symmetry boundary condition. The wing grid, blade grids, and propeller grids have overlap boundary conditions on their outer boundaries. The wing and blade grids additionally have a viscous wall boundary condition at the inner boundaries, modelling an adiabatic wall with no-slip condition.

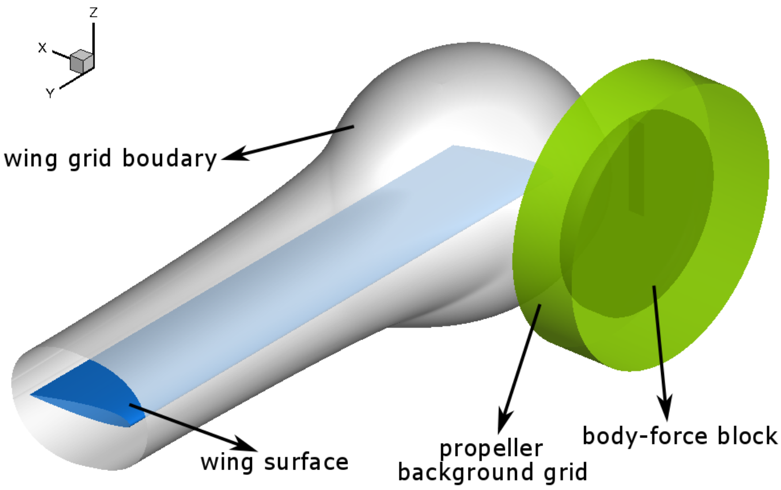

Figure 4.3: Chimera grid blocking strategy showing body of the wing (blue) as well as the block boundaries of the body-force domain (dark green) and the propeller background (light green)

4.2.4. COUPLING PROCEDURE

The coupling procedure is shown in form of a flowchart in Figure 4.4. First, the RANS simulation is initiated. Then, the flow field is extracted from the flow solution in the body force grid (initially being the free stream velocity field). The lifting-line code is executed in this flowfield without calculating induced velocities as they are already included in the flow solution. If the number of iterations is larger than the selected threshold x_1 the pitch of the propeller is trimmed to achieve the objective thrust (or alternatively objective power). The propeller is rotated in selected azimuthal steps and the propeller forces over one full rotation are extracted, giving a disc with propeller forces. These forces are distributed in axial direction by means of a Weibull density function whose coefficients are calibrated with an isolated simulation as function of radial position. The force field is now projected onto the body-force grid and included in the RANS iteration as source terms in the momentum equation. Every x_2th iteration, the source terms are updated by the lifting line code with the current flow field until the simulation is converged.

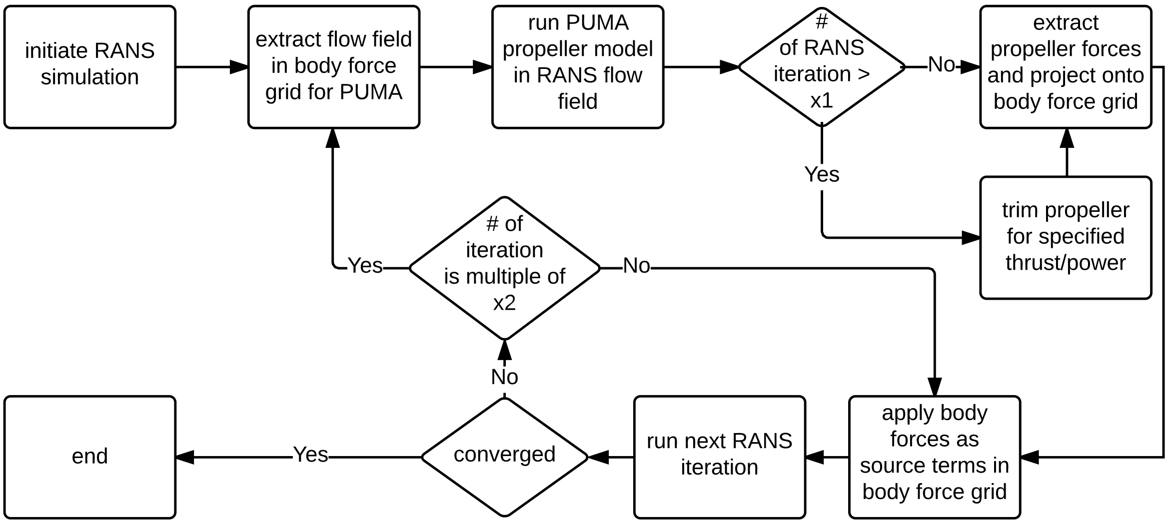

Figure 4.4: Body-force approach coupling procedure flowchart

TRANSFERRING THE FLOWFIELD TO THE LIFTING LINE CODE

To transfer the RANS flowfield to the lifting line code, only the velocity vectors inside the propeller background grid are extracted from the flow solution. The lifting line code PUMA has a pre-existing feature to impose a a three dimensional flowfield instead of having a homogeneous free stream. This is done with the extracted RANS flowfield. Finally, the lifting line code is solved analytically without calculating induced velocities or requiring an iterative procedure. This is computationally very efficient and necessary because the induced velocities are already included in the RANS flowfield. As will be seen later, this requires the induced velocities in the RANS solution to be accurately estimated at the lifting line position to have a good representation of the propeller performance.

TRANSFERRING PROPELLER LOADS TO BODY FORCES

After the lifting-line code has evaluated the blade loads, these have to be transformed into source terms that can be prescribed on the body-force mesh. The flow solver requires as input the momentum and energy source terms per unit volume at each cell centre. For this purpose, the blade loads at all azimuthal and radial positions are retrieved. These loads are then projected from the blade reference frame onto the RANS axis system.

$$\frac{dF_x}{dr} = \frac{dF_a}{dr} \tag{4.1}$$

$$\frac{dF_y}{dr} = \frac{dF_t}{dr} \cdot sin(\Psi) \tag{4.2}$$

$$\frac{dF_z}{dr} = \frac{dF_t}{dr} \cdot cos(\Psi) \tag{4.3}$$

The sectional loads per unit length for each radius are then divided by the arc length of the circle (Equations 4.4 to 4.6) to arrive at the loads per area at sectional loads for each area element of the disc swept by the lifting lines. The energy added is simply the torque times rotational speed as defined in Equations 4.7 and 4.8.

$$\frac{dF_x}{dA} = \frac{dF_x}{dr} \cdot \frac{N_{blades}}{2\pi r} \tag{4.4}$$

$$\frac{dF_y}{dA} = \frac{dF_y}{dr} \cdot \frac{N_{blades}}{2\pi r} \tag{4.5}$$

$$\frac{dF_z}{dA} = \frac{dF_z}{dr} \cdot \frac{N_{blades}}{2\pi r} \tag{4.6}$$

$$\frac{dQ}{dA} = \frac{dF_{tan,blade}}{dr} \cdot r \tag{4.7}$$

$$\frac{dE}{dA} = \frac{dQ}{dr} \cdot n \tag{4.8}$$

Distributing the source terms (currently on a disc at the quarter chord position) in a three-dimensional space requires the distribution of the lifting-line point loads at the quarter-chord line over the chord-wise dimension of the blade. For this, a generic approach was chosen that assumes a generic axial distribution (not chord-wise) by making use of a probability density function with the required characteristics of having an integral of one, having a typical axial blade load distribution shape, and being adjustable to allow calibration. This calibration is an essential part of the method as the induced velocities at the quarter-chord line have to be realistic. Only by matching the induced velocities at this location, the lifting-line code will observe realistic inflow conditions. If all the source terms were applied at the propeller leading edge, the induced velocities would be too high. On the other hand, an even distribution would result in underestimated induced velocities. By modelling a physical distribution, the right induced velocities can be approached.

The chosen Weibull function is defined as shown in Equation 4.13 with its corresponding cumulative distribution function (Equation 4.14) having a value of one for $x = 1$ [162]. Hence, the source terms per unit area are divided by the local chord length and multiplied with the local weight of the Weibull function (Equations 4.9 to 4.12) to arrive at the body-force terms per unit volume.

$$\frac{dF_x}{dV} = \frac{dF_{x,blade}}{dA} \cdot \frac{W_{Weibull}}{c} \tag{4.9}$$

$$\frac{dF_y}{dV} = \frac{dF_{y,blade}}{dA} \cdot \frac{W_{Weibull}}{c} \tag{4.10}$$

$$\frac{dF_z}{dV} = \frac{dF_{z,blade}}{dA} \cdot \frac{W_{Weibull}}{c} \tag{4.11}$$

$$\frac{dE}{dV} = \frac{dE}{dA} \cdot \frac{W_{Weibull}}{c} \tag{4.12}$$

As the distribution shall start and end at zero, the location parameter ξ_0 is set to zero. Furthermore, the shape parameter is set to $c = 2$ to obtain a typical chord-wise blade loading shape. By calibration with isolated propeller body-force and pure lifting-line simulations the scale parameter was found to be $\alpha = 0.35 - 0.27\frac{r}{R}$ depending on the radial position. The resulting chord-wise load distribution is shown in Figure 4.5. The calibration was performed such that the induced velocities close to the blade were as close as possible. The calibration was only performed once for the project for the wing-tip mounted propeller at a thrust setting of 1800N.

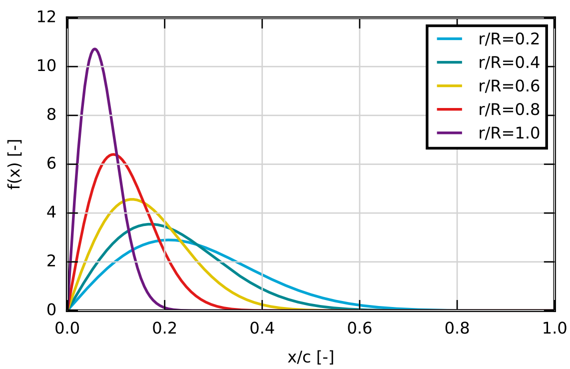

Figure 4.5: Weibull function for the axial load distribution at different radial blade positions as calibrated for the minimum induces loss propeller at design conditions

$$f(x) = \frac{c}{\alpha}\left(\frac{x-\xi_0}{\alpha}\right)^{c-1} e^{-\left(\frac{x-\xi_0}{\alpha}\right)^c} \tag{4.13}$$

$$F(x) = 1 - e^{-\left(\frac{x-\xi_0}{\alpha}\right)^c} \tag{4.14}$$

The resulting loading of the blade is shown in Figure 4.6. The image shows a slice of the body-force mesh at constant azimuth with an indication of the local loading of the blade by presenting the prescribed body-forces. The leading edge is pointing downwards. It can bee seen how the load is only applied to the mesh cells inside the swept blade volume.

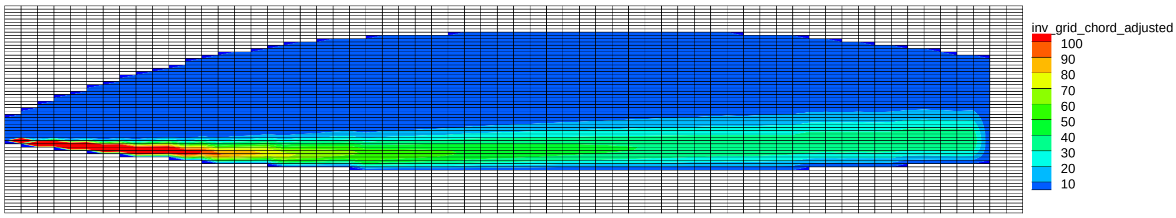

Figure 4.6: Chord-wise blade load distribution on body force mesh showing the source term strength for each mesh cell on an axial cut of the body-force block (leading-edge pointing downwards and free stream coming from below)

This approach is beneficial in that it is very generic and can be used without detailed knowledge of the actual chord-wise loading of the blades. The knowledge of the slipstream induced velocity profiles is enough information. As will become more clear in the following chapters, however, the calibration of this method needs to be redone if a significant change in propeller operating conditions occur and requires reference data. A different approach could be the use of known pressure distributions of the used airfoils. This however, requires the availability of this information and neglects radial flow effects. Another benefit of the selected model is that it can easily be used on a structured cylindrical grid since it works with an axial distribution. If instead, a chord-wise distribution is used the projection of the forces of twisted blade onto such a grid requires more attention.

NUMERICAL LIFTING LINE SETTINGS

Next to the coupling procedure itself, also the numerical settings specific to the lifting-line code have to be specified. As explained previously, PUMA is executed demanding no calculation of induced velocities. In other words, the lifting-line model of the propeller is used to analytically determine the, local inflow angles, local blade angles of attack and the resulting local load coefficients. These are already included in the extracted RANS flowfield that is imposed on the computation. For this reason, little computational effort is required for each time step. This allows to select a small time step without large penalty. The rotation step size is hence set to 2 degrees propeller rotation (as for the meshed propeller URANS simulations). For the high-lift propeller cases, the rotation step was increased to 6 degrees to reduce memory requirements and computation time. Each propeller blade is discretised into 37 span-wise sections.

For the propellers, the geometry (radial stations, chord, twist, dihedral, and sweep), airfoil polars, rotational speed and a pitch angle at 75% blade span are specified. Additionally, a trimming procedure implemented in PUMA is activated after a selected number of RANS iterations of 200. This option is used to either specify the shaft power or thrust of each individual propeller. The code is forced to change the pitch angle at constant rotational speed to meet the target power/thrust. Thrust and power are a direct result of the PUMA model and are based on the integrated loads on the blade.

4.2.5. CONVERGENCE & GLOBAL FORCES

In case of non-meshed propellers, the global forces acting on the wing surface are evaluated as average over the last 100 iterations. Otherwise, the forces are computed as average over the last period of the solution oscillations (e.g. 360/3=120 degrees in case of three propeller blades). The wing loads are determined by extracting the surface pressures and skin friction and integrating those over the surface to obtain the overall loads. The load coefficients are then determined with the reference free stream dynamic pressure and density. The same holds for the propeller, in case of meshed propeller URANS computations. The surfaces pressures and skin friction are integrated to obtain the loads on the blades which are then transformed into thrust, in-plane loads and torque. The shaft power equals $P_{shaft} = 2\pi n q$ while the propeller power equals $P_p = T v_\infty$.

At convergence, the wing lift and drag standard deviation is typically less than 0.1% over the last 1000 iterations. The flow solution residual drops more than four orders of magnitude. Figure 4.7 shows representative convergence histories for body-force simulations as well as for meshed propeller URANS simulations (example is a tractor wing-tip propeller with untwisted wing).

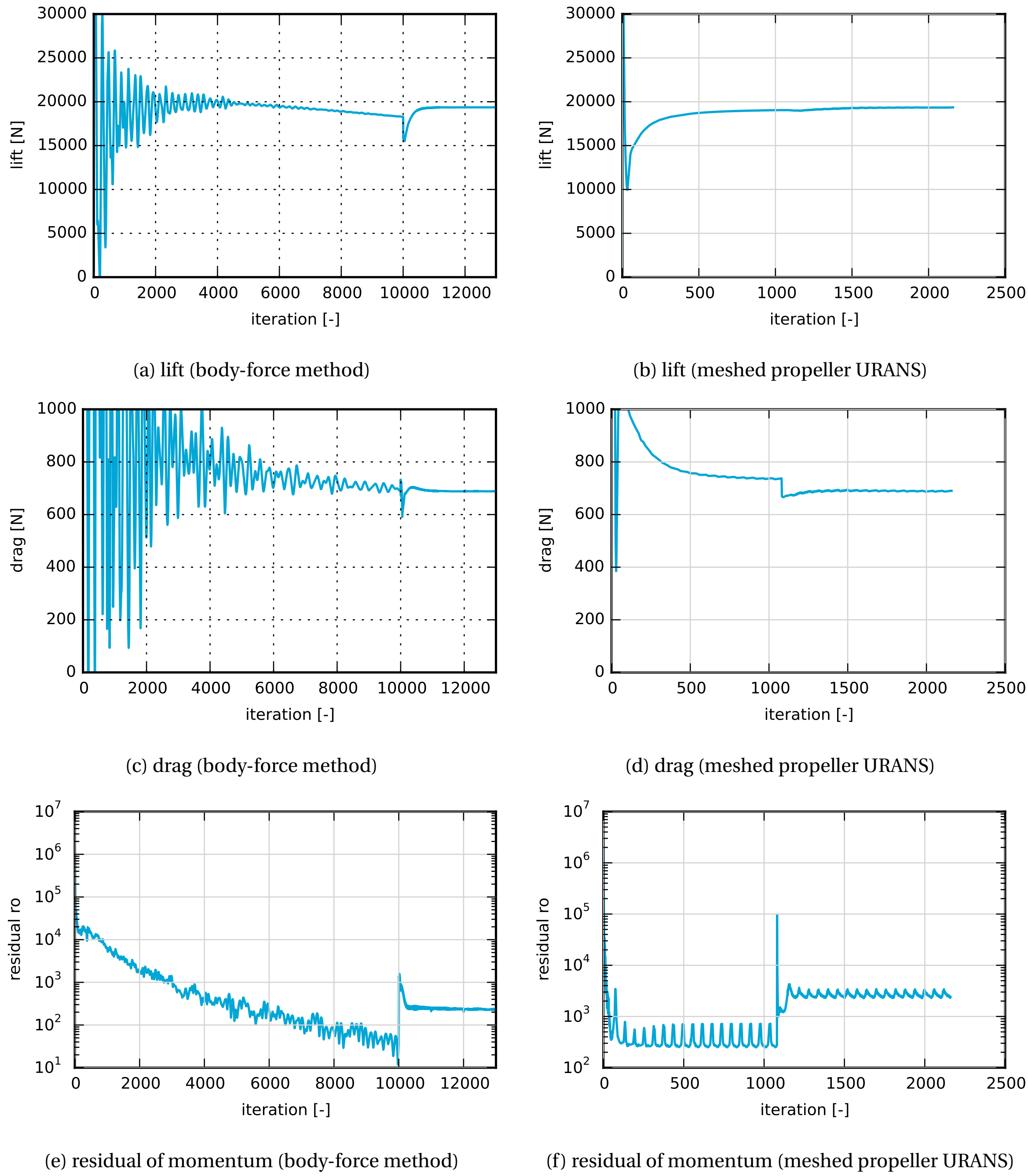

(a) lift (body-force method)

(b) lift (meshed propeller URANS)

(c) drag (body-force method)

(d) drag (meshed propeller URANS)

(e) residual of momentum (body-force method)

(f) residual of momentum (meshed propeller URANS)

Figure 4.7: Exemplary convergence history of resultant wing forces and momentum residual for body-force and meshed propeller URANS simulations (results shown for non-twisted wing with tractor tip propeller)

Clearly, the switch from steady to unsteady mode and the change in artificial dissipation coefficient can be observed at 10,000 iterations for the body-force method. The change in artificial dissipation is also observable in the meshed propeller URANS case. (Change to unsteady for body-force approach initially necessary because of non-physical separations. These occured due to a very high and non-realistic viscosity ratio in the numerical RANS settings such that separation is promoted by over-predicted viscosity. Later not necessary any more but kept for consistency of results.)

4.3. URANS SIMULATIONS WITH MESHED PROPELLERS

As a final simulation strategy, URANS simulations with meshed propellers are employed. This higher fidelity approach is used in two ways. On the one hand, this proven method provides reliable estimations for reference cases that are used for validating the body-force approach. On the other hand, the unsteady resolved propeller slipstream flow features provide additionally information on the principles behind distributed propulsion aerodynamics.

The simulations are set-up in the same way as for the body-force approach. The grid is identical, but propeller blade grids are added inside the cylindrical propeller background grid which now acts as a buffer grid between blades and cartesian background. The numerical settings are identical to those of an unsteady body-force simulation.

The mesh for each propeller blade consists of 2.1M cells. For the three bladed propeller, this means an additional 6.3M cells per propeller with respect to the body-force grid. This may be acceptable for a single propeller, but results in significantly more computational costs when analysing a wing with multiple lift augmenting propellers.

The propeller mesh was provided by ONERA and cannot be shown in detail because of the non-disclosed airfoil sections. An image of the grid can be found in Appendix A. It was meshed according to the experience of the experts in the team.

5

Validation of the Body Force Approach

The body force approach has been set up because it allows less expensive (regarding computational costs and time spent on pre- and post-processing) simulations without loosing significant amounts of accuracy and information with respect to fully meshed propeller URANS analyses. To proof that this is indeed the case for the propeller-wing configurations of interest, several validation cases are presented in this chapter. First, Section 5.1 shows comparisons between meshed propeller URANS and body-force approach simulations for different configurations. These range from isolated propellers, over singe wing-tip mounted propellers to multiple propellers distributed along the leading edge of a wing. In a second step (see Section 5.2), the body-force method was applied to a wind-tunnel set-up and the results between numerical and experimental simulations are presented.

5.1. Comparison between the Simulation Strategies

A comparison between the previously described simulation strategies on the same configurations is presented in the following sections. This is done in order to gain increased confidence in the individual tools' ability to model the configurations of interest as well as to identify their limits. Firstly, an isolated propeller is investigated. Secondly, a wing-tip propeller configuration is used. Thirdly, three distributed propellers along the wing leading edge are analysed.

5.1.1. Isolated Propeller

As a first step, the three simulation methods are compared for the described minimum induced loss propeller with a radius of 0.8m. The thrust coefficient is set to $C_T = T/(\rho \cdot n^2 \cdot D^4) = 0.1238$ at a tip Mach number of 0.5 and a free-stream Mach number of 0.3 at sea-level conditions, yielding an advance ratio of 1.88. The resulting propeller performance is shown in Table 5.1. The propeller efficiency varies within 3.1% .

Table 5.1: Isolated propeller performance results as obtained with URANS, body-force and lifting-line simulations

	URANS	**Body-Force**	**Lifting-Line**
T [N]	1150	1148	1148
$\beta_{0.75R}$ [deg]	43.11	41.93	42.74
η_p [-]	0.882	0.913	0.904
P_{shaft} [kW]	266.2	256.9	259.2

To compare the propeller influence on the flow, the axial and tangential induced velocities are presented in Figure 5.1. For three different axial positions (0.2c upstream & 1c and 2c downstream of the propeller disk), the mean induced velocity profiles are compared for the three different methods. The axial velocity increments are very similar for the downstream locations. Only the pure lifting-line simulation over-predicts the induced velocity near the blade root. As a general consequence, the increased dynamic pressure due to a propeller, should be well captured by a proceeding wing. Directly upstream of the blade, however, the body force method over-predicts the velocity at the highest loaded sections (around r/R=0.75).

The tangential induced velocities match very well for the URANS and body-force simulations. PUMA over-predicts the induced tangential velocities upstream and under-predicts them downstream of the propeller plane. These discrepancies were not observed in other analyses (see for example the body-force grid convergence study in Section A.1.2) and is believed to be erroneous in the Figure 5.1. This statement is supported by the close power prediction as reported in Table 5.1 which does not fit to such large velocity discrepancies.

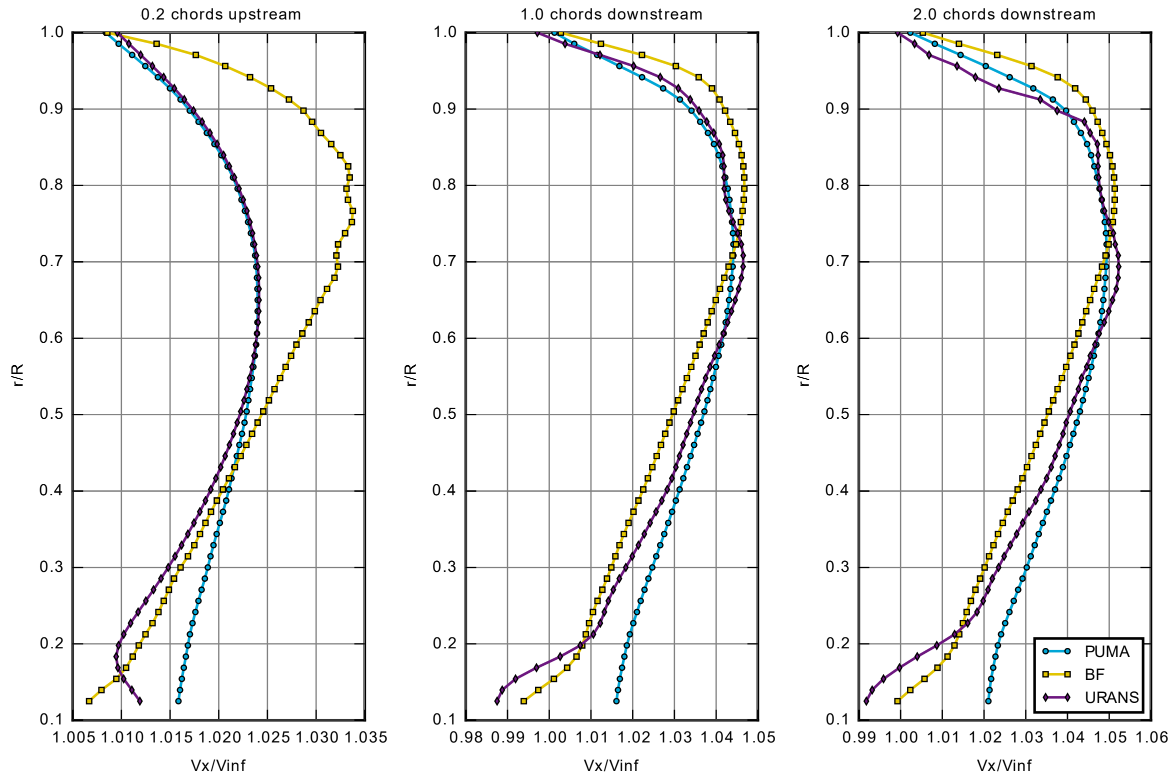

(a) axial induced velocity profiles

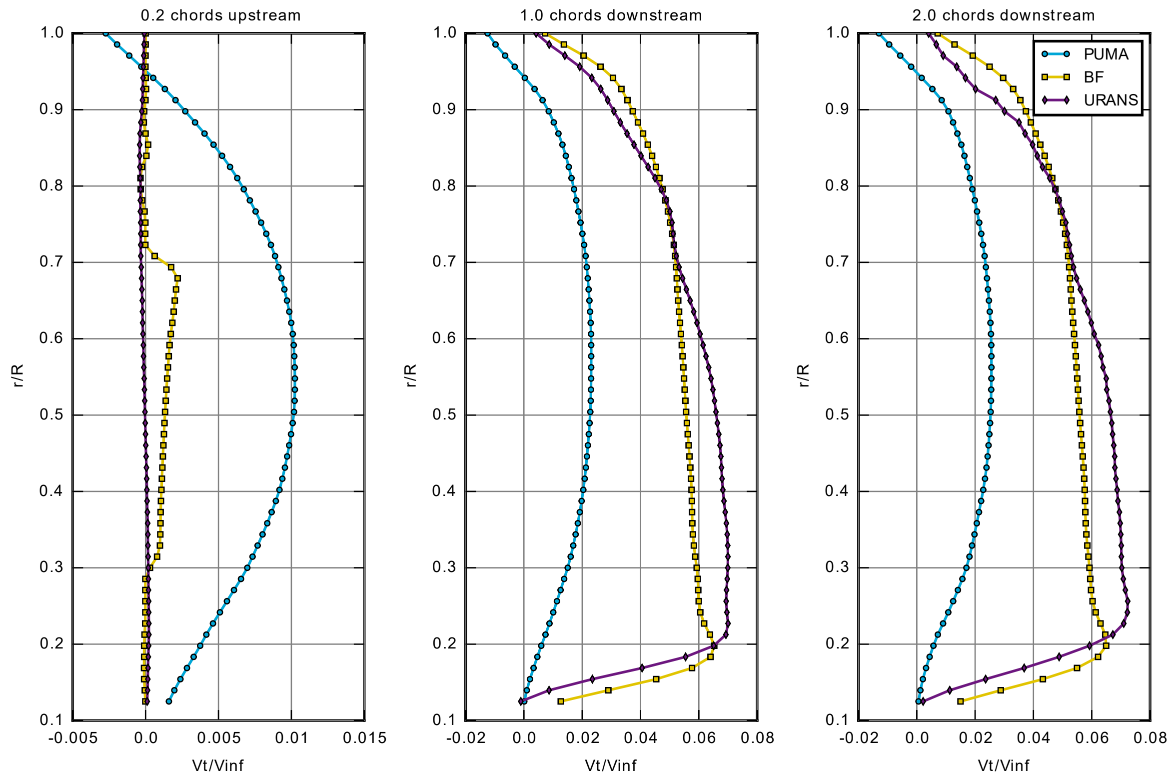

(b) tangential induced velocity profiles (PUMA results erroneous)

Figure 5.1: Mean induced velocity profiles of the isolated propeller compared for URANS, body-force and lifting-line simulations ($T = 1148$N, tangential velocities for PUMA erroneous)

5.1.2. WING-TIP PROPELLER

The results for a wing-tip mounted propeller are presented in the following. A pusher propeller (Table 5.4) and a tractor propeller (Table 5.5) having an axial distance to the wing tip of one propeller radius as well as the isolated wing and propeller geometries (Tables 5.2 and 5.3) are assessed. Results for all cases are obtained with the lifting-line code PUMA, the meshed propeller URANS approach, as well as with the coupled body-force method.

Since the grid as well as the numerical settings for the URANS and body-force simulations are identical if no propeller is introduced the results for the isolated wing are identical. The lifting-line code underestimates the drag by 7.0% with respect to the URANS simulation leading to a lift-to-drag ratio of 30.6 instead of 28.3. The propeller thrust is trimmed to match the drag of the whole configuration including the fixed 924N accounting for the non-resolved parts. The propeller performance differs for all three cases since all methods model the propeller by different means. The URANS and body-force propellers are trimmed to the same thrust such that a direct performance comparison can be made. The body-force model seems to underestimate the propellers' required power by 3.5%.

Table 5.2: Isolated untwisted wing performance results obtained with URANS, body-force and lifting-line simulations

	URANS	Body-Force	Lifting-Line
C_L [-]	0.606	0.606	0.609
α [deg]	5.5	5.5	5.25
C_{D_w} [-]	0.0214	0.0214	0.0199
$(L/D)_w$ [-]	28.3	28.3	30.6
D [N]	2296	2296	2394

Table 5.3: Isolated propeller performance results obtained with URANS, body-force and lifting-line simulations

	URANS	Body-Force	Lifting-Line
T [N]	2301	2296	2394
$\beta_{0.75R}$ [deg]	43.11	41.93	43.31
η_p [-]	0.882	0.913	0.877
P_{shaft} [kW]	266.2	256.9	278.6
F_y/T [%]	0.0	0.0	0.0
F_z/T [%]	0.0	0.0	0.0

In the pusher propeller case, as shown in Table 5.4, the capability of the different methods to account for the interaction between closely coupled propellers and wings can be assessed. The performance changes with respect to the isolated geometries are always taken with respect to the results obtained with the same method.

Table 5.4: Results for untwisted wing with tip-mounted pusher propeller obtained with URANS, body-force and lifting-line simulations. Differences taken with respect to isolated wing & propeller (SL+0, $Ma = 0.3$, $T = D_{ac}$, $D_{ac-w} = 924$N)

	URANS	Body-Force	Lifting-Line
C_L [-]	0.606	0.606	0.609
α [deg]	5.5	5.5	5.23
C_{D_w} [-]	0.0216	0.0216	0.197
$(L/D)_w$ [-]	27.9	28.1	30.9
D [N]	2301	2302	2184
T [N]	2312	2302	2300
$\beta_{0.75R}$ [deg]	40.06	39.16	39.74
η_p [-]	0.970	1.000	0.970
P_{shaft} [kW]	243.4	235.1	242.1
F_y/T [%]	-1.84	-1.36	-1.15
F_z/T [%]	4.71	5.71	1.70
ΔC_{D_w} [%]	+0.9	+0.9	-1.0
$\Delta\eta_p$ [%]	+8.8	+8.7	+9.3
ΔP_{shaft} [%]	-8.6	-8.5	-13.1

The reference URANS simulation shows a wing drag increase of 0.9% and a propeller efficiency gain of 8.8% resulting in an overall power saving for the thrust-drag balanced system of 8.6%. The body-approach yields very comparable results only differing in propulsive efficiency by -0.1% and in power saving of also -0.1%. The lifting-line code was trimmed to the same thrust as the other two simulations, knowing that its drag is under-predicted, and trying to make a fair comparison for the propeller performance. The result is a comparable gain in propulsive efficiency being 0.6% higher than the URANS solution but also a decrease in wing drag of 1% which is the opposite predicted by the two RANS-based methods. This can be explained by the non-physical induced axial velocity by the free-wake simulation, increasing the dynamic pressure over the wing-tip portion. As a result the power saving is much larger and amounts to 13.1%.

Finally, the tractor configuration (see Table 5.5) can be analysed. As for the pusher case, the URANS and body-force method results match well. The drag reduction is equally large (9.8%) and the propulsive efficiency change differs by 0.3%. The overall power consumption estimated by the body force simulation is 6.9%, comparing well to the 7.0% of the URANS reference case. The lifting-line code is able to obtain the same trends with predicting a drag reduction of 8.5%, a propulsive efficiency gain of 1.6% and a power reduction of 11.6%. However, the wing drag reduction is underestimated while the propulsive efficiency increase is overestimated. This indicates that the lifting-line code predicts a too high stagnation at the propeller location and that the resulting lower pitch requirement for the trimmed thrust leads to a weaker slipstream swirl and dynamic pressure having a lower effect on the wing drag.

Table 5.5: Results for untwisted wing with tip-mounted tractor propeller obtained with URANS, body-force and lifting-line simulations. Differences taken with respect to isolated wing & propeller (SL+0, $M = 0.3$, $T = D_{ac}$, $D_{ac-w} = 924$N)

	URANS	**Body-Force**	**Lifting-Line**
C_L [-]	0.606	0.608	0.609
α [deg]	5.25	5.25	4.95
C_{D_w} [-]	0.0193	0.0193	0.0182
$(L/D)_w$ [-]	31.5	31.6	33.5
D [N]	2155	2153	2083
T [N]	2159	2152	2152
$\beta_{0.75R}$ [deg]	42.48	41.40	41.96
η_p [-]	0.891	0.919	0.891
P_{shaft} [kW]	247.6	239.1	246.4
F_y/T [%]	3.76	3.51	2.50
F_z/T [%]	-3.13	-3.86	-4.40
ΔC_{D_w} [%]	-9.8	-9.8	-8.5
$\Delta\eta_p$ [%]	+0.9	+0.6	+1.6
ΔP_{shaft} [%]	-7.0	-6.9	-11.6

Figures 5.2a to 5.2 show iso-surfaces of the axial vorticity with contours of the axial velocity component as obtained with the meshed propeller URANS simulations. The isolated wing, as well as the pusher and tractor configurations are presented. Next to the tip vortices, also root vortices can be observed due to the missing spinner. It can also be seen, that these vortices are stronger in the tractor case where the propeller operates at a higher pitch setting. The overset grid interpolation seems to generate traces of vorticity at the interpolation regions.

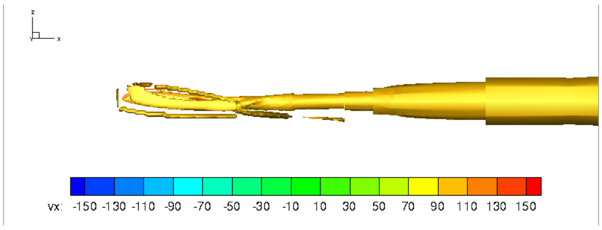

(a) Isolated wing (side view)

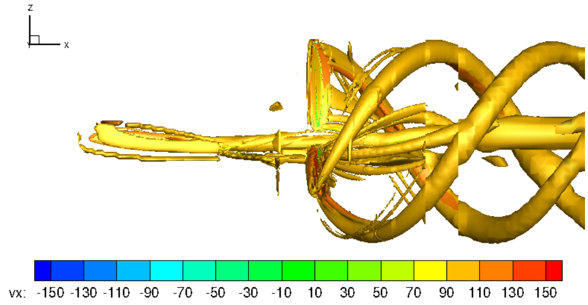

(b) Pusher (side view)

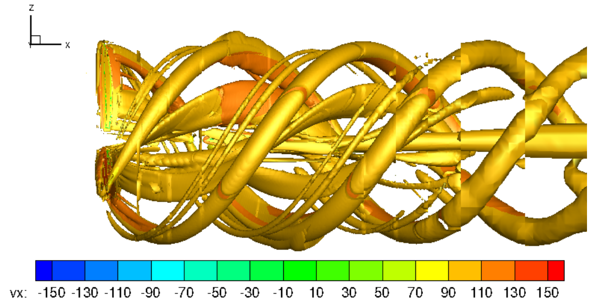

(c) Tractor (side view)

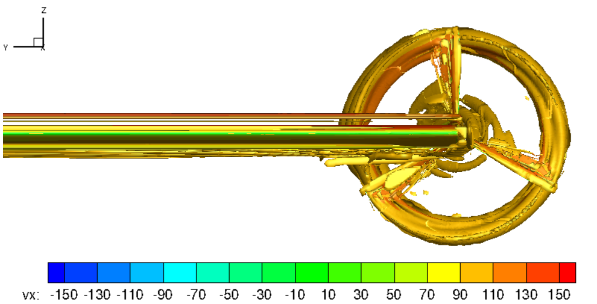

(d) Pusher (front view)

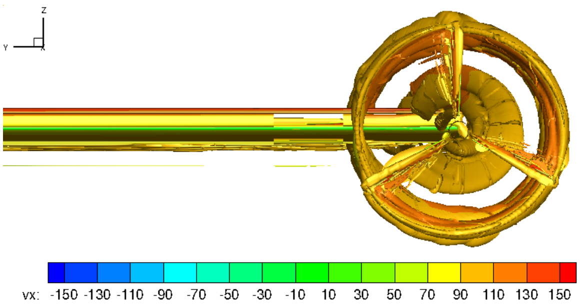

(e) Tractor (front view)

Figure 5.2: Wing-tip mounted pusher/tractor propeller RANS iso-surface of axial vorticity=1000 [s^{-1}] with contours of axial velocity

Figure 5.3 shows the wing lift distribution of all configurations analysed with body-force and meshed propeller simulations. For this, the integrated surface pressures and skin friction are translated into local normal and tangential forces and then transformed into lift and drag. The reference dynamic pressure is constantly equal to the free stream dynamic pressure. Therefore, the presented load coefficients correspond to the effective loads, including the increased slipstream dynamic pressure and not just the change in angle of attack due to the slipstream swirl. The pusher case barely shows any difference from the clean wing. The effect of the tractor propeller on the wing lift is very similar between the body-force and meshed propeller simulations.

As a further comparison, the thrust evolution over a full propeller revolution are plotted for the body-force and URANS cases. Figure 5.4a shows the entire propeller while 5.4b shows an individual blade. While a single blade sees a peak-to-peak variation in 80N in the tractor case and in 110N in the pusher case, the overall propeller thrust only varies within 20N and 40N, respectively. The steady load changes can be explained by the tractor blades exhibiting an upwash directly in front of the wing and the pusher blades exhibiting a downwash behind the wing. The pusher blades, also being disturbed by the wing wake directly behind the wing, have an additional disturbance (causing a quick oscillation of the thrust force with a magnitude of 17N), limited to the direct presence in the wake. Since these quick oscillations are occurring with a 120 degree phase shift and they are locally restrained, they are directly present in the global propeller thrust history. The steady oscillations, on the other hand, average each other out to a certain extend such that the propeller thrust history shows smaller variations. The thrust variation is rather large and is governed by a change in blade angle-of-attack due to the relatively high lift-coefficient of the wing as will become more clear in the next chapter.

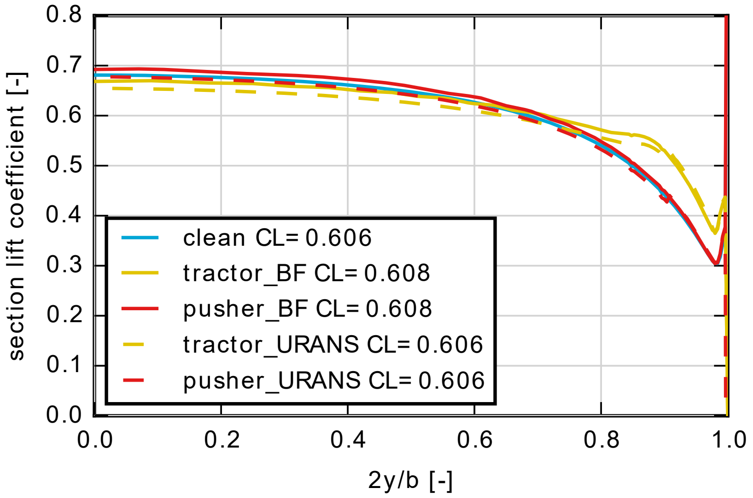

Figure 5.3: Wing-tip propeller lift distribution as obtained with URANS and body-force simulations

The oscillation magnitudes and shapes are well reproduced with the body-force approach. A phase shift of the body-force thrust history with respect to the reference can be observed. The origin of this shift has not been identified until now but may be a direct result of the implementation and the projection of the lifting-line blade forces onto the body-force domain in the RANS simulation.

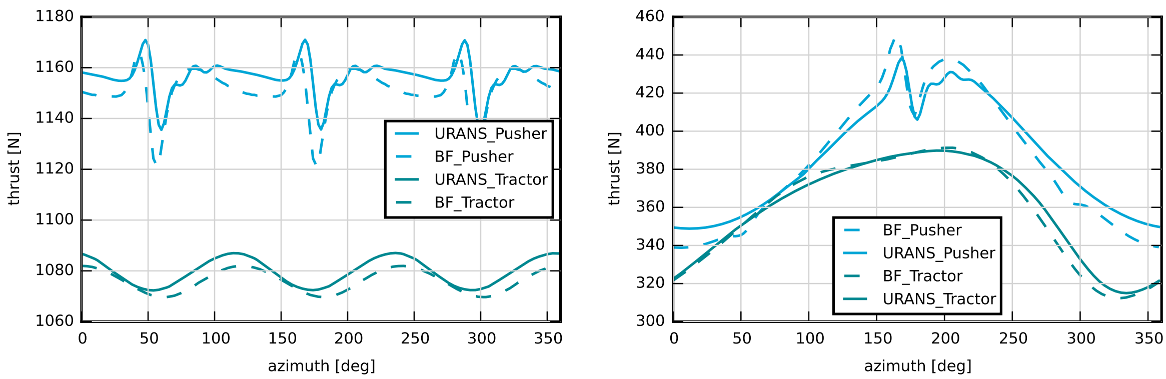

(a) Propeller thrust evolution

(b) Blade thrust evolution

Figure 5.4: Propeller and blade thrust evolutions over a full rotation for tip-mounted pusher/tractor propellers as obtained with URANS and body-force simulations

The in-plane loads of the propellers are shown in Figure 5.5a for the pusher and in Figure 5.5b for the tractor case. Again, the magnitude and shape of the oscillations match well for the two simulation strategies but the body-force loads feature a phase shift with respect to the URANS reference.

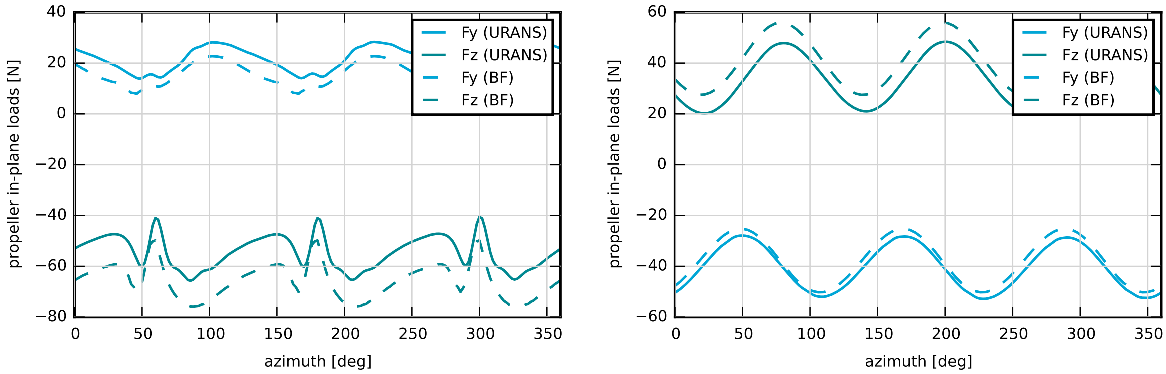

(a) Pusher in-plane loads

(b) Tractor in-plane loads

Figure 5.5: Propeller in-plane loads evolutions over a full rotation for tip-mounted pusher/tractor propellers as obtained with URANS and body-force simulations

5.1.3. DISTRIBUTED PROPELLERS

A second case with three propellers along the leading edge was analysed as well. Figure 5.6 shows the instantaneous wing surface pressures along with iso-surfaces of the q-criterion. The iso-surfaces close to the propeller blades and wing are non-physical and are a result of the Chimera meshing technique. The pitch of all three propellers is identical and no thrust or lift trim was applied. The flight conditions did not change with respect to the previous cases.

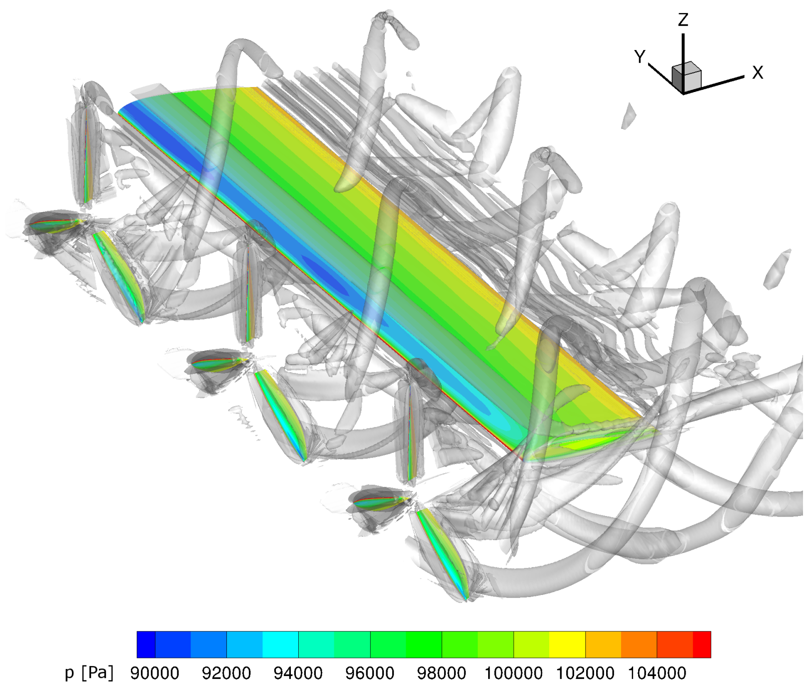

Figure 5.6: Three propeller configuration surface pressures and iso surface of q-criterion=500[1]

The results in Table 5.6 show that the lift augmentation of the two methods is identical. Also the drag coefficient is nearly the same with one drag count offset. The propeller efficiencies are, as previously, slightly differ-

[1]The q-criterion is an indicative means to visualise vortical flow structures. It is based on a positive second invariant of the velocity gradient tensor and implies a local pressure minimum which is characteristic for vortical flow structures [163].

ent but with a larger error than before. This may be attributed to the calibration of the axial load-distribution for a highly loaded propeller. With a disc loading being only a fraction of the original setting, the current source-term distribution in axial direction may not result in a very accurate induced velocity at the quarter chord any more. Therefore, the calibration seems to be inadequate for very weakly loaded propellers. This shows that for future applications, the calibration either always needs to be performed for a largely different thrust setting or that a different technique for the axial body-force distribution needs to be implemented that makes use of known airfoil characteristics or of a quick (semi-)emperical propeller induced velocity model.

Table 5.6: Performance results for wing with three distributed propellers along the leading edge as obtained with URANS and body-force simulations (thrust of body-force propellers trimmed to equal those of URANS simulation; differences under body-force defined with respect to URANS results)

	URANS	**Body-Force**
C_L [-]	0.618	0.618
α [deg]	5.5	5.5
C_D [-]	0.0217	0.0218
L/D [-]	28.5	28.4
T [N]	[370.3, 396.6, 397.8]	[370.3, 396.6, 397.8]
η_p [-]	[0.877, 0.887,0.875]	[0.911, 0.927, 0.931]
ΔC_L [%]	-	+0.0
ΔC_D [%]	-	+0.5
$\Delta(L/D)$ [%]	-	-0.4
$\Delta\eta_p$ [%]	-	[+3.4, +4.0, +5.6]

The lift distribution in Figure 5.7 shows that the lift increment of the body-force simulation is constantly slightly overestimated, indicating an over-estimation of the induced axial velocity behind the propeller. The thrust evolution of the three propellers in Figure 5.8 shows good agreement between the two methods with a slight underestimation of the body-force for the magnitude of the variation.

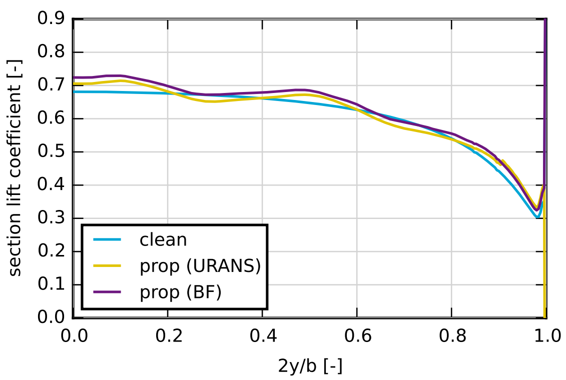

Figure 5.7: Lift distribution for three distributed leading-edge propellers as obtained with URANS and body-force simulations

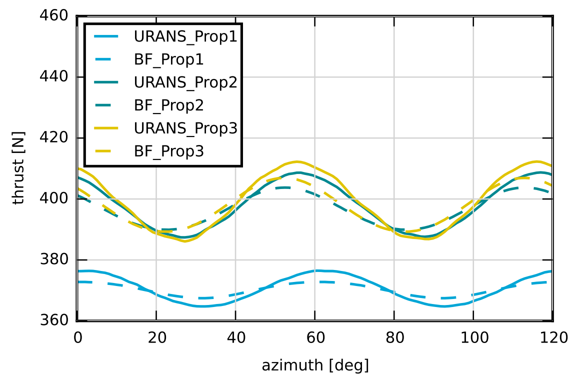

Figure 5.8: Thrust evolutions for three distributed leading-edge propellers as obtained with URANS and body-force simulations

5.2. COMPARISON TO EXPERIMENTAL SIMULATIONS

Next to the validation using different aerodynamic tools in a comparison, also a wind-tunnel test case is considered. The experimental study has been performed by Marcus as part of an ongoing M.Sc. thesis project and the results were made available as a means to validate the body-force approach [164].

The set-up consists of an over-the-wing mounted propeller. The propeller model is a De Havailland DHC-2 Beaver four-bladed scale model (see Figure 5.9b for propeller and Figure 5.9c for nacelle and sting). It has a radius of 0.118m. The wing has an NLF-22 mod-B airfoil as used on the Extra 400 aircraft and features an extendable flap. It measures 1.2m in span. A picture of the installed wing is shown in Figure 5.9a, The test was carried out in the TU Delft Low Turbulence Tunnel (LTT) facility. The rectangular test section measures 1.2m in height and 1.8m in width. The facilities' turbulence intensity is in the order of 0.01-0.2%.

(a) NLF-22 mod-B wing model in the LTT facility at TU Delft (reproduced and annotated from Veldhuis et al. [165])

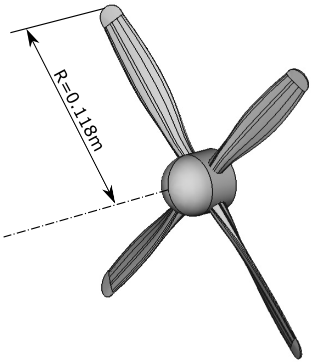

(b) Four-bladed PROWIM propeller model

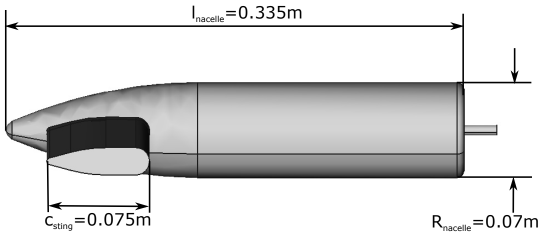

(c) Nacelle & sting models

Figure 5.9: Propeller, nacelle and sting geometries as used in experimental set-up

The propeller is positioned in an over-the-wing fashion at 0.85c with a tip-clearance of 0.01c. The airfoil is at an angle of attack of 2.08 degrees while the propeller axis horizontal axis is aligned with the free stream. Flaps are retracted to keep the meshing effort to an acceptable level. The Mach number in the test section is M=0.12. The chord-based Reynolds number is 1.65 million. The advance ratio of the propeller is set to J=0.7. From previous tests performed by Veldhuis[2], the installed propeller thrust coefficient for this configuration is known to be 0.1257 translating into a thrust of 28.81N at the rotational speed of 247.21 revolutions per second and a tip Mach number of 0.539. Therefore, the thrust of the propeller was trimmed to match this value. Knowing from previous analyses, that the lifting line model is underestimating the required pitch for a given propeller thrust setting (missing viscous & radial flow effects that lead to overestimation of thrust) this approach is assumed to result in a more realistic modeling of the propeller. The resulting pitch of the propeller in the PUMA model is 21.6 degrees while the actual pitch in the wind-tunnel was 23.0 degrees.

The CFD simulation was performed using the same numerical settings as before but on a newly generated mesh. Again, a chimera grid was used being comprised of a wind-tunnel background grid, a wing-grid, a nacelle grid, a sting grid, as well as a propeller background grid. The wind tunnel grid (see Figure 5.9b) is a cartesian grid with a refined test section. The wing, sting, and nacelle grids are O-grids with refined boundary-layers designed for $y_+ < 1$. The boundary conditions are viscous walls on the wing, sting and nacelle surfaces.

[2] L.L.M. Veldhuis: Preliminary analysis of the effect of 2D wing on propeller performance. Internal presentation, Delft University of Technology, 2017.

The wind tunnel walls are modeled with inviscid walls to keep the meshing and computational effort low. The inlet and outlet conditions are set to farfield conditions for simplicity with the inlet being 8 chords in front of the wing and the outlet being 16 chords behind the wing. The propeller was modeled using a single representative airfoil polar for the entire blade and was rotated in steps of 2 degrees. The same Weibull distributions as for the minimum induced loss propeller are employed. Further details on the grid can be found in Appendix A.

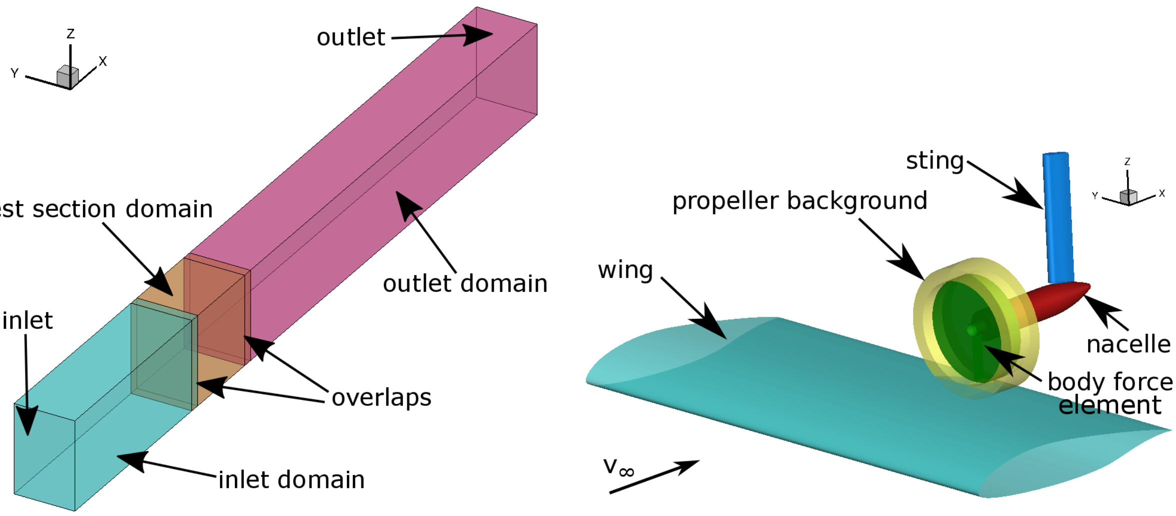

(a) Wind-tunnel domain composed of inlet, test-section and outlet

(b) Wing, propeller, nacelle & sting bodies as included in the test section with a Chimera meshing strategy

Figure 5.10: Experimental set-up grid composition showing the wind-tunnel domain and the installed models

Figure 5.11 shows the clean wing pressure distribution as obtained with the CFD simulation compared to the experimental results of Marcus. The simulation closely matches the wind-tunnel results. Significant differences are only present at the two flap gaps at the pressure and suction side of the wind-tunnel model (the airfoil has been included in the graph to show that the offsets exactly occur at the gap locations). These gaps have not been resolved in the CFD mesh and hence, the solution slightly differs at these points. This reference pressure distribution is used in the following to show the effect of the propeller and nacelle on the wing surface pressure. It is the difference in pressures which is compared because the low propeller loading of the set-up makes it difficult to see the difference between two graphs of a propeller being present or not.

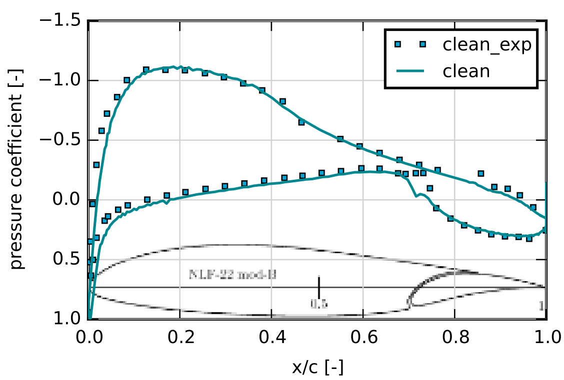

Figure 5.11: NLF-22 mod-B isolated wing pressure distribution RANS validation with experimental results from [164]

The more important results to validate the modeling of propellers in the vicinity of wings are those that show the effect of the propeller on the flow. These results are shown in Figure 5.12. For the experimental results in

Subfigure 5.12a, the difference between the wing-nacelle-propeller configuration and the wing-nacelle configuration is presented. For the numerical results in Subfigure 5.12b, the difference between the isolated wing and the wing-propeller configuration is displayed. This means that possible interference effects with the nacelle are included in the experimental solution. It should further be noticed that the use of different software packages for the creation of the plots with differing color scales are another error source although it was tried to match the scales as well as possible. The presented difference in pressure coefficient is determined with Equation 5.1.

Despite the mentioned error sources, the qualitative comparison shows that the effect of the propeller is well captured by the body-force method. The global effects of increased suction upstream and decreased suction downstream of the propeller on the suction side of the wing can clearly be seen. Additionally, the increased pressure at the leading edge of the pressure side of the wing is distinguishable and equal in magnitude as well. Some differences, however, are apparent as well. First of all, a low pressure region on the trailing edge, extending over both the suction and pressure side, is present in the body-force result but is missing in the experimental study. Additionally, the small suction region on the pressure side of the wind-tunnel model was not found in the numerical solution. Another difference can be observed in the direct vicinity of the propeller. While the pressure and suction regions in the experiment are exactly split by the propeller disc, the transition area in the CFD results is shifted slightly upstream.

Subfigures 5.12d and 5.12e show local pressure difference distributions at a quarter and a half propeller radius outboard from the propeller center line. It can be seen that the experiment is well matched except for the pressure jump across the propeller disc. The discontinuity is less pronounced in the numerical simulation close to the propeller center line. This behaviour can have multiple reasons. One of them is that the propeller loading is not matching exactly with the experiment. Since the propeller loads were not measured during the test campaign, only reference data was used to estimate the thrust coefficient from the advance ratio. This reference, however, is assumed to be quite accurate. Furthermore, the load distribution of the lifting-line model was estimated using a single representative airfoil polar (not the case for other parts of this report!) and the chord-wise distribution utilised the same calibration as for the minimum induced velocity propeller as used in the rest of the report. For these reasons, a local difference in the interaction of propeller and wing can be expected. The spikes in the numerical results occur at the same chord-wise locations in both span-wise positions. Their magnitude is very small with respect to the absolute pressure coefficients and have a negligible effect on the solution. It is, however, not clear what the origin for these peaks is.

$$\Delta C_p = \left(\frac{p - p_\infty}{q_\infty}\right)_{prop} - \left(\frac{p - p_\infty}{q_\infty}\right)_{no-prop} \tag{5.1}$$

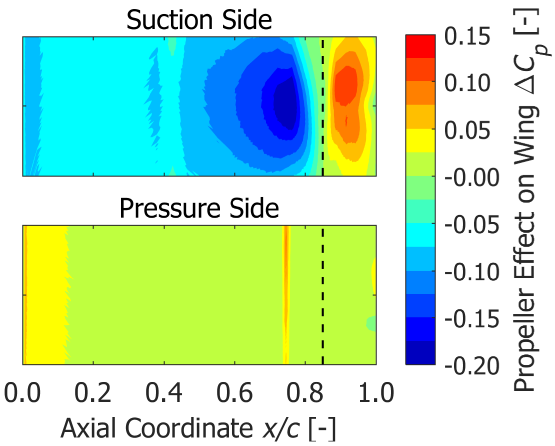

(a) Experimental $Cp_{prop-nacelle-wing} - Cp_{nacelle-wing}$ (reproduced from [164])

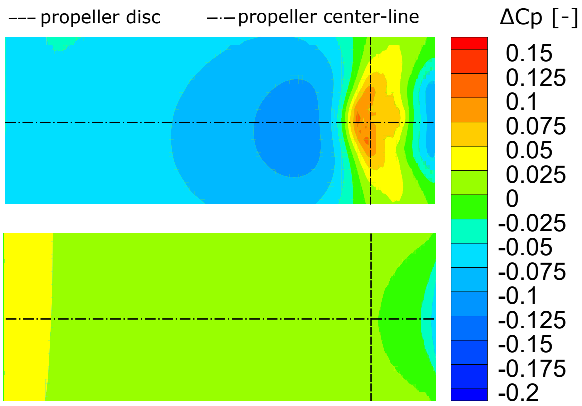

(b) Numerical $Cp_{prop-wing} - Cp_{wing}$ (obtained with the body-force method)

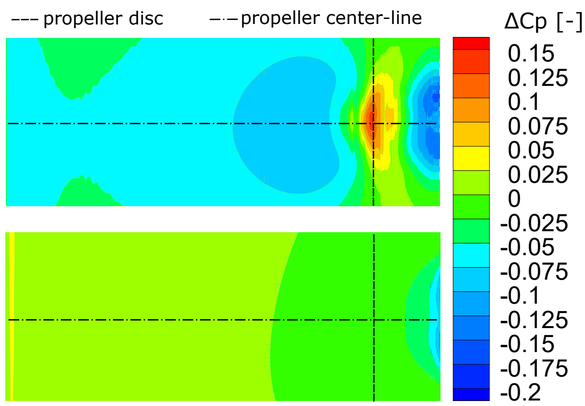

(c) Numerical $Cp_{prop-nacelle-wing} - Cp_{nacelle-wing}$ (obtained with the body-force method)

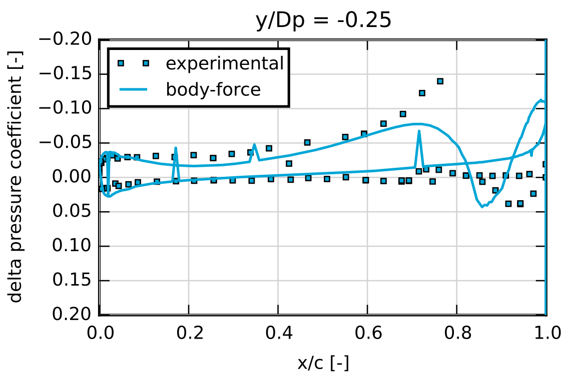

(d) Comparison at a half radius from propeller center-line $Cp_{prop-nacelle-wing} - Cp_{nacelle-wing}$

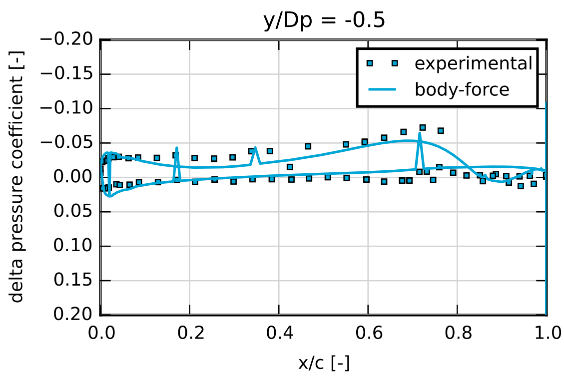

(e) Comparison at a one radius from propeller center-line $Cp_{prop-nacelle-wing} - Cp_{nacelle-wing}$

Figure 5.12: Propeller effect on wing surface pressure coefficient validation (J=0.7)

A second means to validate approach is the comparison of wake plane total pressure measurements at 3.2 propeller diameters behind propeller plane equivalent to 2.1 chord lengths behind wing leading edge. The results are presented in Figure 5.13. The total pressure coefficients are computed with Equation 5.2.

$$C_{p_t} = \frac{p_t - p_\infty}{q_\infty} \tag{5.2}$$

The comparison shows again a good agreement between the experimental and numerical simulations. The magnitude and general behaviour of the total pressure in the wake plane are similar. However, the effect of numerical diffusion can well be identified for the wing wake as well as for the propeller slipstream which are both less sharp captured more than one chord length behind the wing trailing edge. Additional figures presenting the axial velocity contours at the propeller mid-plane as well as an angle-of-attack map for the propeller can be found in Appendix B for the reader's interest.

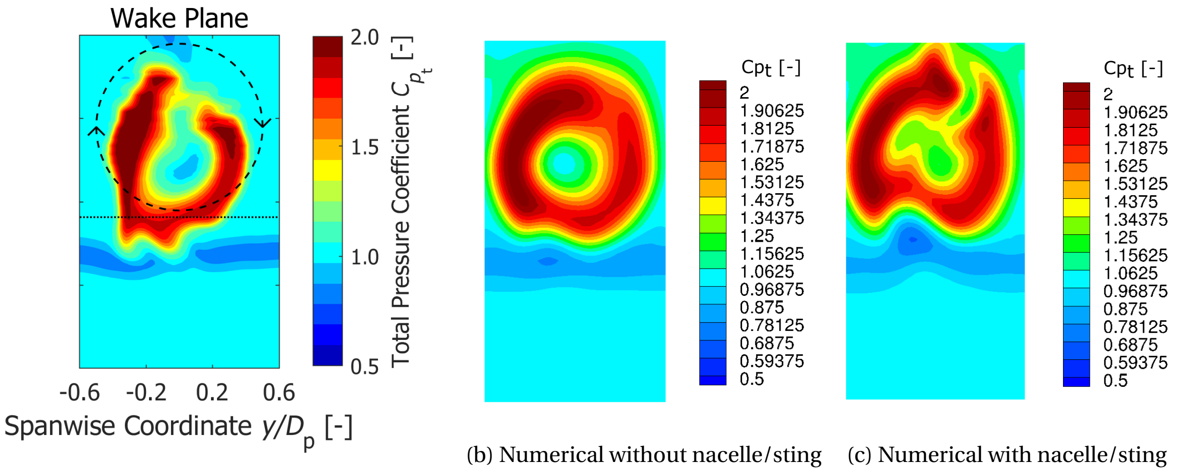

(a) Experimental (reproduced from [164])

(b) Numerical without nacelle/sting (obtained with body-force method)

(c) Numerical with nacelle/sting (obtained with body-force method)

Figure 5.13: Wake plane total pressure validation ($J = 0.7$, C_{p_t} dimensionless)

6

Simulation Results

Having implemented and validated the body-force approach for the simulation of closely coupled propellers and wings, the method can be applied to the cases of interest as described in Chapter 3. The results for the performed simulations are presented in the following sections. First, tip-mounted propellers are shown. The second section deals with lift-augmenting configurations.

6.1. Tip-Mounted Propellers

All simulations on wing-tip propellers are done for pusher and tractor variants for comparison of both options. Additionally, the same configuration is compared for non-twisted and ideally-twisted wings.

6.1.1. Pusher & Puller Configuration (Untwisted Wing)

The first results are presented for the untwisted wing with constant NACA23012 cross-section and without sweep or taper. The 0.8m-radius propeller designed for minimum induced loss with a tip Mach number of 0.5 is mounted one radius in front of the wing-tip leading edge (tractor) or one radius behind the wing-tip trailing edge (pusher). The flight conditions are a Mach number of 0.3 at SL conditions at a lift coefficient of 0.6. For a fair comparison between the two cases, an overall lift-to-drag ratio for the aircraft of 16.8 was assumed for a cruise lift coefficient of 0.6 and taking the difference between the corresponding drag and the clean wing drag as a fixed drag term for the aircraft minus wing $D_{ac-w} = 924$N. The thrust of each configuration is then trimmed to the total drag of the configuration ($T = D_{ac} = D_{ac-w} + D_w$).

Table 6.1 shows the results. A first observation is the reduced wing angle of attack for the tractor configuration, required for keeping the lift coefficient constant, despite the lift-augmenting effect of the slipstream. The pusher propeller, on the other hand, has no measurable effect on the wing lift.

Furthermore, the drag variation due to the propeller installation can be compared. The pusher configuration has an additional 0.9% of wing drag. The tractor configuration has a reduction of 9.8% in wing drag. Due to the thrust-drag balance, the thrust setting of the pusher propeller is increased while the tractor propeller is trimmed to a lower thrust setting. Additionally, the propeller efficiency is affected significantly by the change in inflow conditions. The pusher propeller efficiency increases by 8.7% while the tractor propeller benefits by 0.6%. Therefore, both configurations have a positive effect on the propeller efficiency.

For a global comparison of the different trimmed configurations, the required propeller shaft power is a meaningful figure of merit. All effects of wing drag reduction, propeller efficiency change and propeller trim are included in this performance metric with their respective weight on overall aircraft performance. The pusher case has shown a large increase in propeller efficiency but suffers slightly from induced wing drag and thus increased required thrust. These effects translate into a required power reduction of 8.5%. The tractor configuration benefits from a significant wing drag reduction and additionally gains some propeller efficiency paired with less required thrust. Since the wing drag, however, only constitutes a fraction of overall aircraft drag, the effect on required shaft power (6.9% reduction) is less pronounced than for the pusher case. Clearly, this conclusion is not generally valid as it strongly depends on the wing drag fraction of the total aircraft drag that is based on the assumed aircraft lift-to-drag ratio. Additionally, the design choices on propeller and wing geometry and operating conditions can change which configuration is more efficient.

Table 6.1: Body-Force results for wing-tip mounted pusher/tractor propellers on an untwisted wing. Differences defined with respect to isolated wing & propeller (SL+0, $M = 0.3$, $T = D_{ac}$, $D_{ac-w} = 924$N, $M_{tip} = 0.5$)

	pusher	**tractor**	**iso**
C_L [-]	0.606	0.608	0.606
α [deg]	5.5	5.25	5.5
C_{D_w} [-]	0.0216	0.0193	0.0214
$(L/D)_w$ [-]	28.1	31.6	28.3
L/D [-]	16.8	18.1	16.9
D [N]	2302	2153	2296
T [N]	2302	2152	2296
$\beta_{0.75R}$ [deg]	39.16	41.40	41.93
η_p [-]	1.000	0.919	0.913
P_{shaft} [kW]	235.1	239.1	256.9
ΔC_{D_w} [%]	+0.9	-9.8	-
ΔC_D [%]	+0.3	-6.2	-
$\Delta \eta_p$ [%]	+8.7	+0.6	-
ΔP_{shaft} [%]	-8.5	-6.9	-

The lift and drag distributions of the two configurations are compared to the isolated wing in Figures 6.1a and 6.1b. Again, the coefficients are based on the integrated surface pressures and skin friction of the flow solution. The lift curve shows that the additional lift in the tractor case is indeed generated at the wing tip inside and close to the propeller slipstream. At the inner parts of the wing, the reduced angle of attack results in a slightly reduced local lift. The change in drag coefficient can be localised at the wing tip as well for the tractor configuration. While the reduction extends over the whole span, the largest difference is situated at about 90% of the semi-span. Also the pusher configuration shows an inboard drag reduction but increased drag at the very tip of the wing. The sudden change in drag very close to the root is believed to stem from the integration method and is non-physical.

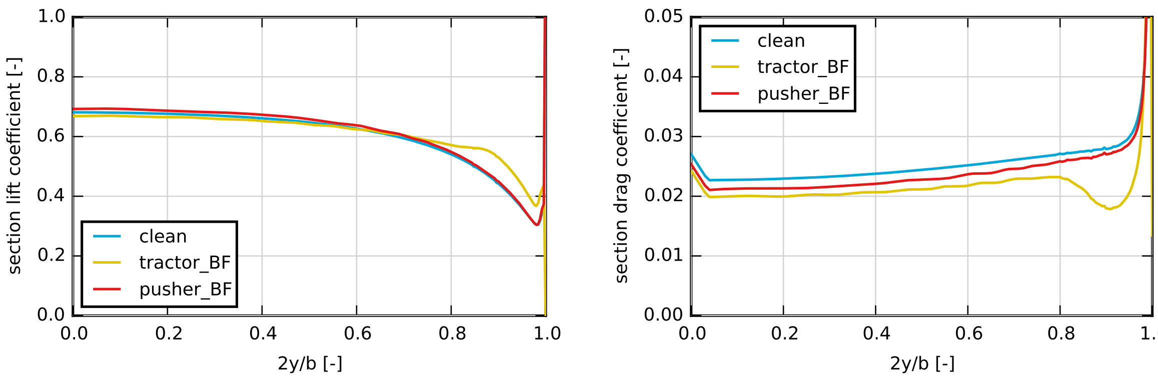

(a) Lift distributions

(b) Drag distributions

Figure 6.1: Lift & drag distributions for untwisted wing with tip pusher/tractor (SL+0, $M = 0.3$, $T = D_{ac}$, $D_{ac-w} = 924$N, $C_L = 0.6$, $M_{tip} = 0.5$)

To see how these changes in local lift and drag are generated the local pressure distributions at different span-wise sections are compared in Figure 6.2. Clearly, the individual configurations are hardly differentiable from the root to 80% of the semi-span. At 90% and 95% the tractor configuration shows a significant offset at the most upstream quarter of the sections. Having the change in surface pressure at the foremost part of the wing, the resultant force not only grows, but also tilts towards the leading edge. Therefore, lift increases while drag decreases.

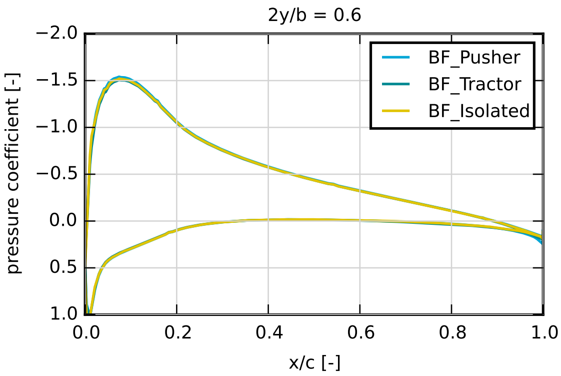

(a) Wing section outside slipstream ($y/R = 2.5$)

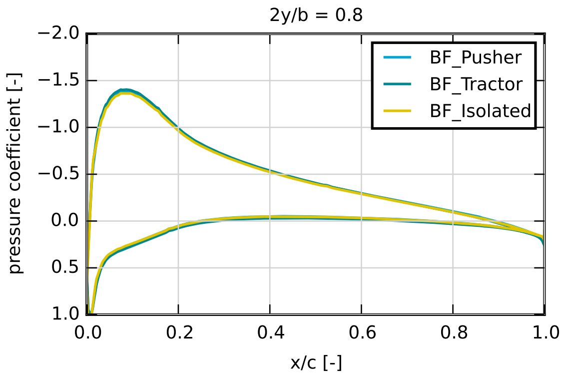

(b) Wing section outside slipstream ($y/R = 1.25$)

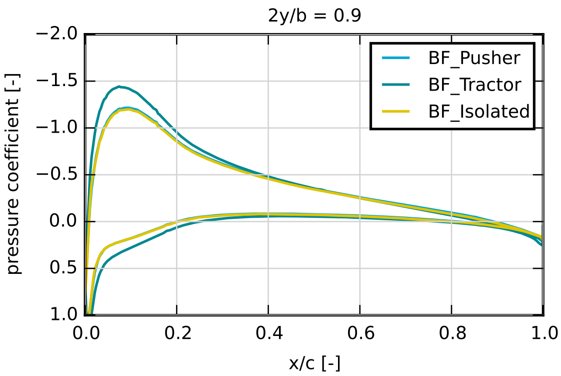

(c) Wing section inside slipstream ($y/R = 0.625$)

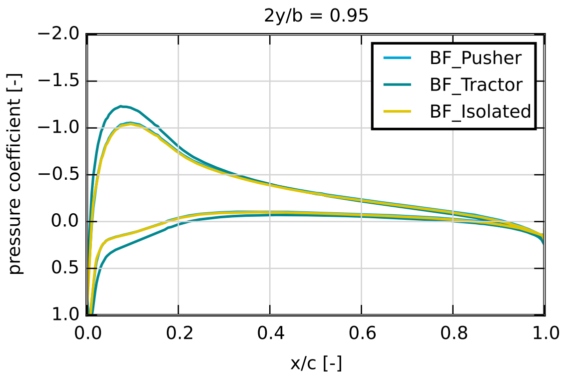

(d) Wing section inside slipstream ($y/R = 0.3125$)

Figure 6.2: Local pressure distributions at different span-wise stations of an untwisted wing with tip-mounted pusher/tractor propeller (SL+0, $M = 0.3$, $T = D_{ac}$, $D_{ac-w} = 924$N, $C_L = 0.6$, $M_{tip} = 0.5$)

Also the wing effect on the propeller is visualised in Figure 6.3. Part 6.3a shows the thrust history of the propeller over one full revolution. The isolated propeller has a constant thrust while that of the installed versions feature significant variations. Both, pusher and tractor, have a rather smooth sinusoidal variation, governed by the wing up-/down-wash seen by the propeller blades when entering the span-wise positions in front of or behind the wing. The pusher shows an additional strong variation at the azimuthal positions where the blades cross the wing wake.

These global thrust variations become more clear when comparing the angle-of-attack maps of the different propellers. These show the local blade section angle of attack. The maps are shown as seen from upstream (See Figure 3.4 for definition of the azimuth Ψ). The isolated propeller has a completely constant loading in azimuthal direction and only minor variations in radial direction. The tractor propeller has a reduced pitch setting and hence also a generally lower loaded blade. Additionally, the up-wash from the wing leads to a further de-loading, most prominent between 180 and 270 degrees azimuth. The pusher configuration shows the largest variations. First of all, the inner blade sections have a strong additional radial inflow angle from the wing-tip vortex swirl. Secondly, the wing wake and its reduced axial velocity result in a higher blade loading close to 180 degrees azimuth.

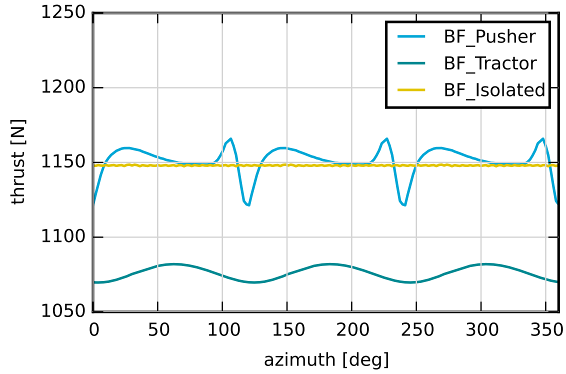

(a) Propeller thrust history

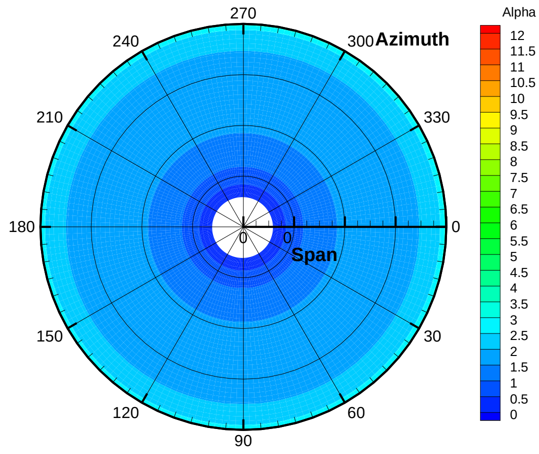

(b) Isolated propeller blade angle-of-attack map

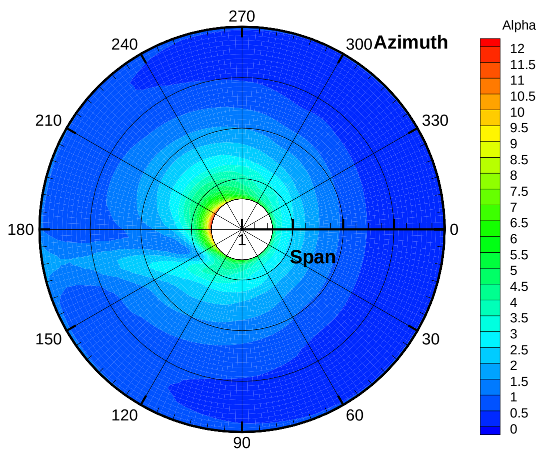

(c) Pusher propeller blade angle-of-attack map

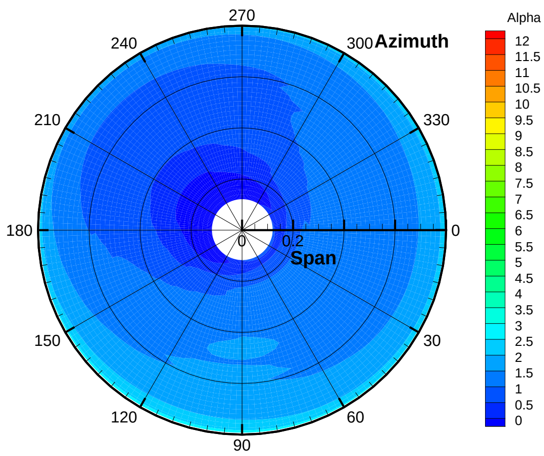

(d) Tractor propeller blade angle-of-attack map

Figure 6.3: Wing-tip mounted pusher/tractor propeller thrust evolution and effective blade angle-of-attack maps (SL+0, $M = 0.3$, $T = D_{ac}$, $D_{ac-w} = 924\text{N}$, $C_L = 0.6$, $M_{tip} = 0.5$)

6.1.2. PUSHER & PULLER CONFIGURATION (IDEALLY TWISTED WING)

Most real wings, contrary to that of the previous section, are optimised for minimum induced drag. It is therefore interesting to assess if a configuration with ideally twisted wing can gain a similar amount of performance increase by installing propellers at the tip.

Table 6.2 shows the results as for the non-twisted wing in the previous section. The results change for the pusher configuration in that the propeller can gain less efficiency increase, compared to the non-twisted wing case. As a result, the propeller shaft power requirement reduces less by an amount og 6%. The tractor propeller on the other hand does lead to an equally large wing drag reduction as for the non-twisted wing. Also the propeller gains more in efficiency. As a result, the relative change in propeller power does not reduce as much as for the pusher configuration. Overall, this leads to a change in conclusion with regard to the global comparison. Both configurations are now equally ably to save power consumption.

Table 6.2: Body-Force results for wing-tip mounted pusher/tractor propellers on an ideally twisted wing. Differences defined with respect to isolated wing & propeller (SL+0, $M = 0.3$, $T = D_{ac}$, $D_{ac-w} = 924$N, $M_{tip} = 0.5$)

	pusher	**tractor**	**iso**
C_L [-]	0.609	0.610	0.608
α [deg]	5.5	5.25	5.5
C_{D_w} [-]	0.0211	0.0188	0.0209
$(L/D)_w$ [-]	28.9	32.4	29.1
L/D [-]	17.1	18.3	17.2
D [N]	2267	2126	2256
T [N]	2268	2136	2256
$\beta_{0.75R}$ [deg]	39.70	41.37	41.81
η_p [-]	0.977	0.919	0.899
P_{shaft} [kW]	237.0	237.3	252.2
ΔC_{D_w} [%]	+1.0	-10.0	-
ΔC_D [%]	+0.5	-5.8	-
$\Delta\eta_p$ [%]	+7.8	+2.0	-
ΔP_{shaft} [%]	-6.0	-5.9	-

The lift and drag distributions of the two configurations are compared to the isolated wing in Figure 6.4. The lift-distribution has a shape that is much closer to an elliptic one that before. The relative changes from the tractor propeller, however, remain unchanged. Also the inboard kink in drag distribution is again a result of the integration method and is non-physical.

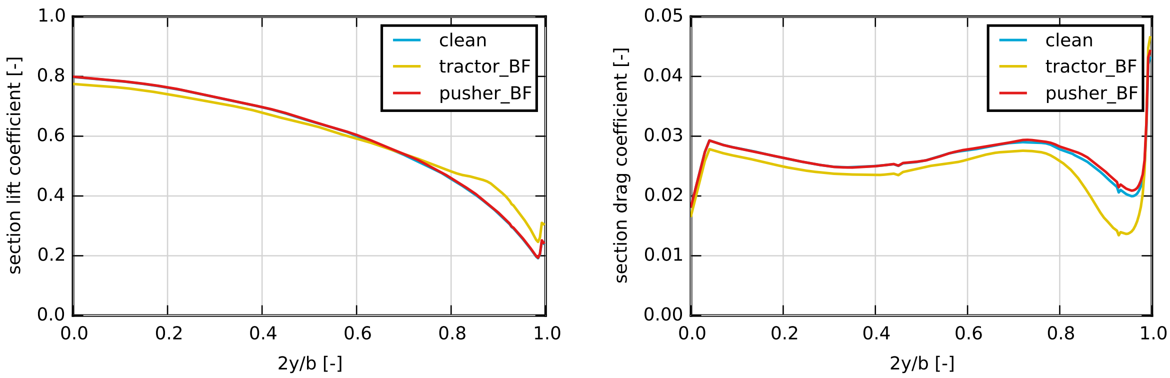

(a) Lift distributions

(b) Drag distributions

Figure 6.4: Lift & drag distributions for an ideally twisted wing with tip pusher/tractor (SL+0, $M = 0.3$, $T = D_{ac}$, $D_{ac-w} = 924$N, $C_L = 0.6$, $M_{tip} = 0.5$)

This is also the case for the sectional pressure distributions as shown in Figure 6.5. As before, the inboard sections are not significantly affected by the propeller but the upwash from the propeller swirl and the increased axial velocity lead to a pronunciation of the pressure distributions close to the leading edge. Because of the fact that the drag reduction is achieved by this effect, rather than by a pure tip vortex attenuation, the relative change in wing drag is as large as for a non-twisted wing.

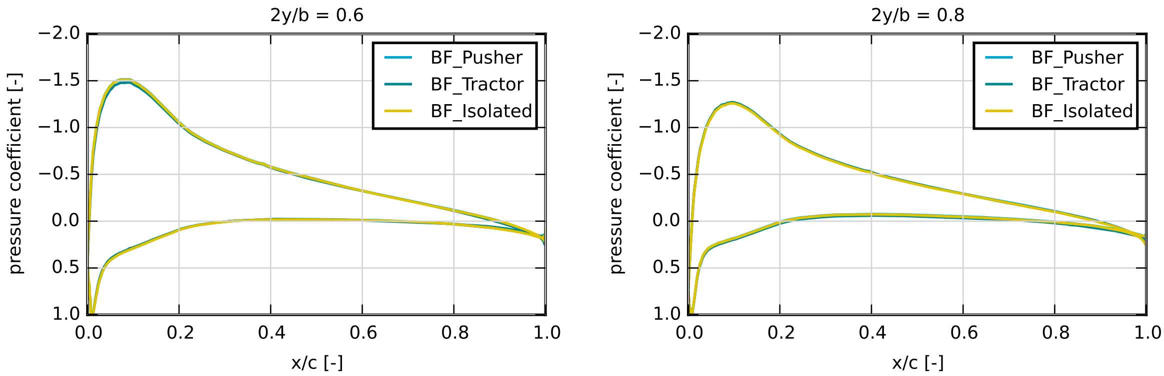

(a) Wing section outside slipstream ($y/R = 2.5$)

(b) Wing section outside slipstream ($y/R = 1.25$)

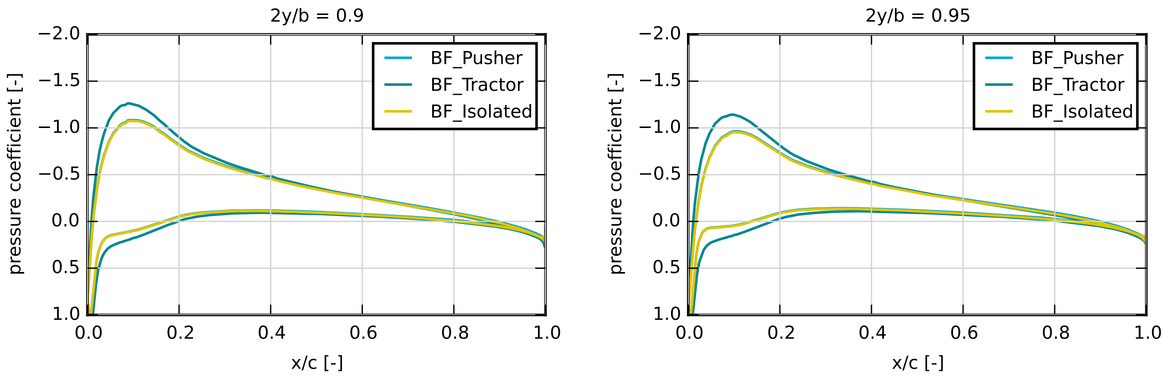

(c) Wing section insedtside slipstream ($y/R = 0.625$)

(d) Wing section outside slipstream ($y/R = 0.3125$)

Figure 6.5: Local pressure distributions at different span-wise stations of an ideally twisted wing with tip-mounted pusher/tractor propeller (SL+0, $M = 0.3$, $T = D_{ac}$, $D_{ac-w} = 924$N, $C_L = 0.6$, $M_{tip} = 0.5$)

Finally, the propeller performance can be analysed in more detail with the help of Figure 6.6. It can be seen, that the thrust variation over a propeller revolution is similar to the non-twisted wing. However, the change in blade loading due to the tip-vortex inflow swirl on the pusher propeller is less pronounced for the ideally-twisted wing. The reduced tip-vortex strength reduces the additional thrust gained from the propeller-wing coupling. As a consequence, the pusher propeller configuration can not gain as much in power consumption as in the non-twisted wing case while the tractor configuration does not suffer from the twist. As seen before, this results in the tractor now being as good in reducing power consumption which was not the case for the non-twisted wing configuration.

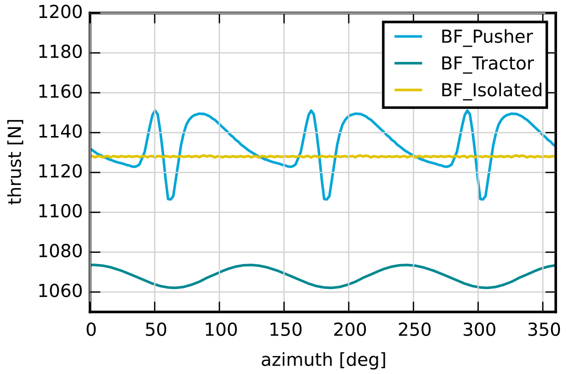

(a) Propeller thrust history

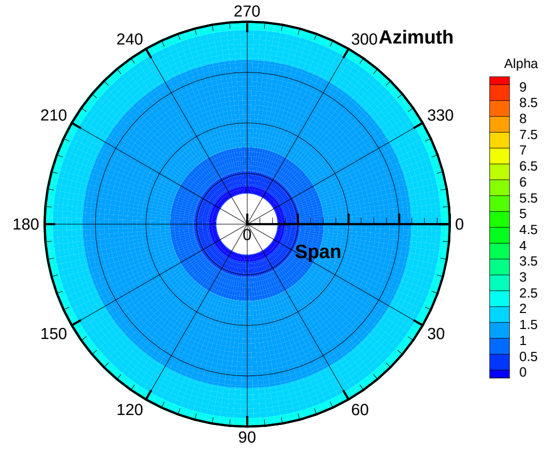

(b) Isolated propeller blade angle-of-attack map

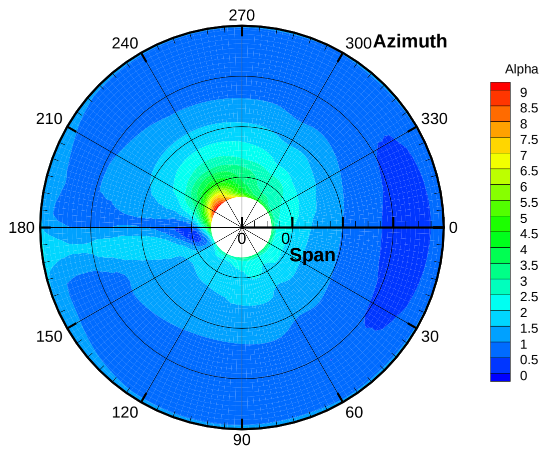

(c) Pusher propeller blade angle-of-attack map

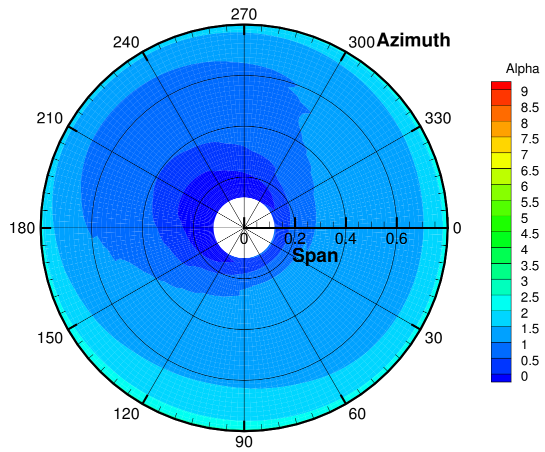

(d) Tractor propeller blade angle-of-attack map

Figure 6.6: Wing-tip mounted pusher/tractor propeller thrust evolution and effective blade angle-of-attack maps (SL+0, $M = 0.3$, $T = D_{ac}$, $D_{ac-w} = 924$N, $C_L = 0.6$, $M_{tip} = 0.5$)

Further body-force results for wing-tip mounted propellers can be found in Appendix B. This includes wing surface pressure distributions as well as total pressure and axial vorticity contours at different axial distances downstream of the wing. Additionally, some variable sweeps are included that have been performed with the free-wake lifting-line code.

6.2. LIFT-AUGMENTING PROPELLERS

This section shows the result for the lift-augmenting propeller configurations. First, the elongated isolated wing results are presented. Subsequently, the results for leading-edge propellers and over-the-wing propellers are discussed. When speaking of the lift augmentation, a difference can be made between the pure change in wing lift ΔC_L and the effective change in wing lift $\Delta C_{L_{eff}}$ including the thrust component in vertical direction as well as the vertical propeller in-plane loads.

6.2.1. ISOLATED WING

First of all, the isolated wing was analysed with the lifting-line and RANS codes. For the body-force method, the angle of attack was set to 5.5 degrees. The faster lifting-line code was applied to a range of angles. The results are shown in Table 6.3.

Table 6.3: Isolated wing performance as predicted by RANS and lifting-line simulations (SL+0, $v_\infty = 61$kts, $Re = 2.2 \cdot 10^6$)

method	α **[deg]**	C_L [-]	C_D [-]	$C_{M_{y,0.25c}}$ [-]	L/D [-]
BF	5.5	0.618	0.0179	-0.0714	34.5
PUMA	0.0	0.118	0.0054	-	21.9
PUMA	2.25	0.341	0.079	-	43.2
PUMA	5.5	0.664	0.0160	-	41.5
PUMA	7.75	0.839	0.0226	-	37.1

6.2.2. LEADING-EDGE PROPELLERS

This section contains the results for leading-edge mounted propellers. Table 6.4 summarises the results obtained with the body-force approach and the lifting-line code. For these results, the propeller has been aligned with the free stream, a constant 5.5 degree wing pitch was applied and a constant disk loading of 1000 N/m^2 was imposed on the propellers. This is a choice representing an approximate average value for proposed concepts as shown in the first chapters. The number of propellers and their sense of rotation was altered to observe their effect on the results. The index '2' is introduced to differentiate the two contra-rotating cases for the most outboard propeller moving inboard downwards (contra) and moving inboard upwards (contra2).

First of all, the focus is shifted to the body-force results. All variations manage to increase the lift by 50%. The highest lift augmentation is achieved with the contra-rotating propellers with the outboard engine running inboard upwards. The outboard engine running inboard downwards has a slightly smaller lift-augmentation with additional drag. The contra-rotating engines lead to higher in-plane loads but require less shaft power. A lower propeller number leads to a slightly higher lift augmentation with less drag but at the cost of a third more required total shaft power.

The lifting-line results obtained with PUMA show similar trends except for the lift augmentation for the reduced number of propellers. The absolute numbers, however, are off by about 20% for the lift augmentation and required power. Also the high in-plane loads of the contra-rotating propellers are not found. It can further be seen that a higher number of 20 propellers leads to a higher lift augmentation at lower required total shaft power. This observation, however, has to be seen critically because the thickness effect of the wing and the fact that parts of the wing may not be inside the slipstream are not covered with the lifting-line theory.

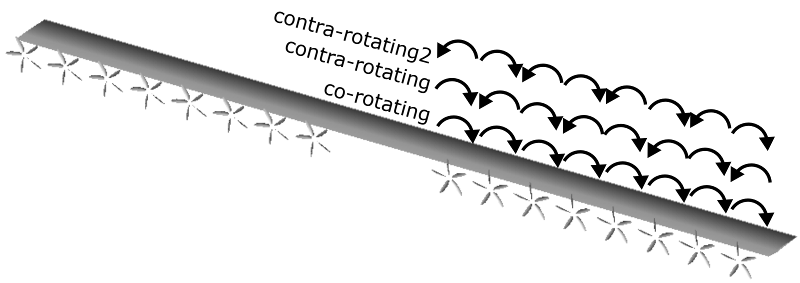

Figure 6.7: High-lift propeller configuration propeller sense of rotation

Table 6.4: Results for leading-edge high lift propellers obtained with body-force and lifting-line simulations. Change in lift with respect to isolated wing (propeller aligned with free steam, $\alpha = 5.5$ deg, $T/A = 1000$ N/m^2)

method	N_P [-]	**rotation**	C_L [-]	C_D [-]	L/D [-]	$C_{L_{eff}}$ [-]	ΔC_L [%]	$\Delta C_{L_{eff}}$ [%]	F_z/T [%]	P [kW]
BF	16	co	0.927	0.0472	19.7	0.941	+50.0	+52.3	1.78	307
BF	16	contra	0.941	0.0475	19.8	0.965	+52.3	+56.2	3.08	299
BF	12	co	0.943	0.0313	30.1	0.958	+52.6	+54.9	1.40	415
BF	16	contra2	0.964	0.0458	21.1	0.988	+56.0	+60.0	3.07	299
PUMA	16	co	1.134	0.0321	35.3	1.143	+70.9	+72.2	1.17	352
PUMA	16	contra	1.191	0.0243	49.0	1.200	+79.5	+80.8	1.16	351
PUMA	12	co	1.127	0.0283	39.8	1.139	+69.8	+71.6	1.18	469
PUMA	20	co	1.210	0.0299	40.5	1.218	+82.3	+83.5	1.25	281

Figure 6.8 shows the span-wise lift distribution for the two different simulation methods. The isolated wing is compared to the 16 propeller configuration with co- and contra-rotating propellers. The magnitude of the lifting-line lift peaks is significantly higher that that of the body-force simulation (especially in case of contra-rotating propellers). This may be an indication that the span-wise section number is too low to accurately resolve the influence of the many propellers. The body-force results show that the local lift is fluctuating strongly with peaks of up to nearly 1.5.

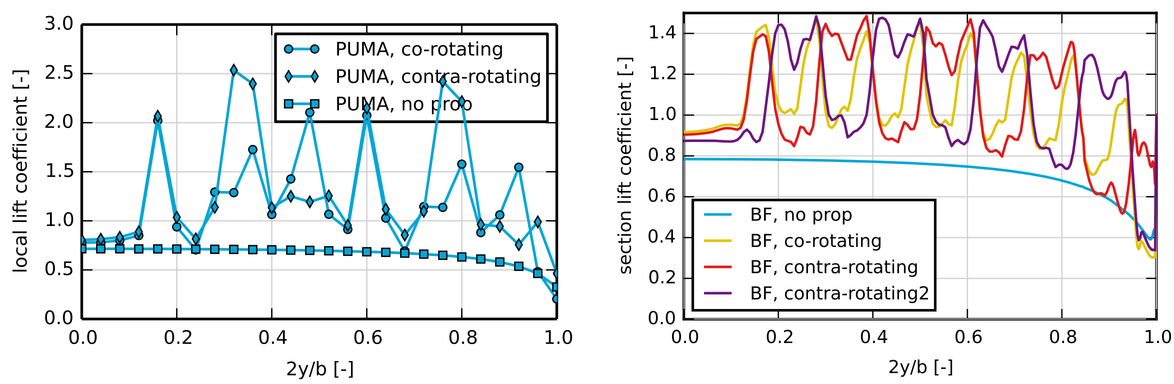

(a) PUMA free-wake lifting-line results

(b) Body-force results

Figure 6.8: Wing lift distributions with installed leading-edge high-lift propellers obtained with lifting-line and body-force simulations (propeller aligned with free steam, $\alpha = 5.5$ deg, $N_p = 16$, $T/A = 1000$ N/m^2)

Figure 6.9 shows the wing pressure distribution with iso axial vorticity contours for co- and counter-rotating propellers. It can be seen how the slipstream washes over the majority of the wing and how the strong fluctuations in wing pressure occur behind the propellers. These fluctuations are repeated at each propeller for the co-rotating propellers and are concentrated every second propeller for the contra-rotating propellers.

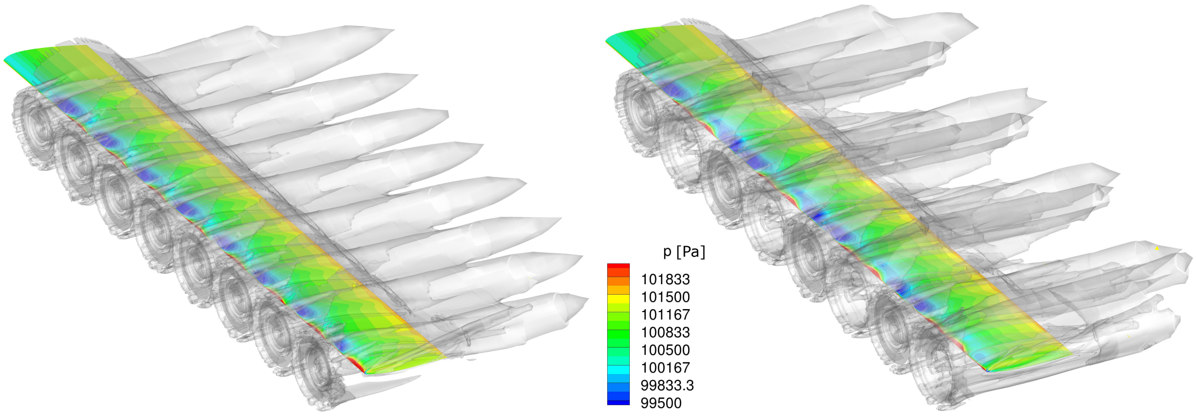

(a) co-rotating

(b) contra-rotating

Figure 6.9: Wing pressure distribution & axial vorticity iso-surfaces $\omega_x = 20\text{s}^{-1}$ with leading-edge high-lift propellers for co- and counter-rotating propellers (p in Pa, propeller aligned with free steam, $\alpha = 5.5$ deg, $N_p = 16$, $T/A = 1000\ \text{N/m}^2$)

Figure 6.10 shows the wake of the lifting-line code for a case with 16 propellers, co-rotating inboard-up at each half-span. The strong wing wake deformation due to the presence of the propellers is clearly visible. The wake panels are coloured according to their circulation strength.

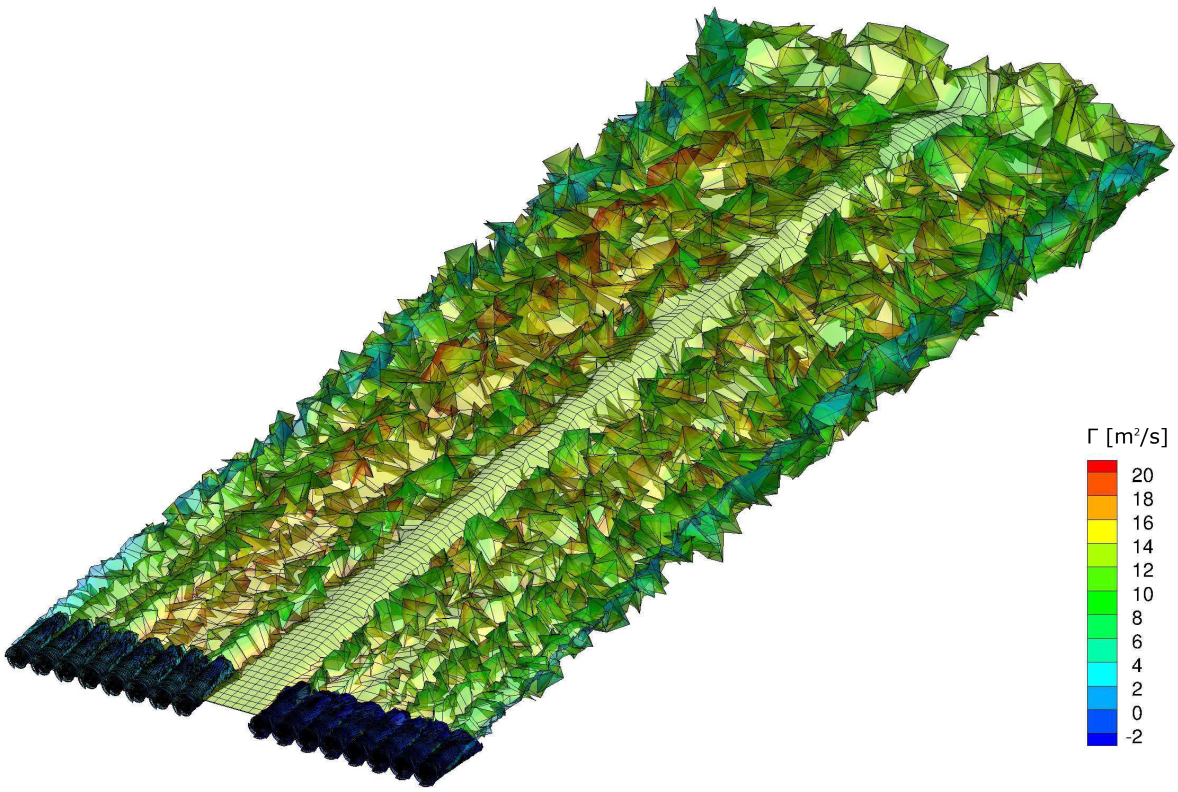

Figure 6.10: PUMA free-wake lifting-line wake model with indicated wake panel circulation strength for co-rotating leading-edge high-lift propellers (propeller aligned with free steam, $\alpha = 5.5$ deg, $N_p = 16$, $T/A = 1000\ \text{N/m}^2$)

The wing surface pressure of the co-rotating propeller case is shown in Figure 6.11 with axial velocity contours at three different span-wise locations. One at the inboard wing portion without direct slipstream effect, one at the center-line of a propeller and one between to propellers. The high speed region is very pronounced at the centre-line of the propellers but is still stronger between the propellers with respect to the isolated wing.

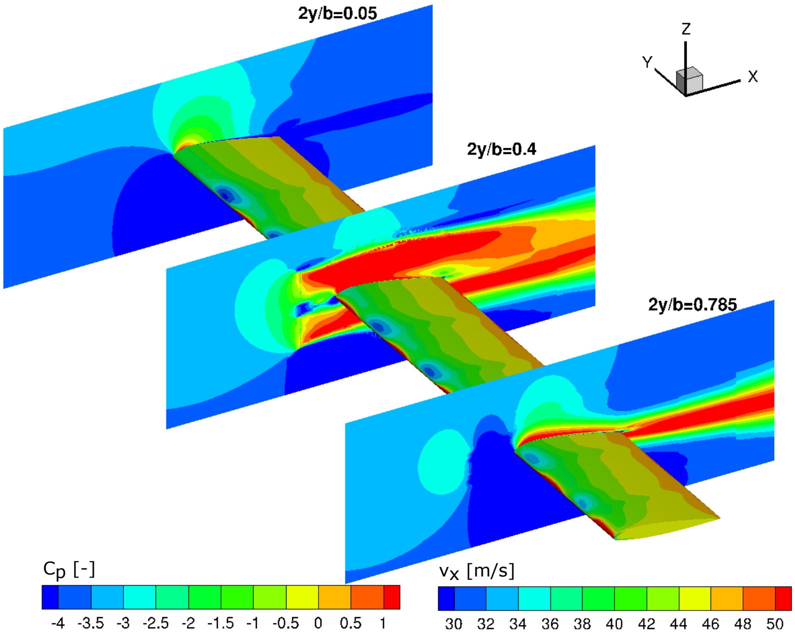

Figure 6.11: Wing surface pressure coefficient and axial velocity fields at unblown mid-wing (2y/b=0.05), center-line of a propeller (2y/b=0.4) and between two propellers (2y/b=0.785) for the case with 16 co-rotating propellers (C_p dimensionless, v_x in m/s)

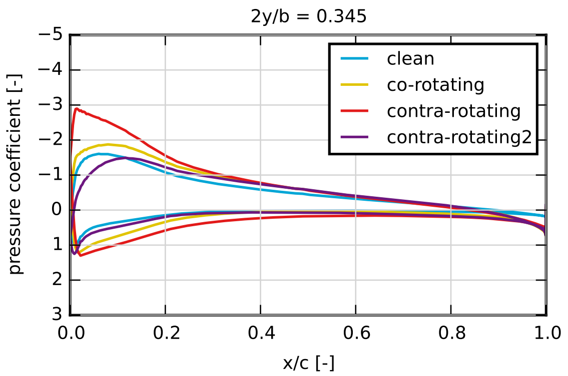

(a) between two propellers

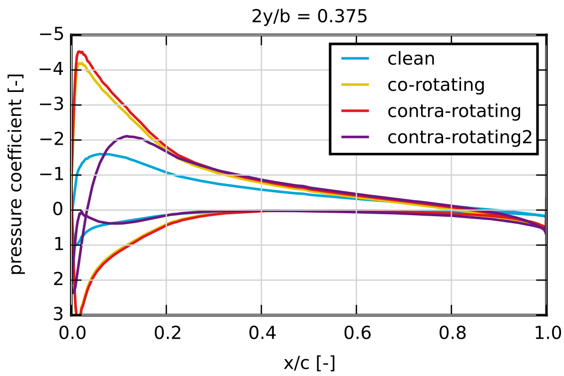

(b) behind blade

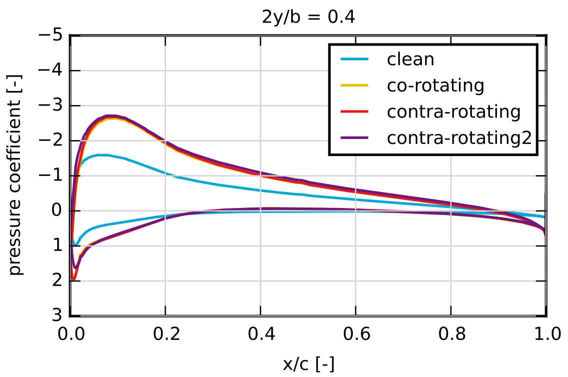

(c) at propeller center-line

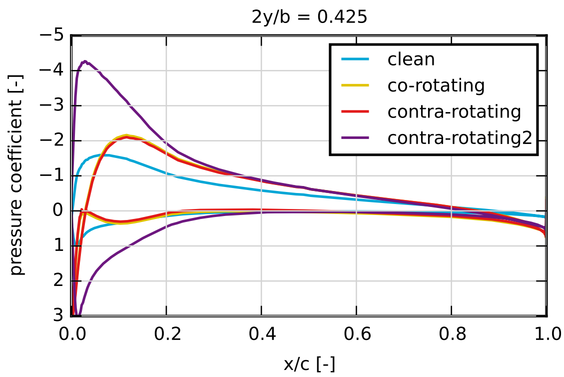

(d) behind blade

Figure 6.12: Wing pressure distributions at center-line of propeller, behind the blade and between two propellers

A look at the local pressure distributions (see Figure 6.12) unveils further differences between the different cases. Between two propellers,the co-rotating case features a slight pronunciation of the surface pressure coefficient. For the counter-rotating propellers this depends on whether the gap is between to down-going or up-going blades, leading to a strong increase/decrease in local lift coefficient respectively. At the propeller centre-line, no significant differences can be observed. Behind the blades, an up-going blade leads to a strong suction peak very close to the leading edge. Behind a down-going blade, the suction peak is only slightly increased but shifted towards the trailing edge.

In a next step, the lifting-line code was used to see the effect on different wing-pitch, propeller number and disk-loading settings. The results are presented in Tables 6.5 to 6.7. The results show that at higher angles of attack, the relative change in lift-coefficient is larger. This is even more the case for the effective lift coefficient due to the higher vertical thrust component. This happens at a constant power consumption.

Table 6.5: Results for angle-of-attack sweep for leading-edge mounted high-lift propellers obtained with lifting-line simulations. Change in lift with respect to isolated wing (propeller rotated with wing around quarter chord line, $T/A = 1000\ \mathrm{N/m^2}$)

α [deg]	C_L [-]	C_D [-]	L/D [-]	$C_{L_{eff}}$ [-]	ΔC_L [%]	$\Delta C_{L_{eff}}$ [%]	P_{shaft} [kW]
0.00	0.409	0.0060	67.9	0.409	+248	+248	351
2.25	0.516	0.0138	37.4	0.550	+51.3	+61.3	352
5.50	1.021	0.0389	26.2	1.104	+53.9	+66.4	351
7.75	1.301	0.0585	22.2	1.416	+55.8	+69.6	350

For the number of propellers, it can be seen that a higher number results in a higher lift augmentation at lower power consumption. However, the effective lift coefficient does not follow this trend because the vertical thrust component is higher for lower propeller counts.

Table 6.6: Results for propeller count sweep for leading-edge mounted high-lift propellers obtained with lifting-line simulations. Change in lift with respect to isolated wing (propeller rotated with wing around quarter chord line, $T/A = 1000\ \mathrm{N/m^2}$)

N_p [-]	C_L [-]	C_D [-]	L/D [-]	$C_{L_{eff}}$ [-]	ΔC_L [%]	$\Delta C_{L_{eff}}$ [%]	P_{shaft} [kW]
12	0.951	0.0367	25.9	1.193	+43.3	+79.8	468
16	1.021	0.0389	26.2	1.104	+53.9	+66.4	351
20	1.111	0.0361	30.8	1.179	+67.4	+77.7	280.6

The propeller loading does not show a linear relationship with the augmented lift or required power but a higher loading leads to a higher lift augmentation at higher power consumption. Doubling the loading leads to a less than doubled lift augmentation at a more than doubled power consumption. Therefore, less loaded propellers are more effective in terms of increase in lift per unit power spent.

Table 6.7: Results for thrust loading sweep for leading-edge mounted high-lift propellers obtained with lifting-line simulations. Change in lift with respect to isolated wing (propeller rotated with wing around quarter chord line, $\alpha = 5.5$ deg

T/A [N/m^2]	C_L [-]	C_D [-]	L/D [-]	$C_{L_{eff}}$ [-]	ΔC_L [%]	$\Delta C_{L_{eff}}$ [%]	P_{shaft} [kW]
500	0.862	0.0273	31.6	0.904	+29.9	+36.2	145
750	0.937	0.0330	28.4	1.000	+41.2	+50.7	240
1000	1.021	0.0389	26.2	1.104	+53.9	+66.4	351

6.2.3. OVER-THE-WING PROPELLERS

An alternative to placing the propellers in front of the leading edge is to place them above the wing. This way, the increase in dynamic pressure over the suction side augments the lift. The fact that the lift augmentation is mainly achieved by increased suction close to the leading edge results in a forward tilting of the resultant force or, in other words, leads to a thrust force counteracting the drag.

Figure 3.5b shows the studied configuration. It is similar to the leading-edge propeller configuration in the preceding section except for a shift in propeller location to different chord-wise locations above the wing. The spacing between the propeller and the wing is 1% of the chord length and the propellers are aligned with the free stream. The propeller disk loading is again set to 1000 $\mathrm{N/m^2}$.

The results for four different chord-wise propeller locations are presented in Table 6.8. A first important observation is that the lift augmentation is higher than for the leading edge-mounted cases. The further the propeller is shifted towards the trailing edge, the higher the lift coefficient. The drag coefficient shows the opposite behaviour and is the smallest for more upstream mounted propellers. Furthermore, the drag coefficient is not only locally negative as for single over-the-wing mounted propeller simulations found in literature but shows a globally negative drag value. The moment coefficient becomes increasingly negative when shifting the propellers downstream. Finally, the required shaft power is smaller for more downstream installed engines.

Table 6.8: Results for over-the-wing mounted high-lift propellers obtained with body-force simulations. Change in lift with respect to isolated wing (propellers aligned with free stream, $\alpha = 5.5$deg, $T/A = 1000$ $\mathrm{N/m^2}$)

x_P/c [-]	C_L [-]	C_D [-]	$C_{M_{y,0.25c}}$ [-]	L/D [-]	ΔC_L [%]	P_{shaft} [kW]
0.2	0.957	-0.0839	-0.0296	-11.4	+54.9	354
0.4	1.094	-0.0680	-0.0315	-16.1	+77.0	352
0.6	1.226	-0.0348	-0.0697	-35.2	+98.4	343
0.8	1.280	-0.0007	-0.1251	-1850	+107.1	333

Table 6.9 shows the results for the same configuration but with half the disc loading of 500 $\mathrm{N/m^2}$. The previously mentioned trends remain but are weakened in magnitude. However, as for the leading-edge mounted propellers, the lift augmentation (and in this case also the drag reduction) reaches more than half with respect to the higher disk loading while requiring less than half the power. This again makes less loaded propellers more effective in augmenting the lift.

Table 6.9: Results for over-the-wing mounted high-lift propellers obtained with body-force simulations. Change in lift with respect to isolated wing (propellers aligned with free stream, $\alpha = 5.5$deg, $T/A = 500$ $\mathrm{N/m^2}$)

x_P/c [-]	C_L [-]	C_D [-]	L/D [-]	ΔC_L [%]	P_{shaft} [kW]
0.2	0.814	-0.0307	-26.5	+31.7	162
0.4	0.899	-0.0250	-35.9	+45.5	161
0.6	0.986	-0.0091	-108.8	+59.5	157
0.8	1.028	0.0080	128.0	+66.3	152

It has been shown that the local lift augmentation, drag reduction and changes in pitching moment as observed by Müller et al. [166] are much stronger for the installation of multiple propellers. The local negative drag is present globally for the analysed case. Furthermore, the lift is increased up to twice its original value depending on the propeller location. The lift distribution is plotted in Figure 6.13 for the different propeller positions. The more downstream installed propellers have higher span-wise lift variations.

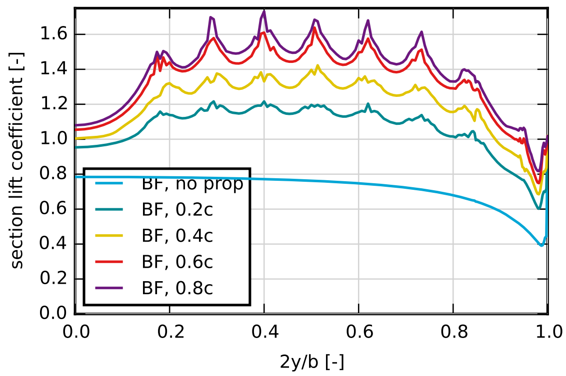

Figure 6.13: Wing lift distribution for installed over-the-wing propellers (propellers aligned with free stream, $\alpha = 5.5$deg, $T/A = 1000$ N/m^2)

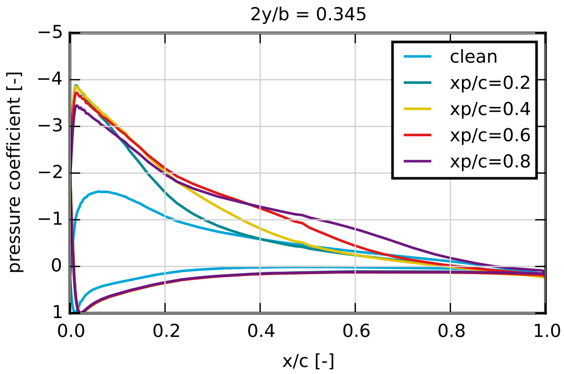

(a) between two propellers

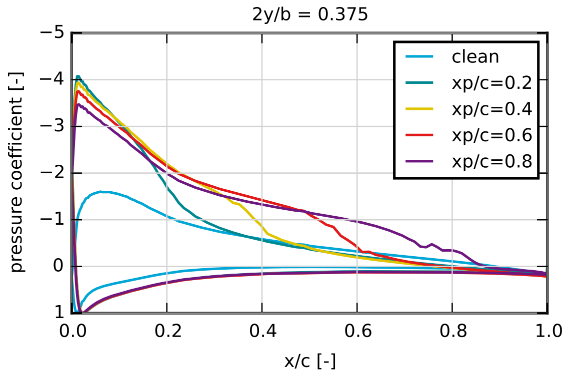

(b) under up-going blade

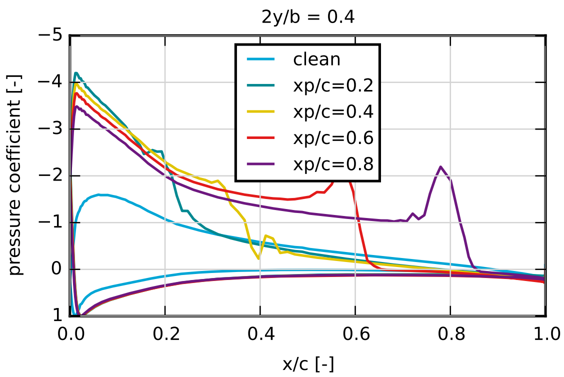

(c) at propeller center-line

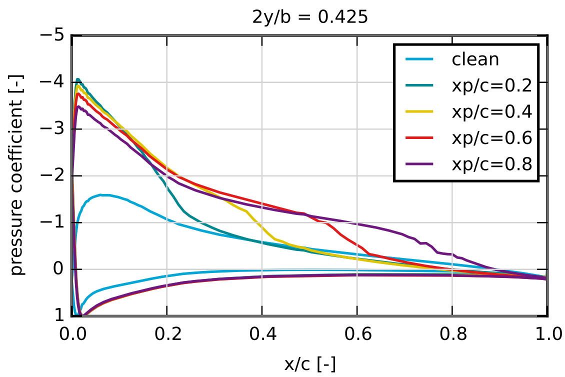

(d) under down-going blade

Figure 6.14: Wing pressure distributions at center-line of over-the-wing propeller and between two propellers (leading-edge pointing downwards, propellers aligned with free stream, $\alpha = 5.5$deg, $T/A = 1000$ N/m^2)

How the strong changes in load coefficients are achieved becomes more clear when looking at sectional pressure distributions as presented in Figure 6.14. Directly between a propeller and a propeller, the pressure jump across the propeller plane is visible on the suction side. The largest difference in pressure distribution compared to the isolated wing occurs on the suction side upstream of the propeller. The more upstream the propeller is located, the stronger the suction peak and the more forward tilts the resultant force vector. Hence, the most upstream mounted propeller leads to the highest drag reduction. On the other hand, the more downstream the propeller is situated, the larger is the surface upstream of the propeller, resulting in a higher lift increment. In between to propellers, the same pressure distribution trend can be observed but the pressure jumps are flattened out where there is a larger gap between the blades and the wing surface. Notably, the distributions at the propeller center-line show wiggles that seem to be the result of imposing body-forces inside the wing boundary layer (also further out-/inboard at backward shifted propeller positions where the boundary layer is thicker). What exactly causes these fluctuations, however, is not clear.

Figures 6.15 shows the axial velocity contours at 40% span for the different propeller positions. Here it becomes clear why the suction at the upper wing surfaceis larger for near trailing-edge mounted propellers. The Further downstream the propeller is installed, the larger is the high-speed region directly over the wing surface.

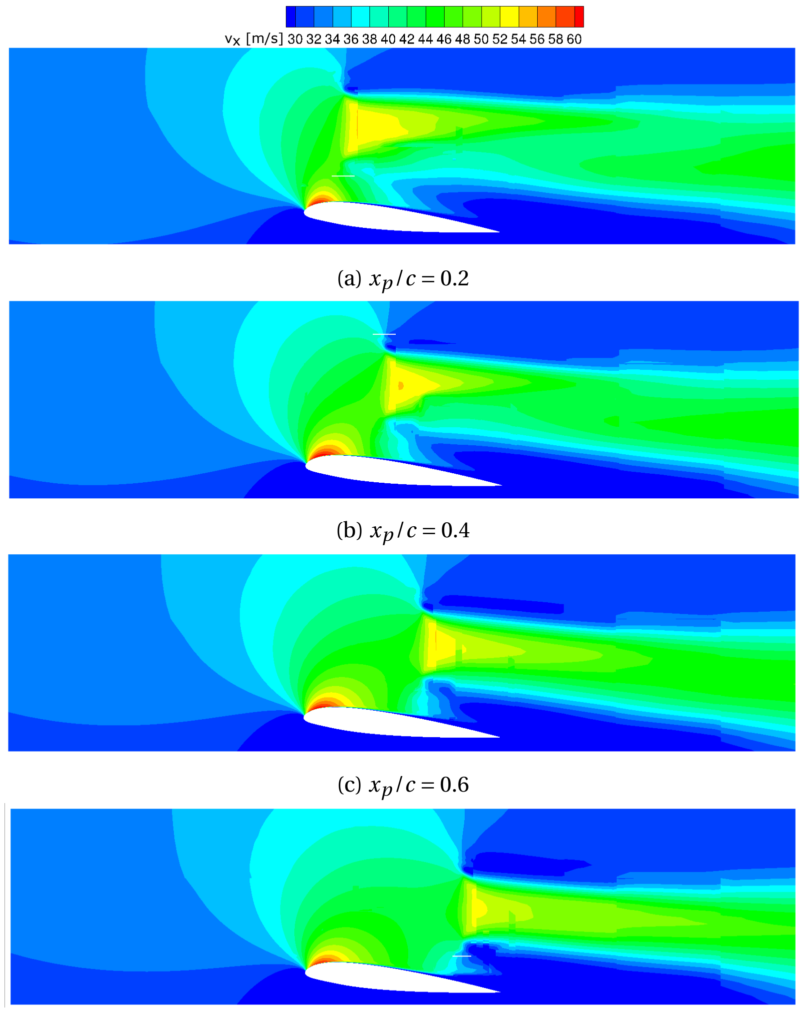

(a) $x_p/c = 0.2$

(b) $x_p/c = 0.4$

(c) $x_p/c = 0.6$

(d) $x_p/c = 0.8$

Figure 6.15: Axial velocity contours at 2y/b=0.4 for different axial propeller positions (v_x in m/s, propellers aligned with free stream, $\alpha = 5.5$deg, $T/A = 1000$ N/m^2)

When looking at the upper wing surface pressure coefficient distributions, it can be seen how the more aft-mounted propellers lead to a higher local variation in pressure distribution. Especially at 80% chord length the propeller seems to interact with the wing boundary layer because the layer extends further than 1% from the wing surface at this position. As a result, it seems that also local trailing-edge separations occur (see also Figure 6.15d).

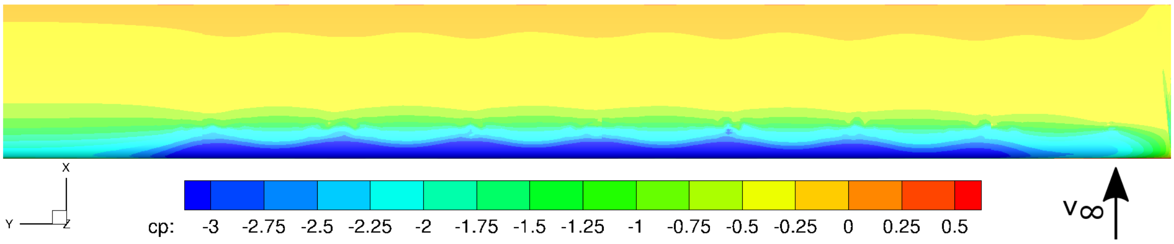

(a) $x_p/c = 0.2$

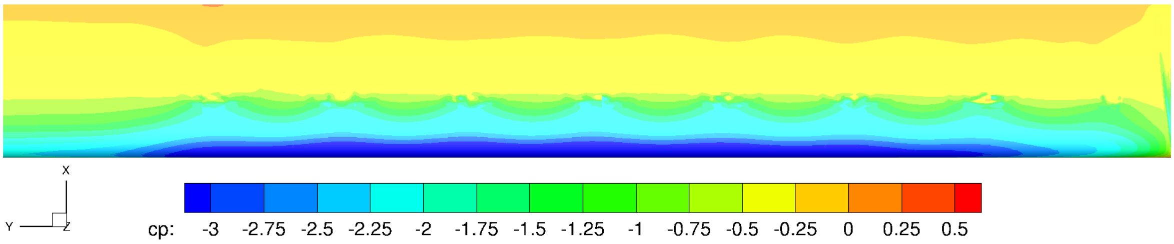

(b) $x_p/c = 0.4$

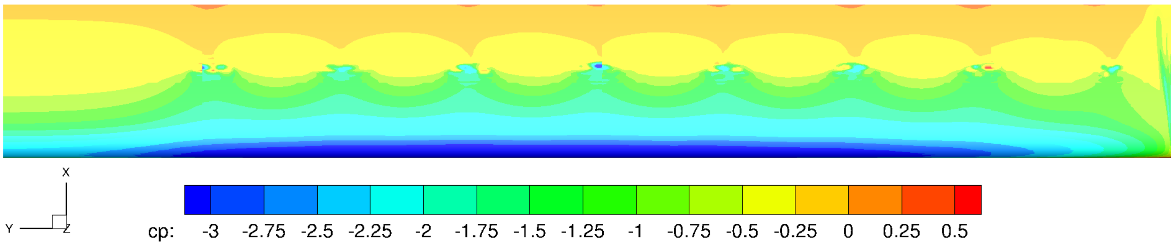

(c) $x_p/c = 0.6$

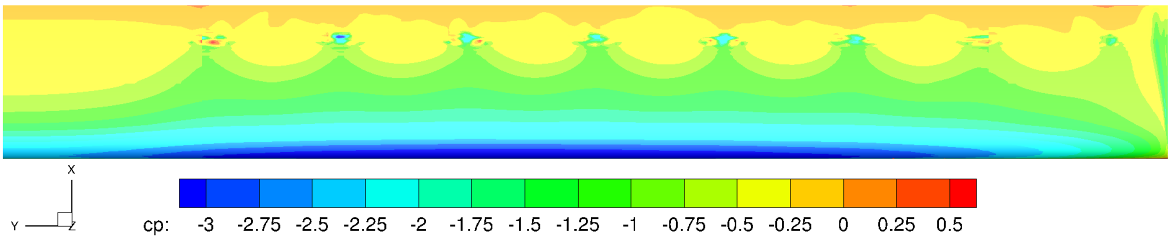

(d) $x_p/c = 0.8$

Figure 6.16: Pressure distribution over the wing upper surface with installed over-the-wing propellers, propellers aligned with free stream, $\alpha = 5.5$deg, $T/A = 1000$ N/m^2)

Finally, the angle-of-attack maps of the propeller at 40% span are shown in Figure 6.17. For the most upstream propeller, a weakly loaded region develops close to the wing. The high induced velocities above the wing leading-edge area cause a decrease in local blade angle of attack. This effect becomes smaller, the further downstream the propeller is mounted. On the other hand, a region of increased local blade angle of attack develops at the upper side of the propeller hub when moving the propeller further downstream because at these locations, the inner blade sees a relatively lower inflow velocity. The outer most part of the blade experiences a rather high angle-of-attack in all cases because the blade-smoothing was not applied in these cases leading to a blade tip with zero chord length and a rather high local pitch.

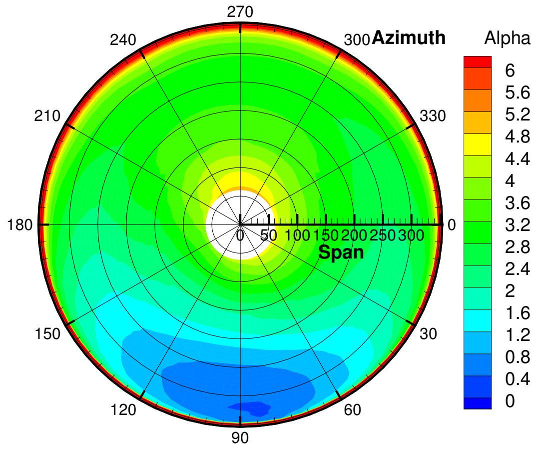

(a) $x_p/c = 0.2$

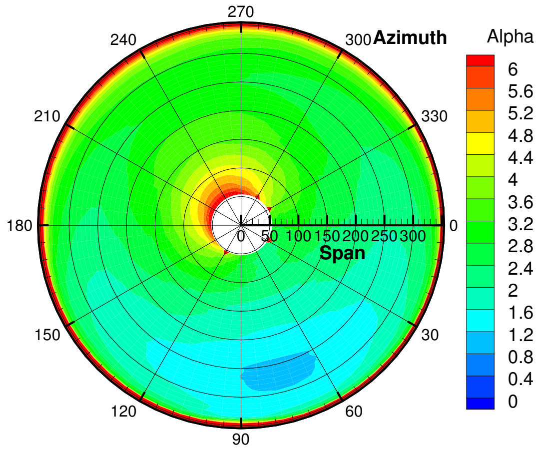

(b) $x_p/c = 0.4$

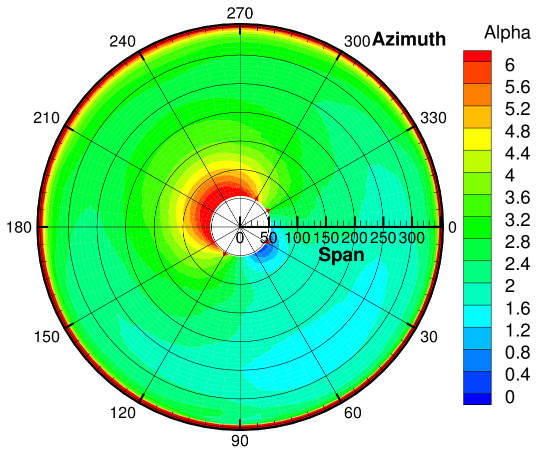

(c) $x_p/c = 0.6$

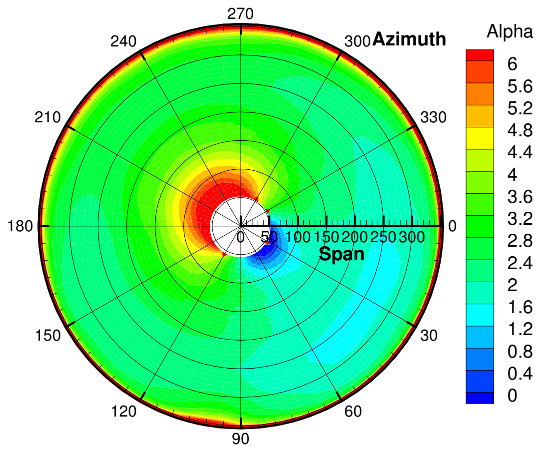

(d) $x_p/c = 0.8$

Figure 6.17: Over-the wing propeller effective angle-of-attack maps for different chord-wise positions (α & Ψ in degrees, b in mm, propellers aligned with free stream, $\alpha_w = 5.5$deg, $T/A = 1000$ N/m^2)

As for the wing-tip mounted propellers, additional results can be found in Appendix B. Presented are wing surface pressure distributions as well as total pressure and axial vorticity contours at different axial distances downstream of the wing.

7

Conclusions & Recommendations

This last chapter is devoted to concluding the previously presented work. First some general conclusions about the implemented method and the analyses are drawn. Subsequently, suggestions for further work are given.

7.1. Conclusions

The literature survey showed that significant aero-propulsive benefits can be achieved by employing distributed propulsion. Improvements in cruise efficiency and high lift capability are two major opportunities pointed out by many publications. While the physical phenomena of propeller-wing interaction are known and have been summarised, the large number of design variables require a large number of simulations to determine how the benefits can best be exploited.

The lack of methods being able to accurately capture all important aerodynamic interactions between distributed propellers and wings at acceptable computational costs motivated the work presented in this report. The introductory chapters outlined why a higher fidelity tool is required to model these interactions and why current alternatives seemed incapable of doing so. The body-force method was proposed to solve this gap and the implementation has been explained in detail. The comparison to meshed-propeller URANS simulations and experimental data showed very good agreement. The two-way interaction was captured in all aspects such that the change in lift and drag on the wing due to the presence of the propeller was correctly predicted. Also the change in propeller efficiency and evolutions in thrust as well as in-plane loads variation was accurately predicted.

In the present analyses, a grid size reduction for the body-force approach with respect to the meshed propeller approach of six million grid points per propeller showed a benefit especially for simulations with many propellers. Design changes for the propeller can be realised directly in the propeller model and do not require re-meshing the configuration. Next to the improved computational and preparatory effort to analyse a configuration with the proposed method, also the direct access to azimuthal thrust and in-plane loads evolutions as well as to engineering variables like blade angle-of-attack or inflow Mach numbers should be pointed out. Finally, the possibility to trim the propellers for a target thrust/shaft power during the simulation is a useful capability of the method.

A limitation of the current work is the absence of a nacelle which has a non-negligible effect on the results of a fully integrated propeller-wing geometry. This was acceptable to study the general flow principles in this work but including the propeller support structure would be of importance for more detailed design studies on specific aircraft architectures. Additionally, it has been seen that the validation for multiple propellers along the leading edge showed an offset between the two different methods caused by the body-force calibration for a highly loaded propeller applied to a weakly loaded propeller, suggesting that the calibration is not suited to model very different operating conditions and needs re-calibration for large changes.

The application of the body-force method to wing-tip mounted propellers showed significant improvements in aero-propulsive efficiency. The wing drag reductions of 10% and the improvements in propulsive efficiency of 8-9% resulted in a significantly reduced required total power. While for a non-twisted wing, the pusher propeller was better capable of benefiting from the interaction, the weaker in-flow swirl of an ideally-twisted wing resulted in the two options being equally efficient. This behaviour, however, cannot be said to be a general rule as the interaction depends on a high number of design variables that could not all be assessed. Still, the large differences in performance suggest that pusher and tractor configurations are not equally well performing contrary to what earlier inviscid analyses suggested. Also other design considerations may play an important role. The pusher cases showed a stronger and more sudden variation in blade loading due to the ingestion of the wing wake. This promotes vibration and noise. The lifting-line code PUMA was additionally shown to be capable of simulating these configurations with less accuracy.

For high-lift propeller-wing configurations, a lift augmentation of more than 107% was achieved by installing over-the-wing propellers. Additionally, strong drag reductions were achieved, especially at chord-wise propeller positions close to the leading edge but at the cost of less lift augmentation. Also leading-edge mounted propellers achieved up to 60% lift improvement. Contra-rotating propellers were found to be more efficient in lift augmentation than co-rotating engines when mounted in front of the wing. A higher number of propellers was shown to result in less required power for a similar or even higher lift augmentation. This was still the case for propellers with diameter-to-chord ratios smaller than one. This is, however, at the cost of increased drag. Weaker loaded propellers were shown to obtain more lift augmentation per unit power. The lifting-line code was shown to capture major trends of such configurations.

7.2. RECOMMENDATIONS

Finally, some recommendations for further work are made in this last section. First some suggestions for further method improvements are made. Secondly, ideas for further exploratory studies on distributed propeller-wing configurations are given. Although the implemented body-force approach has been shown to closely represent the two-way interaction between a wing and propellers, several proposals for improvements can be made.

As a first step, the distribution of the source-terms in blade chord-wise direction may be improved. The implementation of a (semi-)empirical model to estimate the distribution as a function of section loading, radial position and other governing parameters could improve the accuracy compared to the current state where the distribution is kept constant after calibration to one propeller operating condition (also requiring a reference). Also known airfoil pressure distributions may be used to estimate the distribution.

A second step could be adding time resolution. By not applying the time-averaged local source terms but only applying the current source terms at the position of the blade at each time step, the time-varying notion of the flow can be captured with URANS without meshing the blade.

Only a limited number of factors could be assessed during the short project. Therefore, it will be the task of further research to assess the effects of things like propeller inclinations etc. on the configuration.

Also integration issues should be tackled in future studies. While over-the-wing mounted propellers seem an interesting option from the obtained results, the mounting of these propellers may influence the performance significantly. Also the effect of nacelles on the performance of the wing-tip mounted propellers is non-negligible and should be assessed further. Noise generation by many closely coupled propellers undergoing strong variations in loading is an additional problem for future analyses.

Furthermore, the combined effects of lift-augmenting and wing-tip mounted propellers may be different from the isolated cases. It would be interesting to analyse this by comparing identical configurations with isolated wing, only high-lift/wing-tip propellers, and all propellers activated.

Bibliography

[1] D. P. Witkowski, A. K. H. Lee, and J. P. Sullivan, *Aerodynamic Interaction between Propellers and Wings,* Journal of Aircraft **26**, 829 (1989).

[2] C. Pornet, *Electric Drives for Propulsion System of Transport Aircraft,* InTech , 115 (2015).

[3] G. Ameyugo, M. Taylor, and R. Singh, *Distributed Propulsion Feasibility Studies,* 25th International Congress of the Aeronautical Sciences (2006).

[4] A. T. Wick, J. R. Hooker, C. J. Hardin, and C. H. Zeune, *Integrated Aerodynamic Benefits of Distributed Propulsion,* 53rd AIAA Aerospace Sciences Meeting (2015), doi:10.2514/6.2015-1500.

[5] A. K. Sehra and W. Whitlow, *Propulsion and power for 21st century aviation,* Progress in Aerospace Sciences **40**, 199 (2004).

[6] A. Isyanov, A. Lukovnikov, and A. Mirzoyan, *Development challenges of distributive propulsion systems for advanced aeroplanes,* Aircraft Engineering and Aerospace Technology **86**, 459 (2014).

[7] A. S. Gohardani, G. Doulgeris, and R. Singh, *Challenges of future aircraft propulsion: A review of distributed propulsion technology and its potential application for the all electric commercial aircraft,* Progress in Aerospace Sciences **47**, 369 (2011).

[8] H. D. Kim, *Distributed Propulsion Vehicles,* 27th International Congress of the Aeronautical Sciences (2015).

[9] J. L. Felder, H. D. Kim, and G. V. Brown, *Turboelectric Distributed Propulsion Engine Cycle Analysis for Hybrid-Wing-Body Aircraft,* 47th AIAA Aerospace Sciences Meeting including the New Horizons Forum and Aerospace Exposition , AIAA 2009 (2009).

[10] C. E. Jones, P. J. Norman, S. J. Galloway, M. J. Armstrong, and A. M. Bollman, *Future Distributed Propulsion Aircraft,* IEEE Transactions on Applied Superconductivity **26** (2016).

[11] C. Pornet and A. T. Isikveren, *Conceptual design of hybrid-electric transport aircraft,* Progress in Aerospace Sciences **79**, 114 (2015).

[12] A. T. Isikveren, A. Seitz, J. Bijewitz, M. Hornung, A. Mirzoyan, A. Isyanov, J. L. Godard, S. Stückl, and J. van Toor, *Recent Advances in Airframe-Propulsion Concepts with Distributed Propulsion,* 29th Congress of the International Council of the Aerautical Sciences (2014).

[13] A. R. Gibson, D. Hall, M. Waters, B. Schiltgen, T. Foster, J. Keith, and P. Masson, *The Potential and Challenge of TurboElectric Propulsion for Subsonic Transport Aircraft,* 48th AIAA Aerospace Sciences Meeting Including the New Horizons Forum and Aerospace Exposition (2010), doi:10.2514/6.2010-276.

[14] C. M. Lewandowski, *Turboelectric Distributed Propulsion in a Hybrid Wing Body Aircraft,* NASA Technical Report (2011), 10.1017/CBO9781107415324.004, arXiv:arXiv:1011.1669v3 .

[15] D. Nalianda and R. Singh, *Turbo-electric distributed propulsion – opportunities , benefits and challenges,* Aircraft Engineering and Aerospace Technology: An International Journal **86**, 543 (2014).

[16] K. V. Papathakis, K. J. Kloesel, Y. Lin, S. C. Clarke, J. J. Ediger, and S. R. Ginn, *NASA Turbo-electric Distributed Propulsion Bench,* 52nd AIAA/SAE/ASEE Joint Propulsion Conference (2016), 10.2514/6.2016-4611.

[17] H.-J. Steiner, P. C. Vratny, C. Gologan, K. Wieczorek, A. T. Isikveren, and M. Hornung, *Performance and Sizing of Transport Aircraft Employing Electrically-Powered Distributed Propulsion,* Deutscher Luft- und Raumfahrt Kongress 2012, Berlin, Germany (2012).

[18] P. Laskaridis, *Assessment of Distributed Propulsion Systems Used with Different Aircraft Configurations,* 51st AIAA/SAE/ASEE Joint Propulsion Conference (2015), 10.2514/6.2015-4029.

[19] O. Schmitz and M. Hornung, *Unified Applicable Propulsion System Performance Metrics,* Journal of Engineering for Gas Turbines and Power **135** (2013), 10.1115/GT2013-95724.

[20] P. C. Vratny, C. Gologan, C. Pornet, A. T. Isikveren, and M. Hornung, *Battery Pack Modeling Methods for Universally-Electric Aircraft,* 4th CEAS Air & Space Conference (2013), 978-91-7519-519-3.

[21] H. Kuhn, C. Falter, and A. Sizmann, *Renewable Energy Perspectives for Aviation,* Proceedings of the 3rd CEAS Air&Space Conference and 21st AIDAA Congress , 1249 (2011).

[22] C. Liu, E. Valencia, and J. Teng, *Design point analysis of the turbofan-driven turboelectric distributed propulsion system with boundary layer ingestion,* Journal of Aerospace Engineering **230**, 1139 (2016).

[23] H. Dae Kim, J. L. Felder, M. T. Tong, J. J. Berton, and W. J. Haller, *Turboelectric distributed propulsion benefits on the N3-X vehicle,* Aircraft Engineering and Aerospace Technology: An International Journal **86**, 558 (2014).

[24] R. Kirner, *An Investigaion into the Benefits of Distributed Propulsion on Advanced Aircraft Configurations,* Dissertation at Cranfield University (2013).

[25] H. D. Kim, J. L. Felder, M. T. Tong, and M. J. Armstrong, *Revolutionary Aeropropulsion Concept for Sustainable Aviation: Turboelectric Distributed Propulsion,* 21st International Symposium on Air Breathing Engines (ISABE) (2013).

[26] A. Ko, J. A. Schetz, and W. H. Mason, *Assessment of the Potential Advantages of Distributed-Propulsion for Aircraft,* ISABE (2003).

[27] H. Smith, *Airframe integration for an LH2 hybrid-electric propulsion system,* Aircraft Engineering and Aerospace Technology: An International Journal **86**, 562 (2014).

[28] C. Liu, *Turboelectric Distributed Propulsion System Modelling,* Dissertation at Cranfield University (2013).

[29] A. Seitz, J. Bijewitz, S. Kaiser, G. Wortmann, A. Seitz, J. Bijewitz, S. Kaiser, and G. Wortmann, *Conceptual investigation of a propulsive fuselage aircraft layout,* Aircraft Engineering and Aerospace Technology: An International Journal **86**, 464 (2014).

[30] A. Ko, L. T. Leifsson, J. A. Schetz, W. H. Mason, B. Grossman, and R. T. Haftka, *MDO of a Blended-Wing-Body Transport Aircraft with Distributed Propulsion,* AIAA's 3rd Annual Aviation Technology, Integration, and Operations (ATIO) Technical Forum (2003), doi:10.2514/6.2003-6732.

[31] J. S. Attinello, *The jet wing,* IAS 25th Annual Meeting (1957).

[32] J. N. Walker, *Numerical Studies of Jet-Wing Distributed Propulsion and a Simplified Trailing Edge Noise Metric Method,* Thesis at Virginia Polytechnic Institute and State University (2004).

[33] J. A. Schetz, S. Hosder, V. F. Dippold, and J. N. Walker, *Propulsion and aerodynamic performance evaluation of jet-wing distributed propulsion,* Aerospace Science and Technology **14**, 1 (2010).

[34] V. F. Dippold, S. Hosder, and J. a. Schetz, *Analysis of Jet-Wing Distributed Propulsion from Thick Wing Trailing Edges,* 42nd AIAA Aerospace Sciences Meeting and Exhibit (2004), 10.2514/6.2004-1205.

[35] J. P. Hancock, *Test of a high efficiency transverse fan,* AIAA/SAE/ASME 16th Joint Propulsion Conference (1980).

[36] C. Gologan, S. Mores, H.-J. Steiner, and A. Seitz, *Potential of the Cross-Flow Fan for Powered-Lift Regional Aircraft Applications,* 9th AIAA Aviation Technology Integration, and Operations Conference (2009).

[37] G. R. Seyfang, *FanWing - Developments and Applications,* 28th International Congress of the Aeronautical Sciences , 1 (2012).

[38] G. Paniagua, J. Gibbs, A. Bachmann, G. R. Seyfang, P. Peebles, and C. May, *An open-rotor distributed propulsion aircraft study,* Deutscher Luft- und Raumfahrtkongress 2016 (2016).

[39] N. K. Borer, M. D. Patterson, J. K. Viken, M. D. Moore, S. C. Clarke, M. E. Redifer, R. J. Christie, A. M. Stoll, A. Dubois, J. Bevirt, A. R. Gibson, T. J. Foster, and P. G. Osterkamp, *Design and Performance of the NASA SCEPTOR Distributed Electric Propulsion Flight Demonstrator,* 16th AIAA Aviation Technology, Integration, and Operations Conference (2016), 10.2514/6.2016-3920.

[40] A. M. Stoll, E. V. Stilson, J. Bevirt, and P. P. Pei, *Conceptual Design of the Joby S2 Electric VTOL PAV,* 14th AIAA Aviation Technology, Integration, and Operations Conference (2014), 10.2514/6.2014-2407.

[41] M. D. Moore and B. Fredericks, *Misconceptions of Electric Aircraft and their Emerging Aviation Markets,* 52nd Aerospace Sciences Meeting (2014), 10.2514/6.2014-0535.

[42] M. D. Patterson, B. J. German, and M. D. Moore, *Performance Analysis and Design of On-Demand Electric Aircraft Concepts,* 12th AIAA Aviantion Technology, Integration, and Operations (ATIO) Conference and 14th AIAA/ISSM (2012), 10.2514/6.2012-5474.

[43] R. Lyasoff, *Welcome to Vahana,* (2017), URL: `https://vahana.aero/welcome-to-vahana-edfa689f2b75`, online, accessed April 5, 2017.

[44] G. K. Ananda, R. W. Deters, and M. S. Selig, *Propeller Induced Flow Effects on Wings at Low Reynolds Numbers,* 31st AIAA Applied Aerodynamics Conference (2013).

[45] R. H. Stone, *Aerodynamic Modeling of the Wing-Propeller Interaction for a Tail-Sitter Unmanned Air Vehicle,* Journal of Aircraft **45**, 198 (2008).

[46] A. Johanning and D. Scholz, *Novel Low-Flying Prpoeller-Driven Aircraft Concept for Reduced Operating Costs and Emissions,* 28th International Congress of the Aeronautical Sciences , 1 (2012).

[47] A. T. Isikveren, A. Seitz, J. Bijewitz, A. Mirzoyan, A. Isyanov, R. Grenon, O. Atinault, J. L. Godard, and S. Stückl, *Distributed propulsion and ultra-high by-pass rotor study at aircraft level,* The Aeronautical Journal **119** (2015).

[48] R. Kirner, L. Raffaelli, A. Rolt, P. Laskaridis, G. Doulgeris, and R. Singh, *An assessment of distributed propulsion : Advanced propulsion system architectures for conventional aircraft configurations,* Aerospace Science and Technology **46**, 42 (2015).

[49] A. M. Stoll, *Comparison of CFD and Experimental Results of the LEAPTech Distributed Electric Propulsion Blown Wing,* 15th AIAA Aviation Technology, Integration, and Operations Conference (2015), 10.2514/6.2015-3188.

[50] K. Davies, P. J. Norman, C. Jones, S. J. Galloway, and M. Husband, *A Review of Turboelectric Distributed Propulsion Technologies for N + 3 Aircraft Electrical Systems,* 48th International Universities' Power Engineering Conference (2013).

[51] Advisory Council for Aviation Research and Innovation in Europe, *FlightPath 2050 Goals,* (2012), URL: `http://www.acare4europe.org/sria/flightpath-2050-goals`, online, accessed April 5, 2017.

[52] E. M. Greitzer, P. A. Bonnefoy, E. DelaRosaBlanco, C. S. Dorbian, M. Drela, D. K. Hall, R. J. Hansman, J. I. Hileman, R. H. Liebeck, J. Levegren, P. Mody, J. A. Pertuze, S. Sato, Z. S. Spakovszky, C. S. Tan, J. S. Hollman, J. E. Duda, N. Fitzgerald, J. Houghton, J. L. Kerrebrock, G. F. Kiwada, D. Kordonowy, J. C. Parrish, J. Tylko, and E. A. Wen, *N+3 Aircraft Concept Designs and Trade Studies. Volume 1,* NASA Technical Report (2010).

[53] A. Seitz, O. Schmitz, A. Isikveren, and M. Hornung, *Electrically Powered Propulsion: Comparison and Contrast to Gas Turbines,* Deutscher Luft- und Raumfahrtkongress (2012).

[54] B. Schiltgen, M. Green, and A. Gibson, *Analysis of Terminal Area Operations and Short Field Performance of Hybrid Electric Distributed Propulsion,* AIAA Aviation 2013 (2013), doi:10.2514/6.2013-4265.

[55] H.-J. Steiner, P. C. Vratny, C. Gologan, K. Wieczorek, A. T. Isikveren, and M. Hornung, *Optimum number of engines for transport aircraft employing electrically powered distributed propulsion,* CEAS Aeronautical Journal **5**, 157 (2014).

[56] A. S. Gohardani, *A Synergetic Glance at the Prospects of Distributed Propulsion Technology and the Electrical Aircraft Concept for Future Unmanned Air Vehicles and Commercial/Military Aviation,* Progress in Aerospace Sciences **57**, 25 (2013).

[57] A. M. Stoll, J. Bevirt, M. D. Moore, W. J. Fredericks, and N. K. Borer, *Drag Reduction Through Distributed Electric Propulsion,* 14th AIAA Aviation Technology, Integration, and Operations Conference (2014), 10.2514/6.2014-2851.

[58] M. D. Patterson, M. J. Daskilewicz, and B. J. German, *Conceptual Design of Electric Aircraft with Distributed Propellers : Multidisciplinary Analysis Needs and Aerodynamic Modeling Development,* 52nd Aerospace Sciences Meeting (2014), 10.2514/6.2014-0534.

[59] A. A. Candade, *Thesis at Delft University of Technology,* Master thesis, TU Delft (2015).

[60] A. M. Stoll and G. Veble Mikic, *Design Studies of Thin-Haul Commuter Aircraft with Distributed Electric Propulsion,* 16th AIAA Aviation Technology, Integration, and Operations Conference (2016), 10.2514/6.2016-3765.

[61] J. Posey, A. Tinetti, and M. Dunn, *The Low-Noise Potential of Distributed Propulsion on a Catamaran Aircraft,* 12th AIAA/CEAS Aeroacoustics Conference (27th AIAA Aeroacoustics Conference) (2006), 10.2514/6.2006-2622.

[62] J. Hileman, Z. Spakovszky, M. Drela, and M. Sargeant, *Airframe Design for "Silent Aircraft",* 45th AIAA Aerospace Sciences Meeting and Exhibit (2007), 10.2514/6.2007-453.

[63] S. Bruner, S. Baber, C. Harris, N. Caldwell, P. Keding, K. Rahrig, L. Pho, and R. Wlezian, *NASA N + 3 Subsonic Fixed Wing Silent Ef fi cient Low-Emissions Commercial Transport (SELECT) Vehicle Study Revision A,* NASA Technical Report 2010-216798 (2010).

[64] P. J. Masson, G. V. Brown, D. S. Soban, and C. A. Luongo, *HTS machines as enabling technology for all-electric airborne vehicles,* Superconductor Science and Technology **20**, 748 (2007).

[65] M. D. Moore, K. Goodrich, J. Viken, J. Smith, B. Fredericks, T. Trani, J. Barraclough, B. J. German, and M. D. Patterson, *High-Speed Mobility through On-Demand Aviation,* Aviation Technology, Integration, and Operations Conference (2013).

[66] A. Lundbladh and T. Grönstedt, *Distributed Propulsion and Turbofan Scale Effects,* 17th Symposium on Airbreathing Engines (2005).

[67] J. C. Shaw, S. D. A. Fletcher, P. J. Norman, and S. J. Galloway, *More electric power system concepts for an environmentally responsible aircraft (N+2),* Proceedings of the Universities Power Engineering Conference (2012), 10.1109/UPEC.2012.6398668.

[68] M. W. Green, B. T. Schiltgen, and A. R. Gibson, *Analysis of a Distributed Hybrid Propulsion System with Conventional Electric Machines,* 48th AIAA/ASME/SAE/ASEE Joint Propulsion Conference and Exhibit (2012), 10.2514/6.2012-3768.

[69] K. Reynolds, N. T. Nguyen, E. Ting, and J. Urnes Sr, *Wing shaping concepts using distributed propulsion,* Aircraft Engineering and Aerospace Technology: An International Journal **86**, 478 (2014).

[70] J. Freeman, P. Osterkamp, M. Green, A. Gibson, and B. Schiltgen, *Challenges and opportunities for electric aircraft thermal management,* Aircraft Engineering and Aerospace Technology **86**, 519 (2014).

[71] a. F. Haglind and R. Hasselrot, *Potential of reducing the environmental impact of aviation by using hydrogen Part I : Background , prospects and challenges Intergovernmental Panel on Cimate Change,* The Aeronautical Journal **110**, 533 (2006).

[72] C. A. Snyder, J. J. Berton, G. V. Brown, J. L. Dolce, N. V. Dravid, D. J. Eichenberg, J. E. Freeh, C. A. Gallo, S. M. Jones, K. P. Kundu, C. J. Marek, M. G. Millis, P. L. Murthy, T. M. Roach, and R. T. Tornabene, *Propulsion Investigation for Zero and Near-Zero Emissions Aircraft,* NASA Technical Report (2009).

[73] J. D. Anderson Jr., *Fundamentals of Aerodynamics*, 5th ed. (McGraw-Hill, Inc., 2011).

[74] T. Burton, D. Sharpe, N. Jenkins, and E. Bossanyi, *Wind Energy Handbook*, 1st ed. (John Wiley & Sons, ltd, 2001).

[75] A. Betz and L. Prandtl, *Schraubenpropeller mit geringstem Energieverlust,* Nachrichten von der Gesellschaft der Wissenschaften zu Göttingen, Mathematisch-Physikalische Klasse **2**, 193 (1919).

[76] L. Prandtl, *Mutual Influence of Wings and Propeller,* The First Report of the Goettingen Aerodynamic Laboratory, Chapter 4, Section 6 (1921).

[77] Q. R. Wald, *The aerodynamics of propellers,* Progress in Aerospace Sciences **42**, 85 (2006).

[78] L. L. M. Veldhuis, *Propeller wing aerodynamic interference,* Dissertation at Delft University of Technology (2005).

[79] S. Goldstein, *On the Vortex Theory of Screw Propellers,* Proceedings of the Royal Society of London. Series A, Containing Papers of a Mathematical and Physical Character **123**, 440 (1929).

[80] E. E. Larrabee, SAE Technical Paper 790585 (1979).

[81] C. N. Adkins and R. H. Liebeck, *Design of Optimum Propellers,* Journal of Propulsion and Power **10**, 676 (1994).

[82] F. M. Catalano, *On the Effects of an Installed Propeller Slipstream on Wing Aerodynamic Characteristics,* Acta Polytecnica **44** (2004).

[83] L. L. M. Veldhuis, E. van Berkel, M. Kotsonis, and G. Eitelberg, *Non-Uniform Inflow Effects on Propeller Performance,* 31st AIAA Applied Aerodynamics Conference (2013), 10.2514/6.2013-2801.

[84] L. L. M. Veldhuis, T. Stockermans, T. Sinnige, and G. Eitelberg, *Analysis of Swirl Recovery Vanes for Increased Propulsive Efficiency in Tractor Propeller Aircraft,* 30th Congress of the International Council of the Aeronautical Sciences (2016).

[85] I. Kroo, *Propeller-Wing Integration for Minimum Induced Loss,* Journal of Aircraft **23**, 561 (1986).

[86] L. R. Miranda and J. E. Brennan, *Aerodynamic effects of wing-tip mounted propellers and turbines,* 4th AIAA Applied Aerodynamics Conference **86-1802**, 221 (1986).

[87] L. L. M. Veldhuis, *Review of Propeller-Wing Aerodynamic Interference,* 24th International Congress of the Aeronautical Sciences (2004).

[88] M. D. Patterson and B. J. German, *Wing Aerodynamic Analysis Incorporating One-Way Interaction with Distributed Propellers,* 14th AIAA Aviation Technology, Integration, and Operations Conference (2014), 10.2514/6.2014-2852.

[89] J. C. Patterson and G. R. Bartlett, *Evaluation of installed performance of a wing-tip-mounted pusher turboprop on a semispan wing,* NASA Technical Report 2739 (1987).

[90] M. H. Snyder Jr. and G. W. Zumwalt, *Effects of Wingtip-Mounted Propellers on Wing Lift and Induced Drag,* Journal of Aircraft **6**, 392 (1969).

[91] J. L. Loth and F. Loth, *Induced drag reduction with wing tip mounted propellers,* AIAA 2nd Applied Aerodynamics Conference (1984), 10.2514/6.1984-2149.

[92] D. P. Witkowski, R. T. Johnston, and J. P. Sullivan, *Propeller/wing interaction,* 27th Aerospace Sciences Meeting (1989), 10.2514/6.1989-535.

[93] A. D. Thom, *Analysis of Vortex-Lifting Surface Interactions,* Dissertation at University of Glasgow (2011).

[94] L. L. M. Veldhuis and P. M. Heyma, *Aerodynamic optimisation of wings in multi-engined tractor propeller arrangements,* Aircraft Design **3**, 129 (2000).

[95] M. D. Patterson and B. J. German, *Simplified Aerodynamics Models to Predict the Effects of Upstream Propellers on Wing Lift,* 53rd AIAA Aerospace Sciences Meeting (2015), 10.2514/6.2015-1673.

[96] M. George and E. Kisielowski, *Investigation of Propeller Slipstream Effects on Wing Performance,* NASA (USAAVLABS) Technical Report 67 (1967).

[97] N. T. Nguyen, M. Field, K. Reynolds, M. Field, E. Ting, S. G. Technologies, M. Field, N. Nguyen, and M. Field, *Wing Shaping Distributed Propulsion Aircraft Concept for Improved Aerodynamic Efficiency,* 34th AIAA Applied Aerodynamics Conference (2016), 10.2514/6.2016-3413.

[98] N. K. Borer, M. D. Moore, and A. Turnbull, *Tradespace Exploration of Distributed Propulsors for Advanced On-Demand Mobility Concepts,* 14th AIAA Aviation Technology, Integration, and Operations Conference (2014), 10.2514/6.2014-2850.

[99] A. M. Stoll, J. Bevirt, M. D. Moore, W. J. Fredericks, and N. K. Borer, *Drag Reduction Through Distributed Electric Propulsion,* 14th AIAA Aviation Technology, Integration, and Operations Conference (2014).

[100] R. E. Kuhn and J. W. Draper, *Investigation of the Aerodynamic Characteristics of a Model Wing-Propeller Combination and of the Wing and Propeller Separately At Angles of Attack Up To 90 Degree,* NACA Report 1263 (1956).

[101] D. Reckzeh, *Aerodynamic Design og the A400M High-Lift System,* 26th international congress of the Aeronautical Sciences (2008).

[102] L. Ting, C. H. Liu, and G. Kleinstein, *Interference of Wing and Multipropellers,* AIAA Journal **10**, 906 (1972).

[103] J. Yin, A. Stuermer, and M. Aversano, *Coupled uRANS and FW-H Analysis of Installed Pusher Propeller Aircraft Congurations,* 15th AIAA/CEAS Aeroacoustics Conference (2009), 10.2514/6.2009-3332.

[104] L. Müller, D. Kozulovic, M. Hepperle, and R. Radespiel, *Installation Effects of a Propeller Over a Wing with Internally Blown Flap,* 30th AIAA Applied Aerodynamics Conference (2012), 10.2514/6.2012-3335.

[105] N. K. Borer and M. D. Moore, *Integrated Propeller - Wing Design Exploration for Distributed Propulsion Concepts,* 53rd AIAA Aerospace Sciences Meeting (2015), doi:10.2514/6.2015-1672.

[106] S. An, *Aeroelastic Design of a Leightweight Distributed Electric Propulsion Aircraft with Flutter and Strength Requirements,* Thesis at Georgia Institute of Technology (2015).

[107] M. D. Patterson and N. K. Borer, *A Simple Method for High-Lift Propeller Conceptual Design,* 54th AIAA Aerospace Sciences Meeting (2016), 10.2514/6.2016-0770.

[108] M. D. Patterson, J. M. Derlaga, and N. K. Borer, *High-Lift Propeller System Configuration Selection for NASA ' s SCEPTOR Distributed Electric Propulsion Flight Demonstrator,* 16th AIAA Aviation Technology, Integration, and Operations Conference (2016), 10.2514/6.2016-3922.

[109] W. Fu, J. Li, and H. Wang, *Numerical simulation of propeller slipstream effect on a propeller-driven unmanned aerial vehicle,* Procedia Engineering **31**, 150 (2012).

[110] J. C. Patterson and S. G. Flechner, *An exploratory wind-tunnel investigation of the wake effect of a panel tip-mounted fan-jet engine on the lift-induced vortex,* NASA Technical Note D-5729 (1970).

[111] J. C. Patterson and G. R. Bartlett, *Effect of a Wing-Tip Mounted Pusher Turboprop on the Aerodynamic Characteristics of a Semi-Span Wing,* AIAA/SAE/ASME/ASEE 21st Joint Propulsion Conference (1985), 10.1017/CBO9781107415324.004, arXiv:arXiv:1011.1669v3 .

[112] M. Dimchev, *Experimental and numerical study on wingtip mounted propellers for low aspect ratio UAV design,* Thesis at Delft University of Technology (2012).

[113] N. K. Borer, J. M. Derlaga, K. A. Deere, M. B. Carter, S. A. Viken, M. D. Patterson, B. L. Litherland, and A. M. Stoll, *Comparison of Aero - Propulsive Performance Predictions for Distributed Propulsion Configurations,* 55th AIAA Aerospace Sciences Meeting (2017), 10.2514/6.2017-0209.

[114] M. O. L. Hansen, J. N. Sørensen, S. Voutsinas, N. Sørensen, and H. A. Madsen, *State of the art in wind turbine aerodynamics and aeroelasticity,* Progress in Aerospace Sciences **42**, 285 (2006).

[115] P. Lötstedt, *A propeller slipstream model in subsonic linearized potential flow,* ICAS (1990).

[116] A. S. Aljabri, *The Prediction of Propeller/Wing Interaction Effects,* ICAS (1982).

[117] L. Prandtl, *Applications of Modern Hydrodynamics to Aeronautics,* NASA Technical Report (1923).

[118] J. Weissinger, *The Lift Distribution of Swept-Back Wings,* NACA Report 1120 (1947).

[119] J. Katz and A. Plotkin, *Low-Speed Aerodynamics: From Wing Theory to Panel Methods* (McGraw-Hill, Inc., 1991).

[120] L. Miranda and R. Elliot, *A generalized vortex lattice method for subsonic and supersonic flow applications,* NASA Technical Report (1977).

[121] J. J. Bertin and R. M. Cummings, *Aerodynamics for Engineers*, sixth ed. (Pearson, 2014).

[122] J. Cho and J. Cho, *Quasi-Steady Aerodynamic Analysis of Propeller – Wing Interaction,* International Journal for Numerical Methods in Fluids **1042**, 1027 (1999).

[123] T. Theodorsen, *Theory of Propellers* (McGraw-Hill Book Company, 1948).

[124] D. Clark and A. C. Leiper, *The Free Wake Analysis a Method for The Prediction of Helicopter Rotor Hovering Performance,* Journal of the American Helicopter Society **15**, 3 (1970).

[125] A. B. Phillips, S. R. Turnock, and M. E. Furlong, *Evaluation of manoeuvring coefficients of a self-propelled ship using a blade element momentum propeller model coupled to a Reynolds averaged Navier Stokes flow solver,* Ocean Engineering **36**, 1217 (2009).

[126] O. Gur and A. Rosen, *Comparison between blade-element models of propellers,* Aeronautical Journal **112**, 689 (2008).

[127] J. M. Janus, A. Chatterjee, and C. Cave, *Computational analysis of a wingtip-mounted pusher turboprop,* Journal of Aircraft **33**, 441 (1996).

[128] E. W. M. Roosenboom, A. Stürmer, and A. Schröder, *Advanced Experimental and Numerical Validation and Analysis of Propeller Slipstream Flows,* Journal of Aircraft **47**, 284 (2010).

[129] A. Jameson, *Preliminary Investigation of the Lift of a Wing in an Elliptic Slipstream,* Grumman Aerodynamics Report (1968).

[130] A. Jameson, *Analysis of Wing Slipstream Flow Interaction,* NASA Technical Report (1970).

[131] M. a. Mcveigh, L. Gray, and E. Kisielowski, *Prediction of span loading of straight-wing/propeller combinations up to stall,* NASA Contractor Report (1975).

[132] R. M. Ardito Marretta, G. Davi, G. Lombardi, and A. Milazzo, *Hybrid numerical technique for evaluating wing aerodynamic loading with propeller interference,* Computers & Fluids **28**, 923 (1999).

[133] R. M. Ardito Marretta, *Different Wings Flowfields Interaction on the Wing-Propeller Coupling,* Journal of Aircraft **34**, 740 (1997).

[134] D. Hunsaker and D. Snyder, *A Lifting-Line Approach to Estimating Propeller/Wing Interactions,* 24th AIAA Applied Aerodynamics Conference (2006), 10.2514/6.2006-3466.

[135] J. Calabretta, *A Three Dimensional Vortex Particle-Panel Code for Modeling Propeller-Airframe Interaction,* Thesis at California Polytechnic State University (2010).

[136] D. J. Willis, *An Unsteady, Accelerated, High Order Panel Method with Vortex ParticleWakes,* Dissertation at MIT (2006), 10.1109/RE.2006.31.

[137] G. Ferraro, T. Kipouros, M. Savill, A. Rampurawala, and C. Agostinelli, *Propeller-Wing Interaction Prediction for Early Design,* AIAA SciTech 52nd Aerospace Science Meeting (2014), 10.2514/6.2014-0564.

[138] C. Alba, *A Surrogate-Based Multi-Disciplinary Design Optimization Framework Exploiting Wing- Propeller Interaction,* Thesis at Delft University of Technology (2017).

[139] W. Du, S. A. Kinnas, R. M. Mendes, and T. Le Quere, *RANS / Lifting Line Model Interaction Method for the Design of Ducted Propellers and Tidal Turbines,* 22nd Offshore Symposium (2017).

[140] M. Lino, *Numerical investigation of propeller-wing interaction effects for a large military transport aircraft,* Thesis at Delft University of Technology (2010).

[141] J. A. Sparenberg, *On the Linear Theory of an Actuator Disk in a Viscous Fluid,* Journal of Ship Research **18**, 16 (1974).

[142] J. A. Schetz and S. Favin, *Numerical Solution for the Near Wake of a Body with Propeller,* Journal of Hydronautics **11**, 136 (1977).

[143] J. A. Schetz and S. Favin, *Numerical Solution of a Body-Propeller Combination Flow including Swirl and Comparison with Data,* Journal of Hydronautics **13**, 46 (1979).

[144] D. L. Whitfield and A. Jameson, *Three-Dimensional Euler Equation Simulation of Propeller-Wing Interaction in Transonic Flow,* AIAA 21st Aerospace Sciences Meeting (1983), 10.2514/6.1983-236.

[145] F. Stern, H. Kim, V. Patel, and H. Chen, *A Viscous-Flow Approach to the Computation of Propeller-Hull Interaction,* Journal of Ship Research **32**, 246 (1988).

[146] F. Stern and H. Kim, *Computation of Viscous Flow around a Propeller-Shaft Configuration with Inifinite-Pitch Rectangular Blades,* 5th International Conference on Numerical Ship Hydrodynamics (1990).

[147] I. Zawadzki, D. Fuhs, and J. Gorski, *Integration of a Viscous Flow RANS Solver with an Unsteady Propulsor Force Code,* Carderock Division, Naval Surface Warfare Center (1997).

[148] Q. Gao, W. Jin, and D. Vassalos, *The Calculations of Propeller Induced Velocity by RANS and Momentum Theory,* Journal of Marine Science and Application **11**, 164 (2012).

[149] M. Rotte, *Analysis of a Hybrid RaNS-BEM Method for Predicting Ship Power,* Thesis at Delft University of Technology (2015).

[150] A. Sánchez-Caja, J. Martio, I. Saisto, and T. Siikonen, *On the enhancement of coupling potential flow models to RANS solvers for the prediction of propeller effective wakes,* Journal of Marine Science and Technology (Japan) **20**, 104 (2015).

[151] D. Rijpkema, B. Starke, and J. Bosschers, *Numerical simulation of propeller-hull interaction and determination of the effective wake field using a hybrid RANS-BEM approach,* 3rd International Symposium on Marine Propulsors , 421 (2013).

[152] M. Greve, *Non-Viscous Calculation of Propeller Forces under Consideration of Free Surface Effects,* Dissertation at Technische Universität Hamburg-Harburg (2015).

[153] C. D. Simonsen and F. Stern, *RANS Maneuvering Simulation of Esso Osaka With Rudder and a Body-Force Propeller,* Journal of Ship Research **49**, 98 (2005).

[154] J. Bosschers, G. Vaz, A. R. Starke, and E. van Wijngaarden, *Computational Analysis of Propeller Sheet Cavitation and Propeller-Ship Interactopm,* Marine CFD conference Rina (2008).

[155] C. Rong, L. Qiushi, P. Tianyu, and Z. Jian, *Streamwise-body-force-model for rapid simulation combining internal and external flow fields,* Chinese Journal of Aeronautics **29**, 1205 (2016).

[156] S. A. Chadha, B. W. Pomeroy, and M. S. Selig, *Computational Study of a Lifting Surface in Propeller Slipstreams,* 34th AIAA Applied Aerodynamics Conference (2016), 10.2514/6.2016-3132.

[157] B. Starke and J. Bosschers, *Analysis of scale effects in ship powering performance using a hybrid RANS-BEM approach,* 29th Symposium on Naval Hydrodynamics , 26 (2012).

[158] K. Wöckner-Kluwe, *Evaluation of the Unsteady Propeller Performance behind Ships in Waves,* Thesis at Technische Universität Hamburg-Harburg (2013).

[159] W. F. Phillips, S. R. Fugal, and R. E. Spall, *Minimizing Induced Drag with Wing Twist, Computational-Fluid-Dynamics Validation,* Journal of Aircraft **43**, 437 (2006).

[160] L. Cambier, S. Heib, and S. Plot, *The Onera elsA CFD Software : input from research and feedback from industry,* Mechanics & Industry **14**, 159 (2013).

[161] C. Benoit, S. Péron, and S. Landier, *Cassiopee: A CFD pre- and post-processing tool,* Aerospace Science and Technology **45**, 272 (2015).

[162] N. L. Johnson, S. Kotz, and N. Balakrishnan, *Continuous Univariate Distributions*, Vol. Volume 1 (Wiley, New York, 1995) Chap. 21.

[163] J. Jeong and F. Hussain, *On the identification of a vortex,* Journal of Fluid Mechanics **285**, 69 (1995).

[164] P. Marcus, *Rapid numerical modeling of over-the-wing propeller aerodynamics,* (2017).

[165] L. Veldhuis, D. Jansen, J. El Haddar, and G. Correale, *Novel Passive and Active Flow Control for High Lift,* 28th International Congress of the Aeronautical Sciences (2012).

[166] L. Müller, W. Heinze, D. Kožulović, M. Hepperle, and R. Radespiel, *Aerodynamic Installation Effects of an Over-the-Wing Propeller on a High-Lift Configuration,* Journal of Aircraft **51**, 249 (2014).

A

Detailed Mesh Description

This chapter shows some details on the meshes used for the simulations in the report.

A.1. Body Force Method

As shown in Figure A.1, the propellers are represented as cylindrical blocks on which the source terms for the propeller body-forces are applied while the wing surface is meshed.

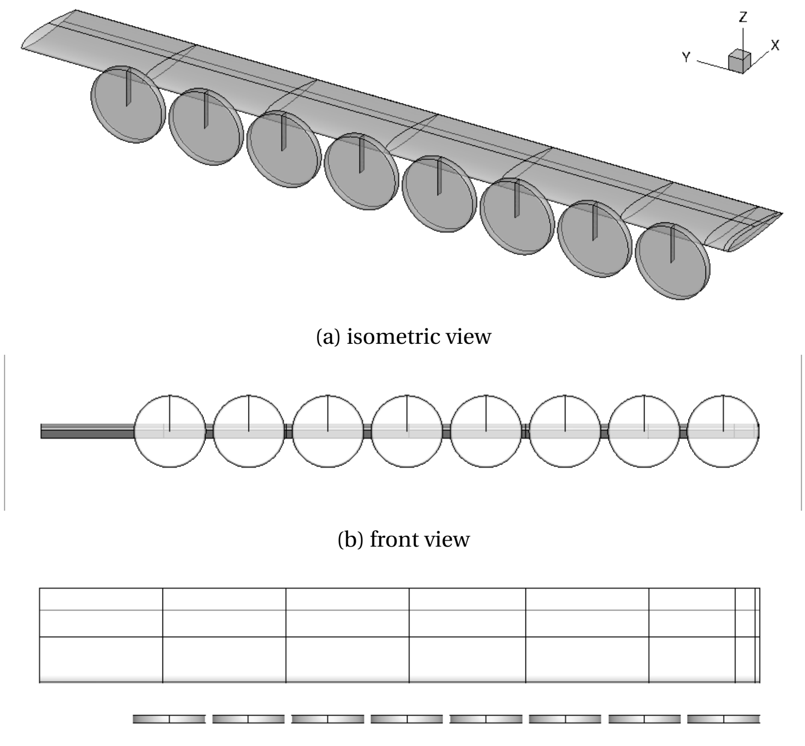

(a) isometric view

(b) front view

(c) top view

Figure A.1: Wing surface and propeller background bodies

Figure A.1 displays cuts of the merged Chimera grid for a wing-tip mounted tractor propeller. Part A.2a shows the mesh as seen from the far-field in direction of the wing-tip. The Cartesian background grid gets finer towards the parts in the center. When seen from above the wing, the grid is finer at the middle of the symmetry plane at $y = 0$ where the wing is located. A close-up of both figures can be found to their right showing how the Cartesian background grid is refined such that the cell size of the wing and propeller grid are nearly matched.

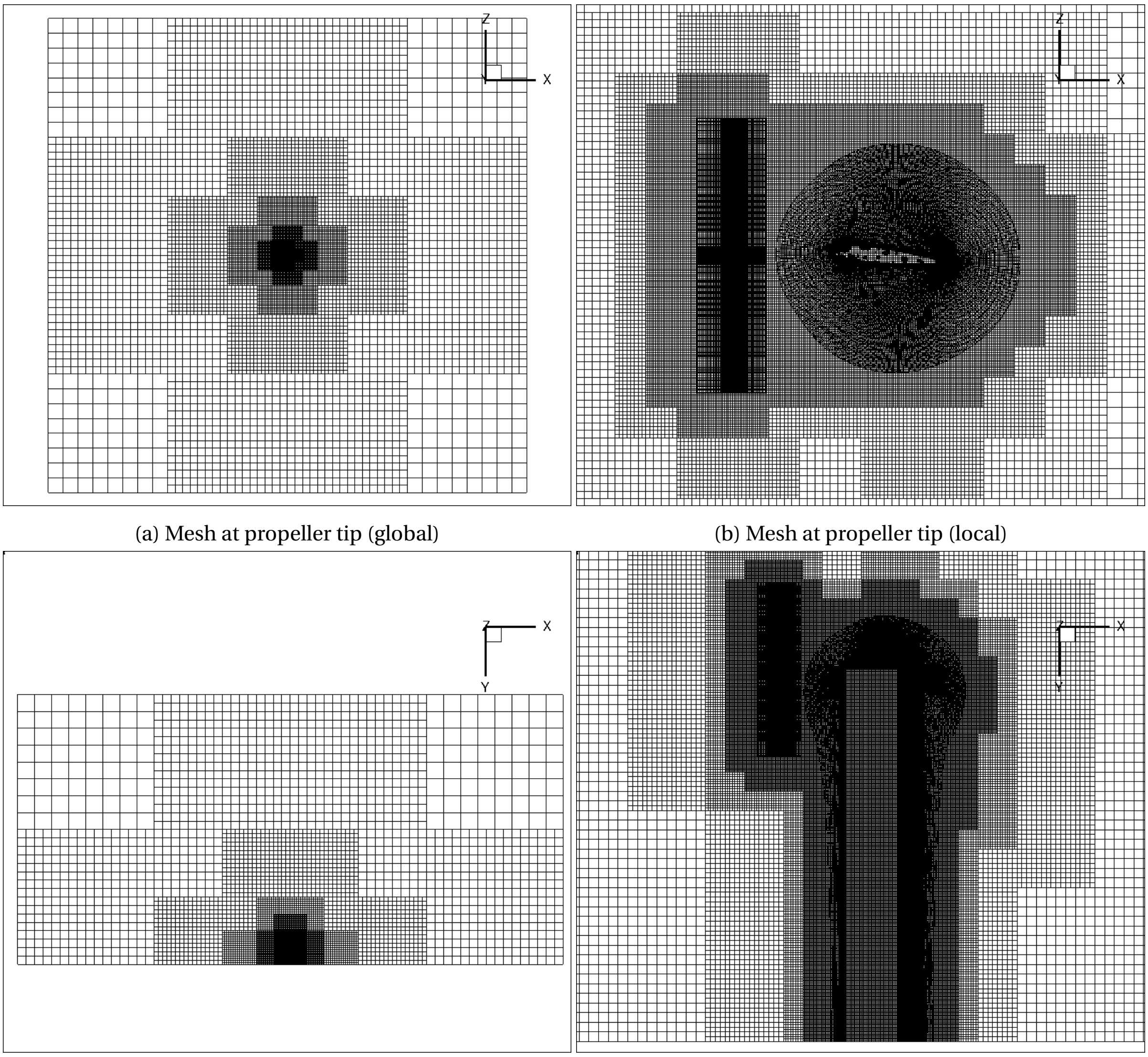

(a) Mesh at propeller tip (global) (b) Mesh at propeller tip (local)

(c) Mesh at wing surface (global) (d) Mesh at wing surface (local)

Figure A.2: Complete Chimera grid for a wing-tip mounted tractor propeller

A.1.1. BODY FORCE GRID

The cylindrical body-force grid is shown in Figure A.3. The axially refined part has a constant axial cell length and is in total slightly larger than the maximum chord of the blade. upstream and downstream the cell size increases exponentially. In radial direction, the cell size increases towards the outer blade region.

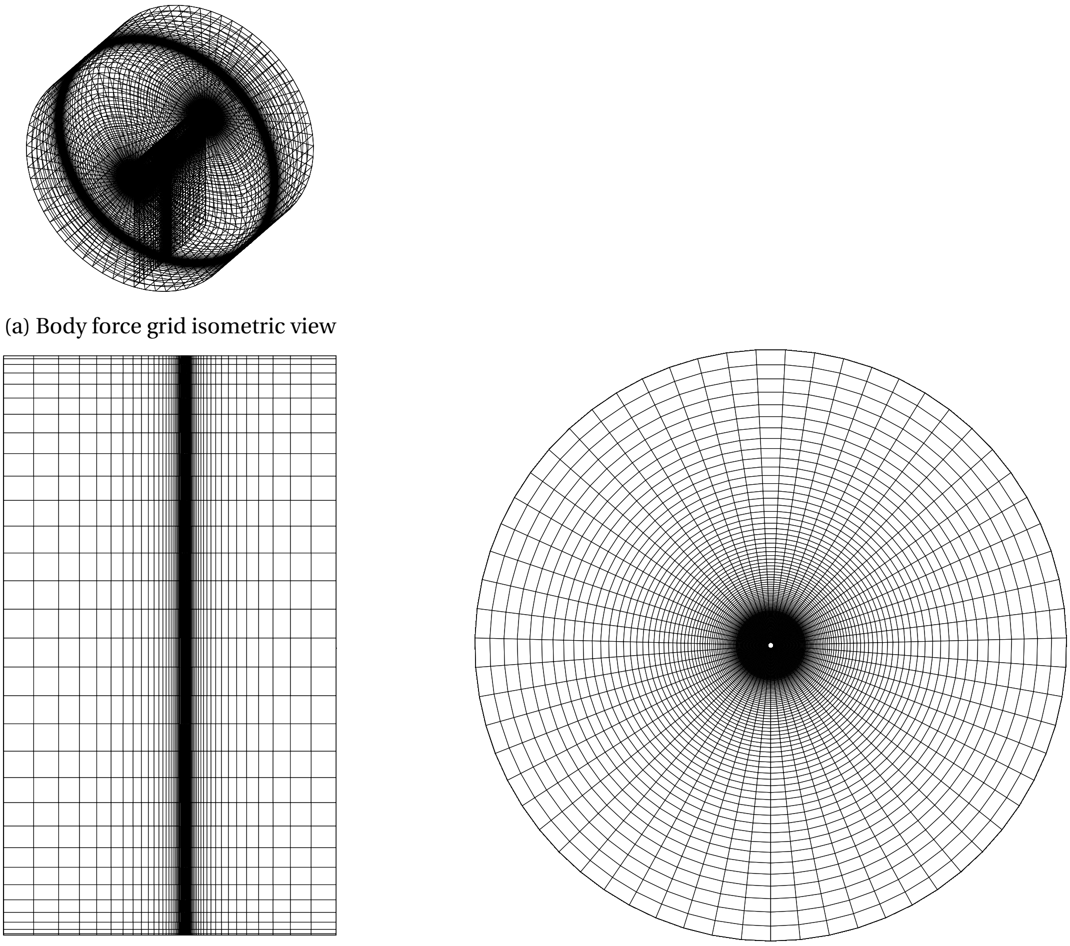

(a) Body force grid isometric view

(b) Body force grid axial view

(c) Body force grid front view

Figure A.3: Body force grid

A.1.2. BODY FORCE GRID CONVERGENCE STUDY

A convergence study was performed for the body force grid as it was not yet clear in the beginning what refinement is required to have a converged solution. The grid was refined in axial, radial and azimuthal direction separately. The global thrust and power results are compared in Tables A.1 to A.3. The values do not significantly change but it cannot be concluded from this that the roughest resolution is enough for a wing-propeller combination.

Table A.1: BF grid convergence - radial

	coarse	**intermediate**	**fine**
$n_{nodes,radial}$ [-]	32	64	128
$n_{nodes,azimuthal}$ [-]	64	64	64
$n_{nodes,axial}$ [-]	64	64	64
C_T [-]	0.1957	0.1957	0.1957
C_P [-]	0.4159	4161	0.4160

Table A.2: BF grid convergence - azimuthal

	coarse	intermediate	fine
$n_{nodes,radial}$ [-]	64	64	64
$n_{nodes,azimuthal}$ [-]	32	64	128
$n_{nodes,axial}$ [-]	64	64	64
C_T [-]	0.1957	0.1957	0.1957
C_P [-]	0.4160	0.4161	0.4161

Table A.3: BF grid convergence - axial

	coarse	intermediate	fine
$n_{nodes,radial}$ [-]	64	64	64
$n_{nodes,azimuthal}$ [-]	64	64	64
$n_{nodes,axial}$ [-]	32	64	96
C_T [-]	0.1957	0.1957	0.1957
C_P [-]	0.4165	0.4161	0.4157

For having no influence of the background grid on the solution also the induced velocities have to be converged. For this, the axial and tangential induced velocities at three different axial distances from the quarter chord line are compared in Figures A.4 to A.9. From these comparisons it is concluded that 64 radial points, 64 azimuthal points and 32 axial points are sufficient to have grid convergence.

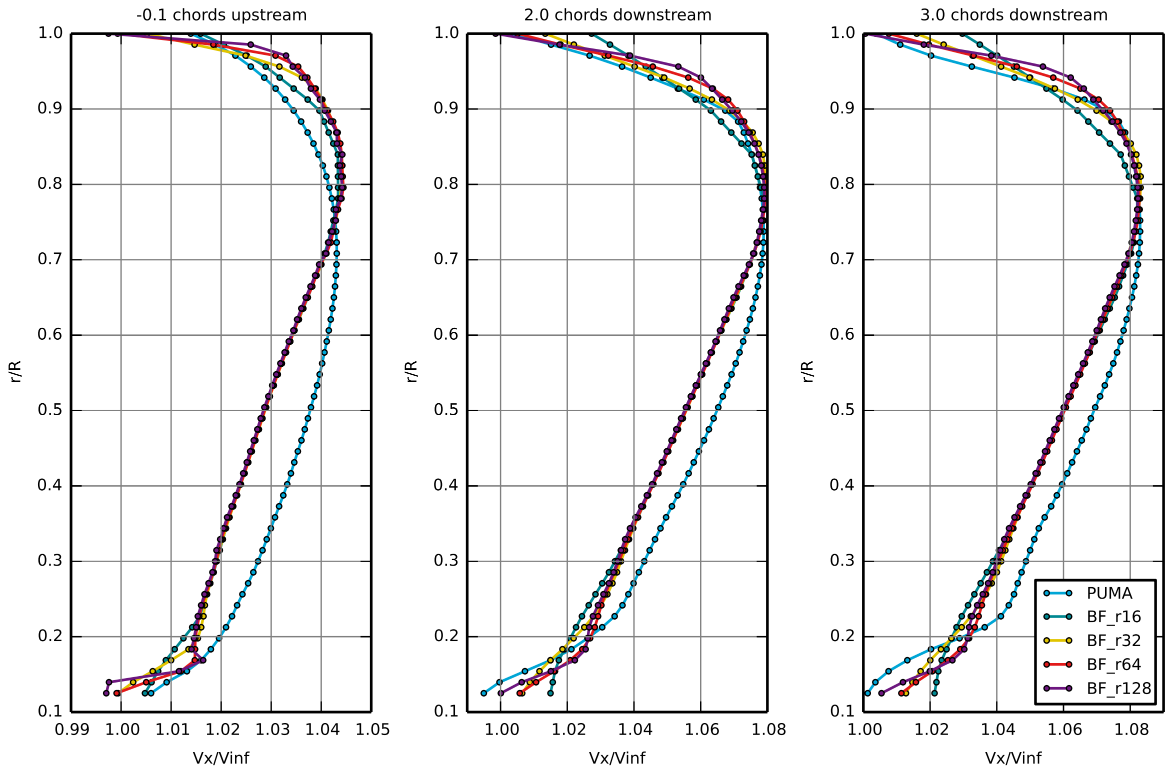

Figure A.4: Body force grid convergence study for radial fineness (axial velocity profiles at different axial stations)

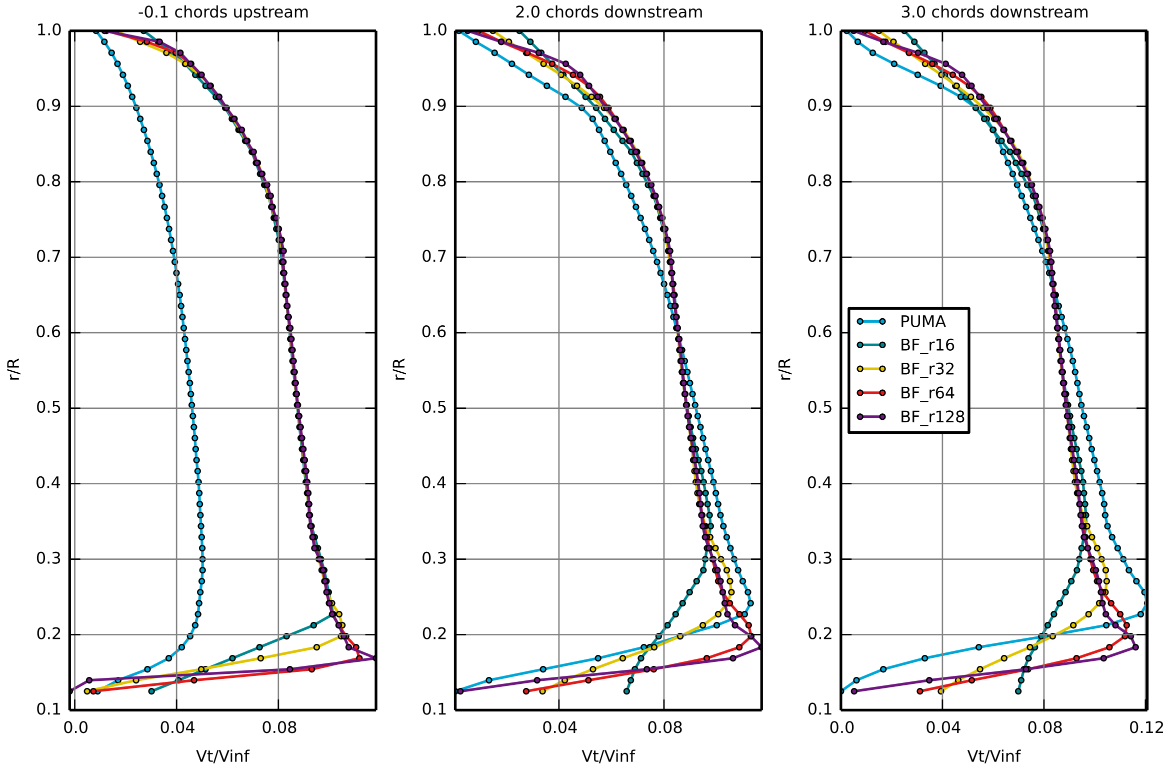

Figure A.5: Body force grid convergence study for radial fineness (tangential velocity profiles at different axial stations)

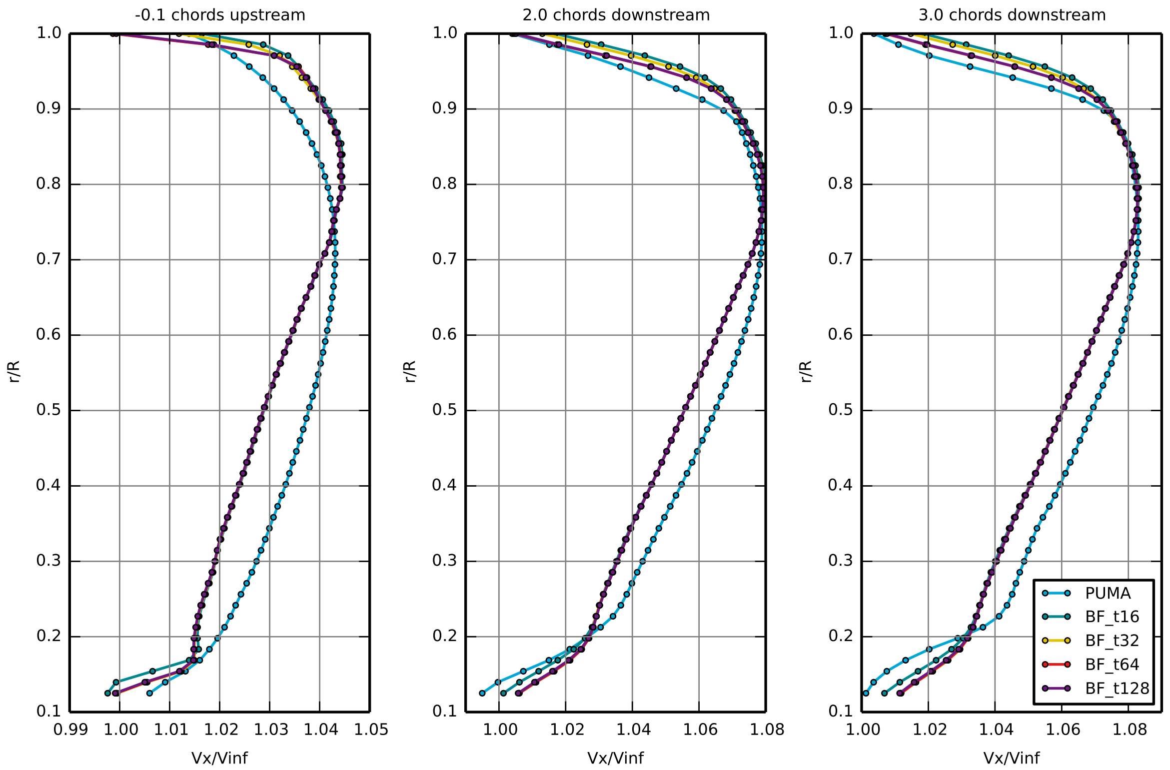

Figure A.6: Body force grid convergence study for azimuthal fineness (axial velocity profiles at different axial stations)

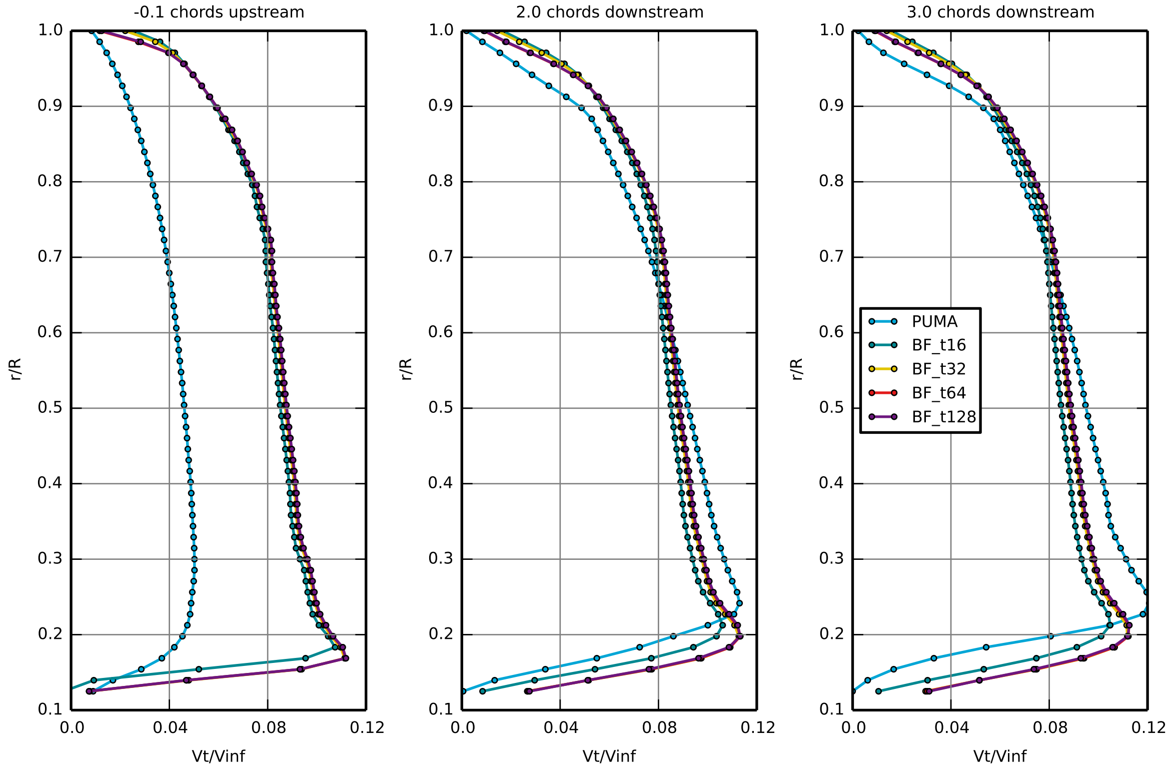

Figure A.7: Body force grid convergence study for azimuthal fineness (tangential velocity profiles at different axial stations)

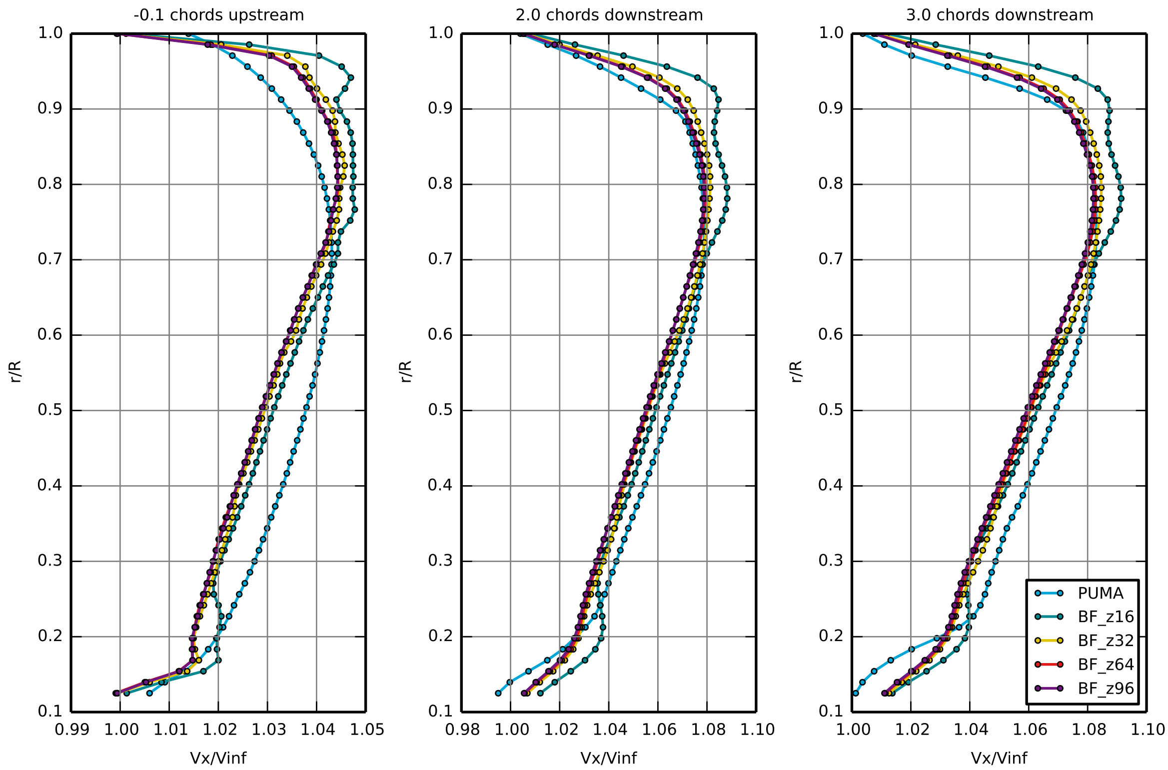

Figure A.8: Body force grid convergence study for axial fineness (axial velocity profiles at different axial stations)

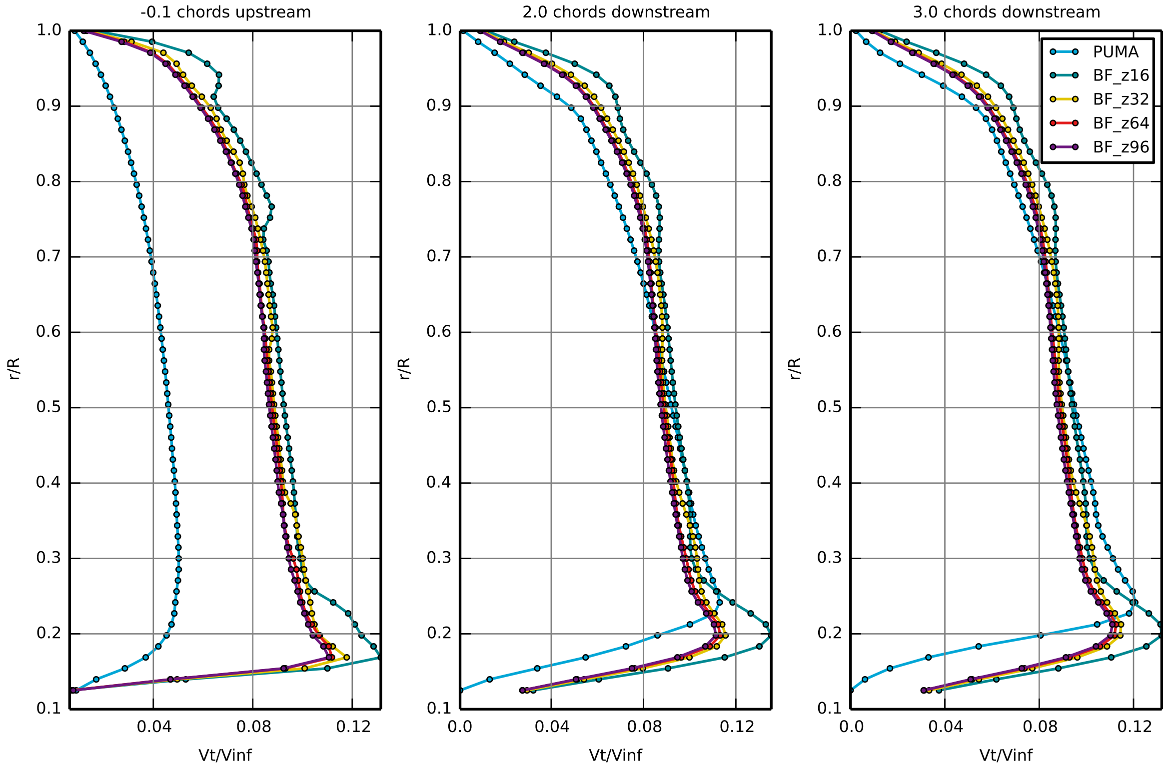

Figure A.9: Body force grid convergence study for axial fineness (tangential velocity profiles at different axial stations)

A.2. WING GRID

Figure A.10 shows a span-wise section cut through the wing grid. The presented mesh corresponds to the untwisted wing used for the wing-tip mounted propeller configurations. Figure A.11 shows an isometric view of the entire grid.

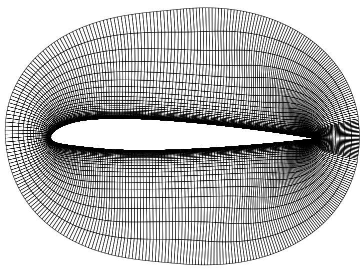

Figure A.10: Wing grid span-wise slice

Figure A.11: Global wing grid view

To make sure that the wing grid is fine enough to resolve the boundary layer's behaviour, the y_+ values are plotted at span-wise section $2y/b = 0.25$. Clearly, the value stays below 1 at all time such that the first grid layer is considered small enough.

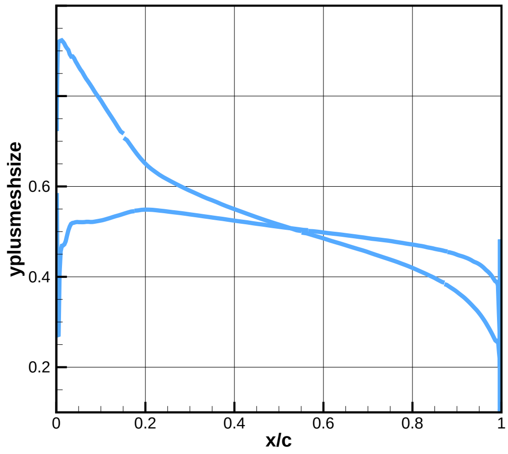

Figure A.12: y+ values at wing quarter span

A.3. PROPELLER BLADE GRID

The propeller gird as shown in Figure A.13 is presented for the minimum induced loss propeller as used as wing-tip propellers in the report. The wing surface mesh, the individual blocks and a radial section cut are indicated.

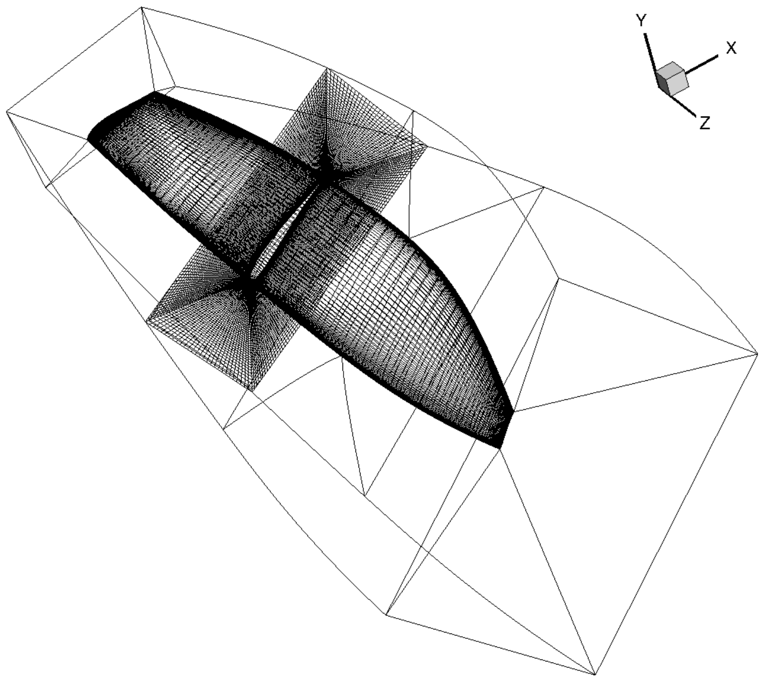

Figure A.13: Propeller blade grid

A.4. EXPERIMENTAL SET-UP GRIDS

The validation of the body-force approach includes a comparison to an over-the-wing mounted propeller. In Chapter 5, the composition of the Chimera grid was presented. Additionally, this section shows details on the individual component grids. The grids for the nacelle and the sting are presented. The wing grid is similar to the one presented above apart from its airfoil shape and is, hence, not shown individually. The same holds for the body-force grid.

A.4.1. NACELLE GRID

The nacelle grid is shown in Figure A.14. The body-of-revolution was meshed with Pointwise. Figures A.15 and A.16 show and axial cut and a cross-section cut of the mesh.

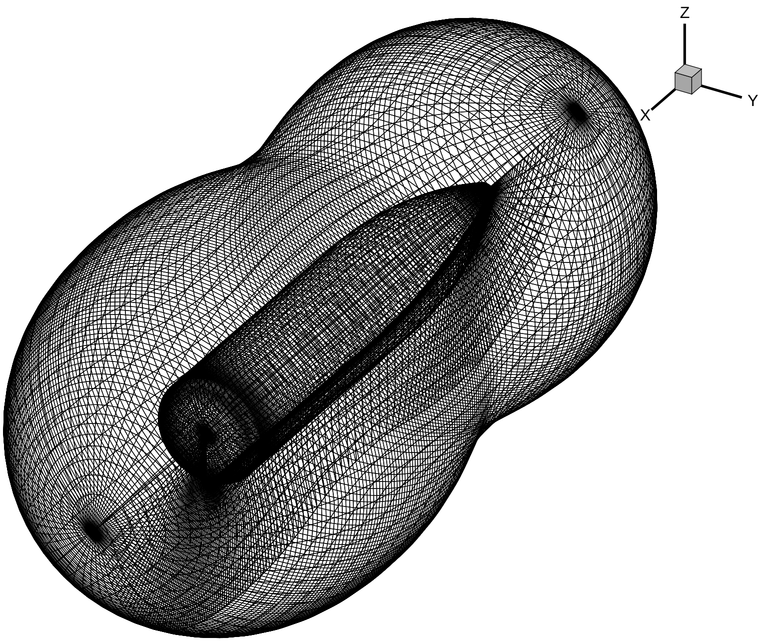

Figure A.14: Nacelle grid iso-view

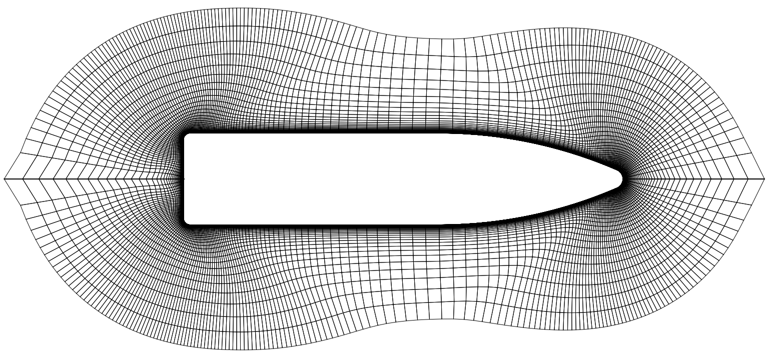

Figure A.15: Nacelle grid constant y cut

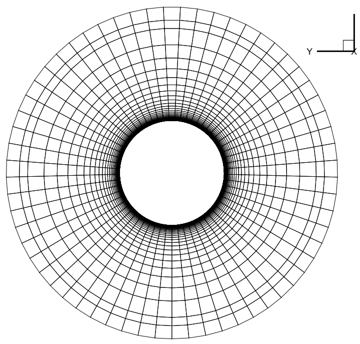

Figure A.16: Nacelle grid constant x cut

A.4.2. STING GRID

The sting grid was meshed with Pointwise and is shown in Figure A.17. It was meshed similarly to the wing grid but instead of fixing a constant y for the most inboard nodes, this time the inner nodes were forced to follow the nacelle contour.

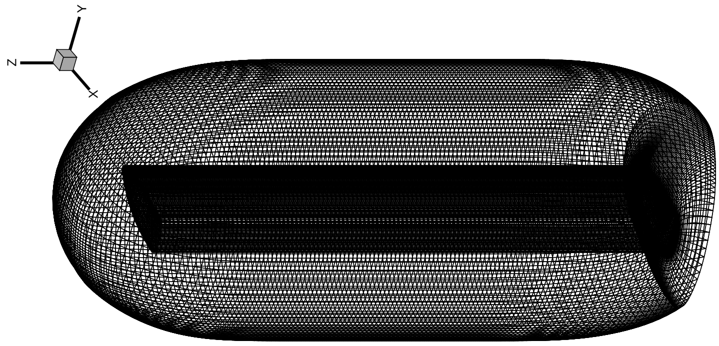

Figure A.17: Sting grid iso-view

The nacelle fitting can be seen on the left side of Figure A.18. Figure A.19 shows a span-wise section cut.

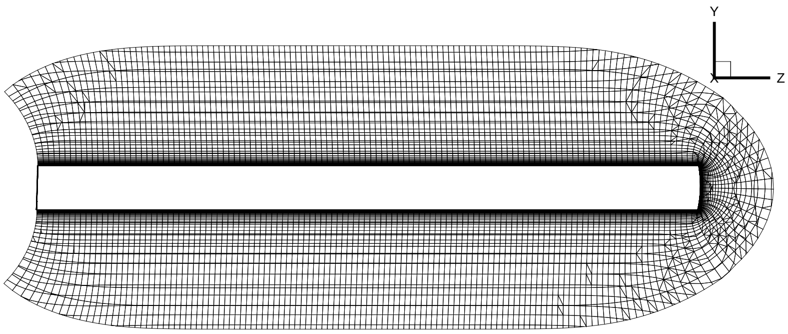

Figure A.18: Sting grid constant x cut

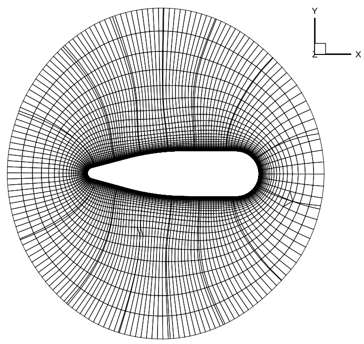

Figure A.19: Sting grid constant z cut

B
ADDITIONAL RESULTS

B.1. VALIDATION

The angle-of-attack map of the PROWIM propeller model mounted above the wing is shown in Figure B.1. The increased speed close to the wing surface clearly leads to a reduction in blade loading between 0 and 180 degrees.

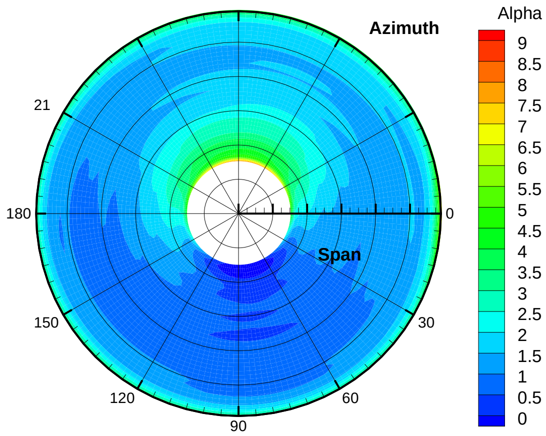

Figure B.1: propeller angle of attack map (α in degrees)

The axial velocity contours around the configuration is depicted in Figure B.2. The hole in the wing as well as the partially covered stagnation in front of the nacelle is a visualisation error because of the blanking process. Clearly, wing, nacelle, sting and propeller strongly interact with each other. The propeller operates in the high velocity region of the wing and interacts with its wake. The nacelle is close to the wing and forms a channel with the wing. The sting interacts with the nacelle as well as with the slipstream.

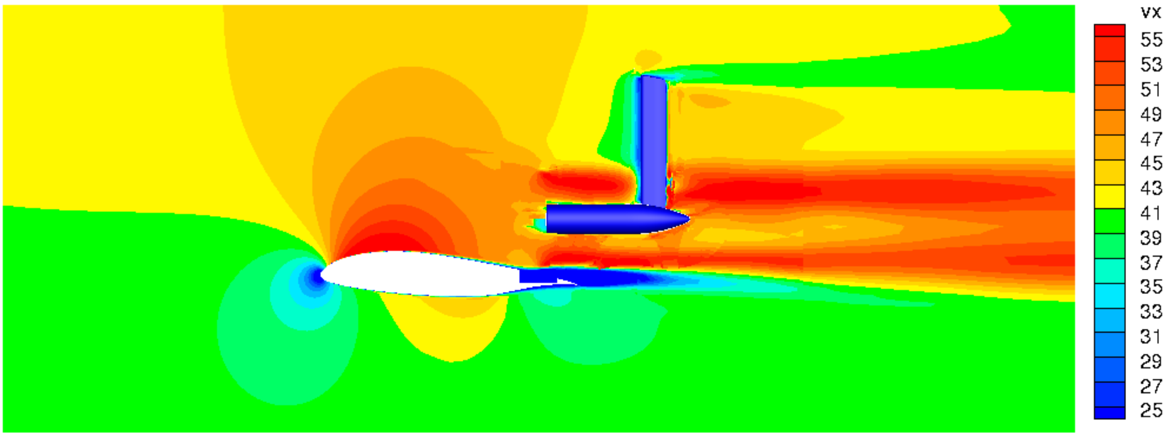

Figure B.2: Velocity field at constant y at the propeller center line (v_x in m/s)

B.2. WING-TIP PROPELLER

Additional results for the simulations in Section 6.1 are presented in this section for the interested reader.

B.2.1. BODY-FORCE SIMULATION

The upper wing surface pressure contours are shown for the isolated wing as well as for the pusher & tractor configurations in Figure B.3. Little difference can be observed for the pusher configuration but the tractor shows a clear increase in suction close to the tip being strongest behind the highest loaded blade sections of the propeller.

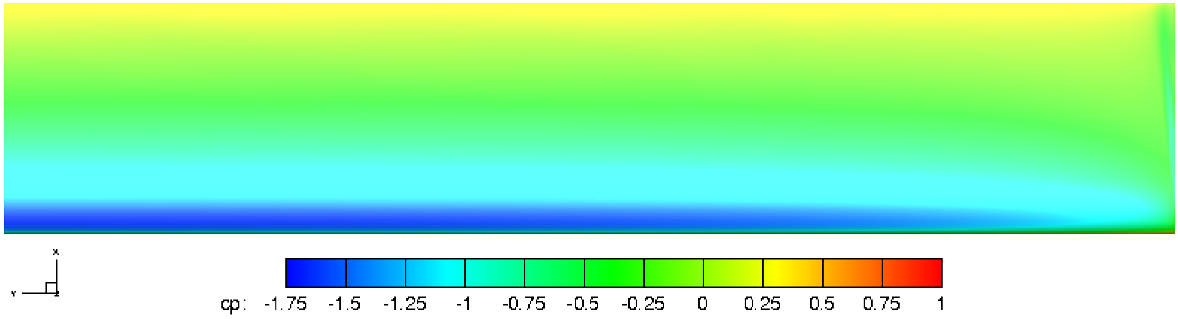

(a) isolated wing

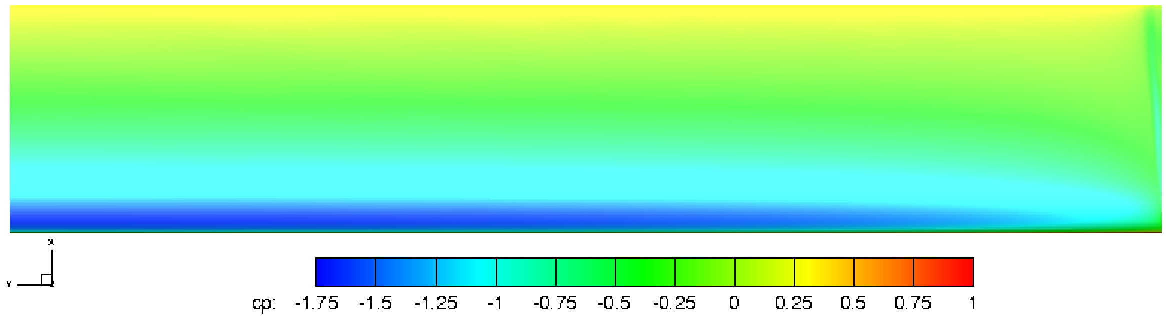

(b) Pusher configuration

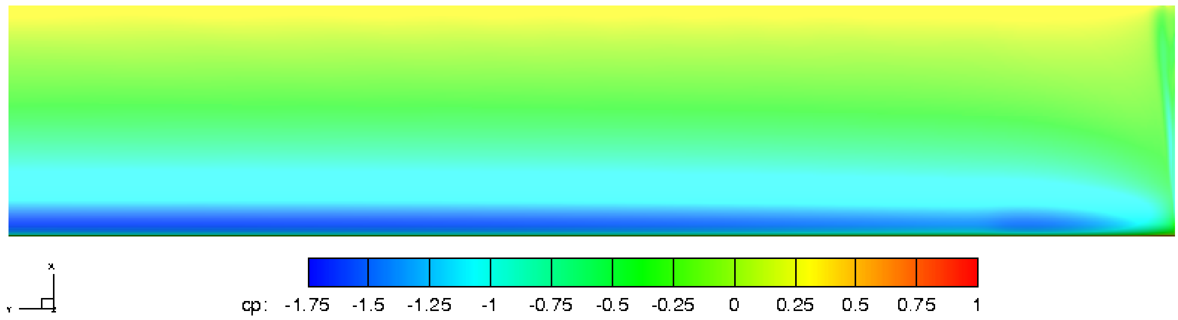

(c) Tractor configuration

Figure B.3: Pressure distribution over the wing upper surface for untwisted wing with tip pusher/tractor (SL+0, $M = 0.3$, $T = D_{ac}$, $D_{ac-w} = 924$N, $C_L = 0.6$, $M_{tip} = 0.5$)

Figures B.4 to B.6 show the axial vorticity and total pressure contours behind the three different cases. Clearly, the wakes of the propeller and the wing interact with each other. However, it can be noticed that due to the weak loading at the wing tip, no significant shearing of the propeller slipstream occurs for the tractor propeller. Additionally, the vorticity stemming from the isolated wing is reduced in strength when installing a pusher or tractor propeller. Also the total pressure loss close to the wing-tip is compensated by installing wing-tip mounted propellers.

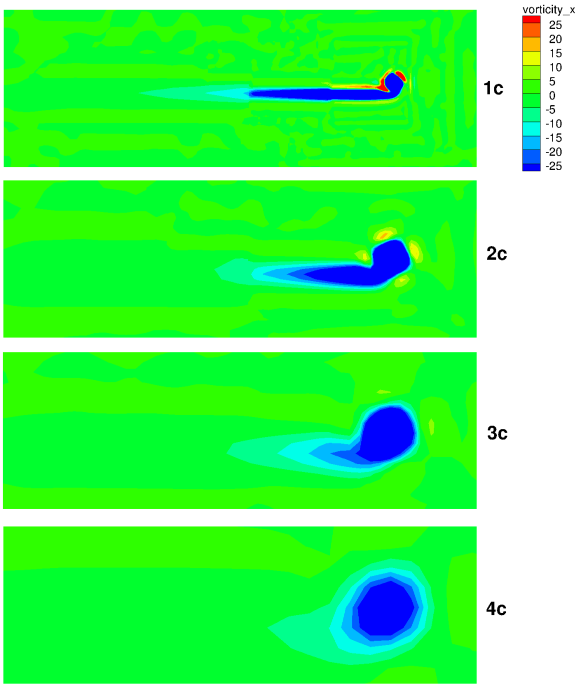

(a) Axial vorticity contours at 1-4 chord lengths behind the wing trailing edge

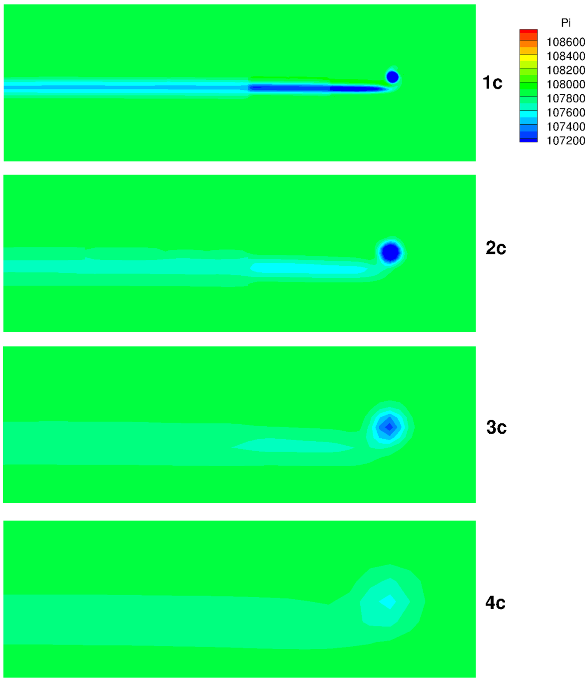

(b) Total pressure contours at 1-4 chord lengths behind the wing trailing edge

Figure B.4: Axial vorticity & total pressure contours behind the isolated wing for untwisted wing (ω_x in s^{-1}, p_t in Pa, SL+0, $M = 0.3$, $C_L = 0.6$)

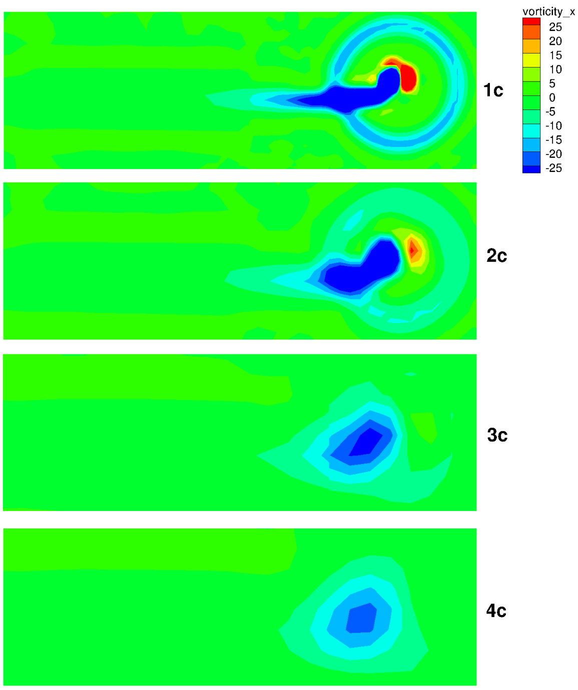

(a) Axial vorticity contours at 1-4 chord lengths behind the wing trailing edge

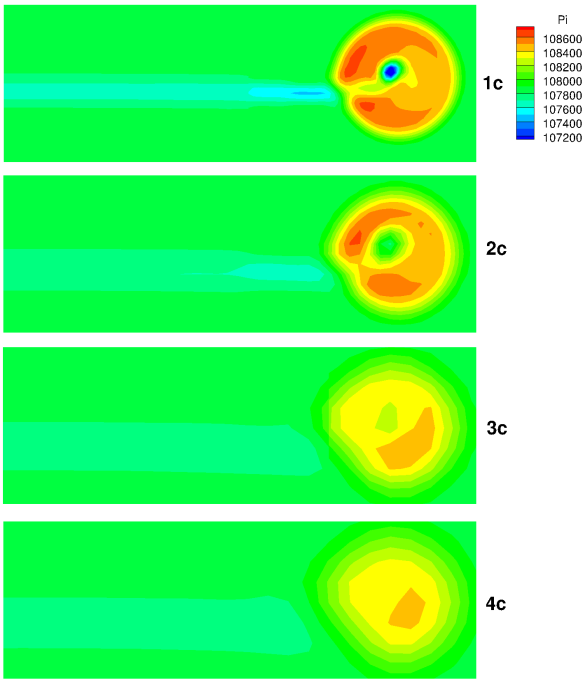

(b) Total pressure contours at 1-4 chord lengths behind the wing trailing edge

Figure B.5: Axial vorticity & total pressure contours behind the pusher configuration for untwisted wing (ω_x in s^{-1}, p_t in Pa, SL+0, $M = 0.3$, $T = D_{ac}$, $D_{ac-w} = 924$N, $C_L = 0.6$, $M_{tip} = 0.5$)

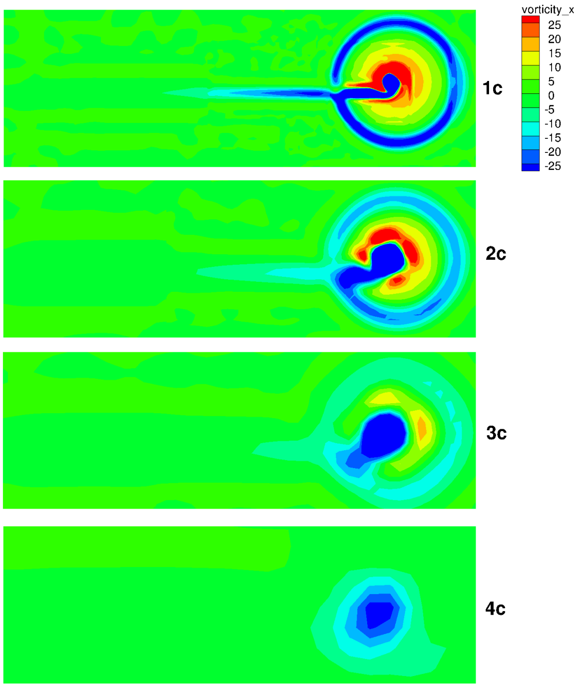

(a) Axial vorticity contours at 1-4 chord lengths behind the wing trailing edge

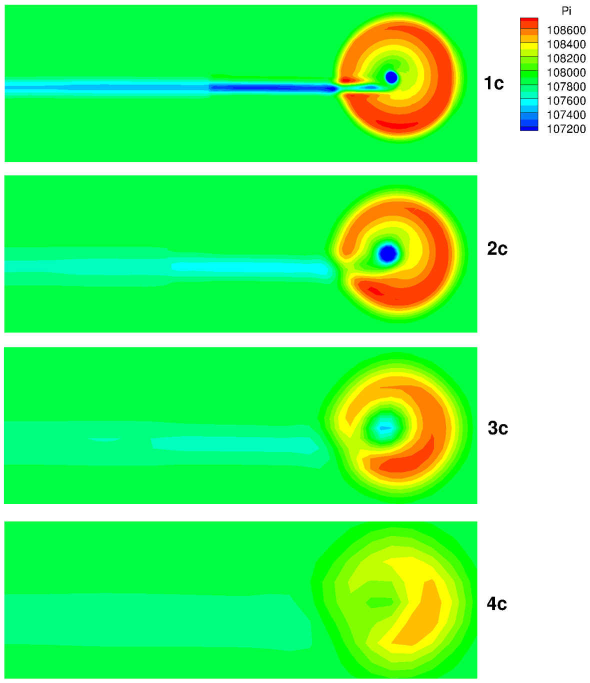

(b) Total pressure contours at 1-4 chord lengths behind the wing trailing edge

Figure B.6: Axial vorticity & total pressure contours behind the tractor configuration for untwisted wing (ω_x in s^{-1}, p_t in Pa, SL+0, $M = 0.3$, $T = D_{ac}$, $D_{ac-w} = 924$N, $C_L = 0.6$, $M_{tip} = 0.5$)

B.2.2. PARAMETRIC STUDY WITH PUMA

A parametric study was performed with the lifting-line code to assess the sensitivity of the drag reduction and propeller efficiency on different design parameters. This is done because the lifting-line code is a relatively fast means that does not require a change in meshing etc. to assess the effect of geometric changes to the geometry. This allows to identify the governing design parameters for the configuration performance. The study is performed at constant lift coefficient of 0.5 and a constant thrust coefficient of 0.114 per engine. The flight conditions and geometries are similar to those in the previous analyses.

EFFECT OF PROPELLER POSITIONING

The axial position of the propeller has a strong effect on the performance since the propeller slipstream varies significantly with stream-wise distance from the propeller disk. Additionally, the wing effect on the propeller is much stronger close to the wing. Figure B.7 shows the changes in drag and propeller efficiency with changing axial propeller distance from the wing. The tractor propeller shows a higher propeller efficiency close to the wing because of the higher stagnation effect of the wing. The drag reduction, however, is less strong because the slipstream axial velocity is less close to the propeller disk. The pusher configuration, on the other hand, has a lower drag when being closely coupled and also shows a slightly lower increase in propeller efficiency.

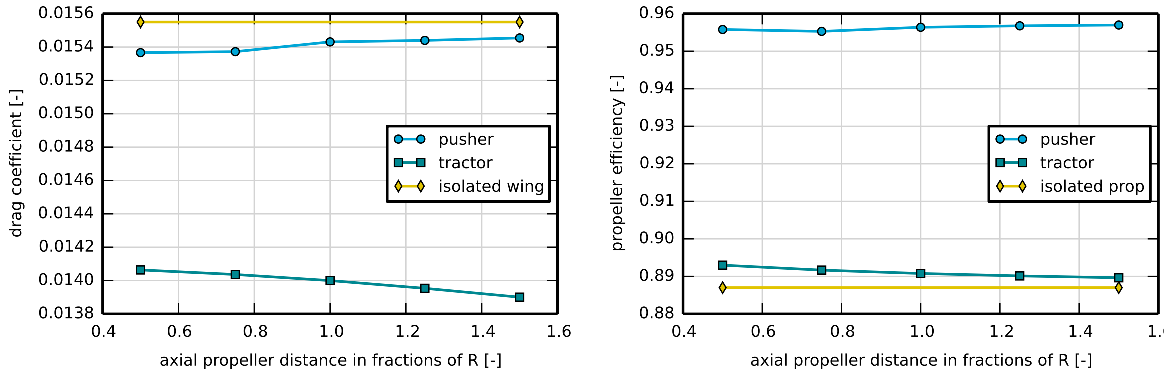

(a) Effect on drag

(b) Effect on propeller efficiency

Figure B.7: Sensitivity of wing drag and propeller efficiency to the axial propeller position

EFFECT OF PROPELLER LOADING

The propeller thrust coefficient also has a strong effect on the performance. A stronger loaded tractor propeller has a higher slipstream velocity in tangential direction and therefore further reduces wing drag. The higher axial velocity increases wing drag and lift but due to the lift trim, the angle of attack is lowered and both values are reduced again leaving the tangential flow effect as the governing phenomenon. The propeller efficiency slightly decreases but much less when compared to the isolated propeller. This may be attributed to the inflow swirl lowering the required pitch setting thus postponing the performance drop at higher thrust levels. The pusher configuration has a lower drag coefficient for a higher loaded propeller which may be a result of a higher dynamic pressure over the wing tip, allowing a lower angle of attack for the same lift coefficient. The propeller performance deteriorates less significantly than for the isolated propeller, as even for higher propeller settings, the inflow swirl augments the thrust strongly.

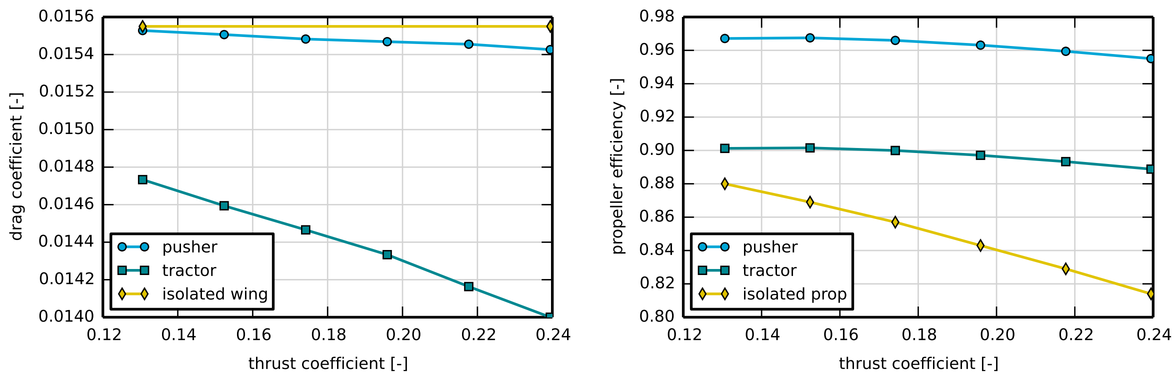

(a) Effect on drag

(b) Effect on propeller efficiency

Figure B.8: Sensitivity of wing drag and propeller efficiency to the propeller thrust

EFFECT OF PROPELLER SIZING

The size of the propeller has a strong influence because of the relative size with respect to the wing. The slipstream of a larger propeller washes over a larger portion of the wing tip. Hence, a larger tractor propeller also has a higher potential to reduce the drag coefficient. However, if the propeller loading is weak and the swirl component diminishes because the thrust is kept constant, this is not the case any more. This behaviour can also be observed in Figure B.9. On the other hand, the larger propeller has a higher efficiency for pusher and tractor configurations which is not the case for the isolated propeller.

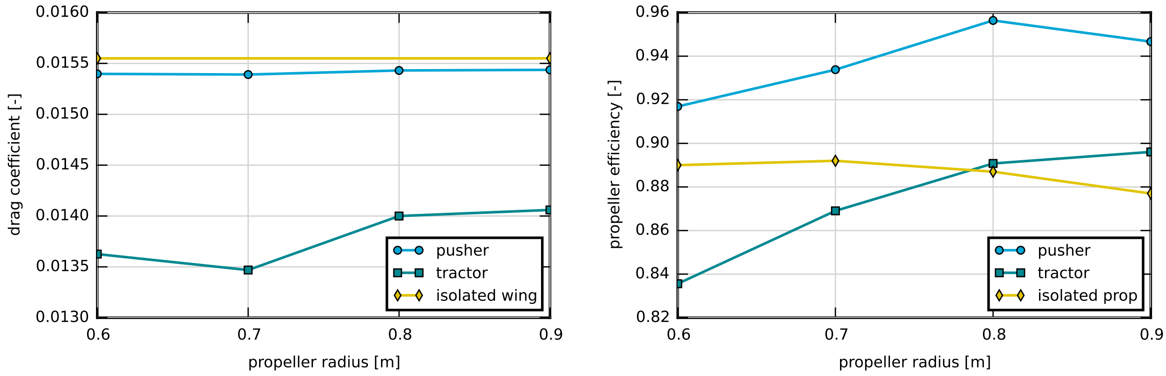

(a) Effect on drag

(b) Effect on propeller efficiency

Figure B.9: Sensitivity of wing drag and propeller efficiency to the propeller radius

EFFECT OF APECT RATIO

The increase in aspect ratio shows the effect of reduced washed wing surface for the tractor case as well as a lower propeller inflow swirl for the pusher case. The reduced inflow swirl leads to a strong decrease in propeller efficiency mounted on higher-aspect ratio wings. All cases have a reduced drag coefficienct as can be expected from higher aspect ratio wings but no clear distinguishable effects can be observed for the different variants.

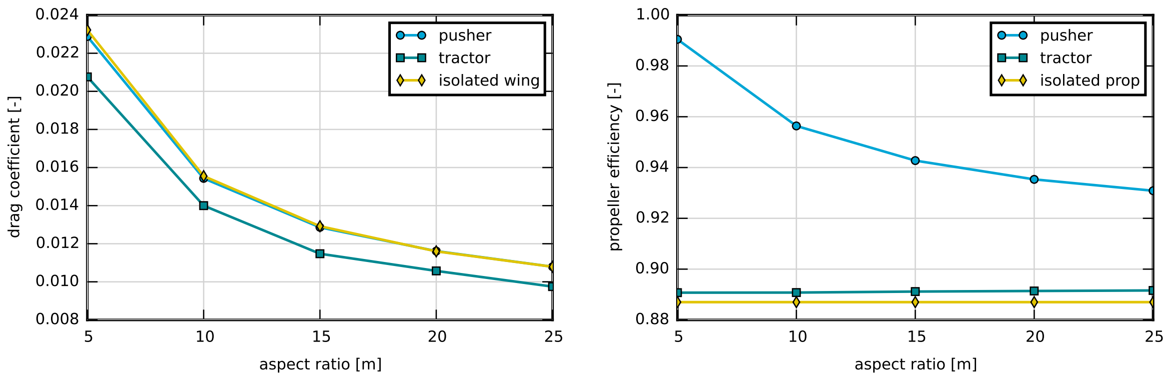

(a) Effect on drag

(b) Effect on propeller efficiency

Figure B.10: Sensitivity of wing drag and propeller efficiency to the wing aspect ratio

EFFECT OF TAPER

The taper ratio of the wing is the last variable that was changed to see its effect on the configuration. Apparently, a taper ratio of roughly 0.4 leads to the lowest wing drag in all cases. This may be attributed to the fact that this geometry comes closest to an elliptic lift distribution. The effect on pusher propeller efficiency, however, is monotonically increasing with higher taper ratio. The less elliptic lift distribution of a wing with high taper ratio wings results in a stronger wing-tip vortex or more beneficial inflow swirl for the propeller.

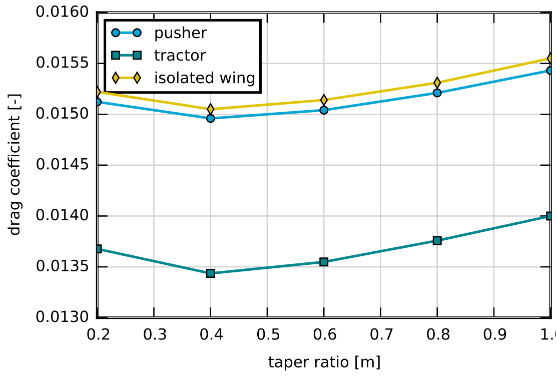

(a) Effect on drag

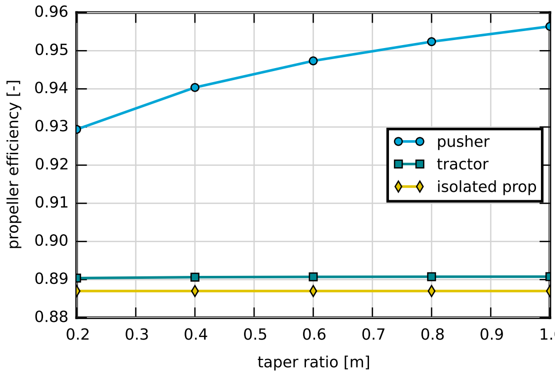

(b) Effect on propeller efficiency

Figure B.11: Sensitivity of wing drag and propeller efficiency to the wing taper ratio

B.3. HIGH-LIFT PROPELLERS

In this section, further results for the simulations presented in Section 6.2 are shown.

B.3.1. LEADING-EDGE PROPELLERS

The wing pressure distributions for the different senses of rotation are are shown in Figure B.12. Additionally, the axial vorticity and total pressure contours behind the configurations are shown in Figure B.13. While for the co-rotating propellers the wing pressure distribution periodically shows peaks at every section behind an up-going blade, the contra-rotation leads to a merging of the suction peaks leading to a stronger maximum suction as has been seen in Section 6.2. Also, the suction regions are deformed by this interaction and are not as uniform as for the contra-rotating case.

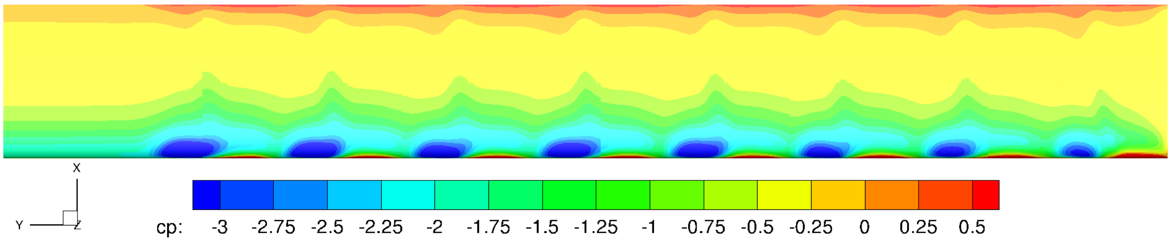

(a) Co-rotating

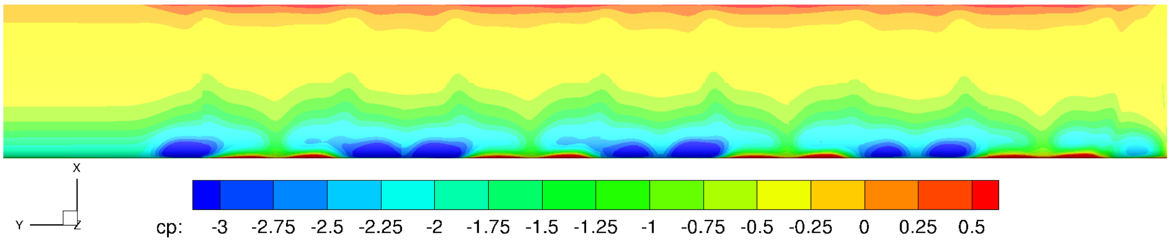

(b) Contra-rotating

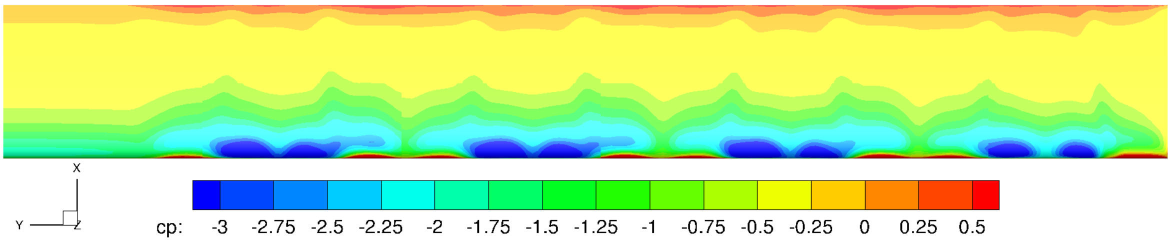

(c) Contra-rotating2

Figure B.12: Pressure distribution over the wing upper surface for leading-edge mounted high-lift propellers with different senses of rotation (propeller aligned with free steam, $\alpha = 5.5$ deg, $N_p = 16$, $T/A = 1000\ \mathrm{N/m^2}$)

The wakes of the distributed propellers merge and deform strongly in all cases. A difference can be made between the total pressure fields that shows a continuous high total pressure band for the co-rotating propellers while the counter-rotating case leads to individual high total pressure regions of two merged slipstreams each.

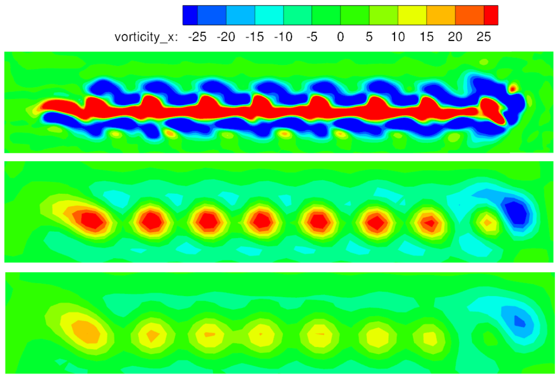

(a) Axial vorticity contour (co-rotating)

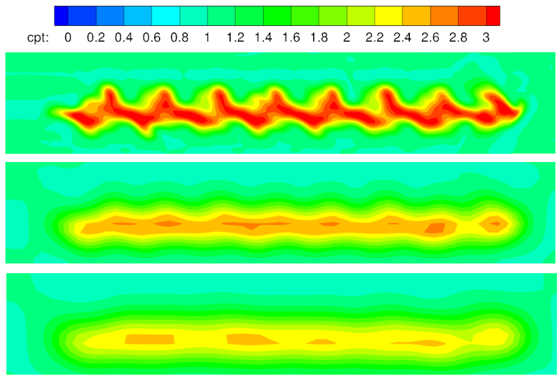

(b) Total pressure contour (co-rotating)

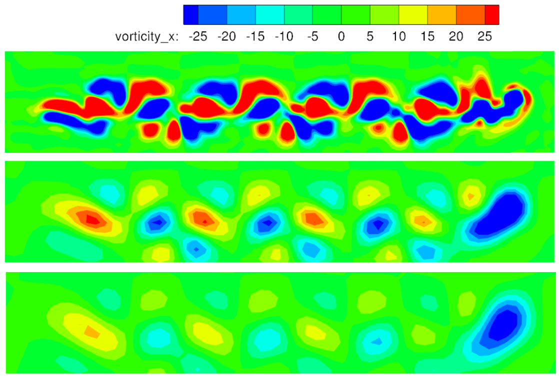

(c) Axial vorticity contour (counter-rotating)

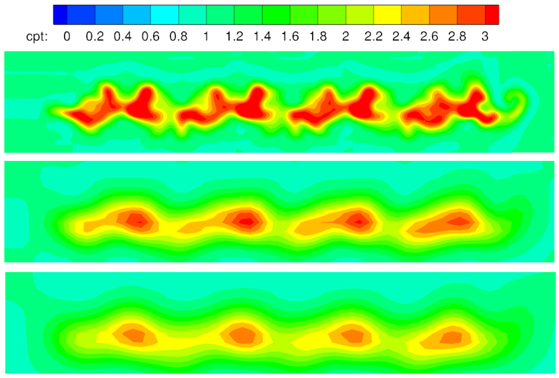

(d) Total pressure contour (counter-rotating)

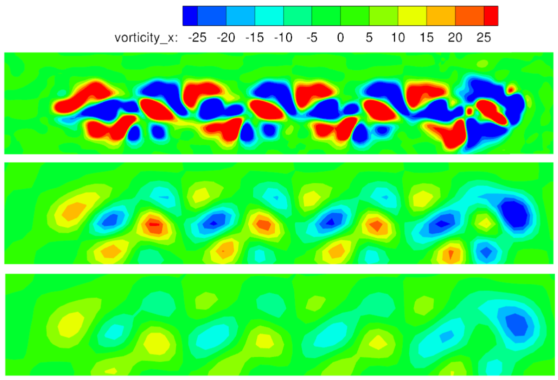

(e) Axial vorticity contour (counter-rotating2)

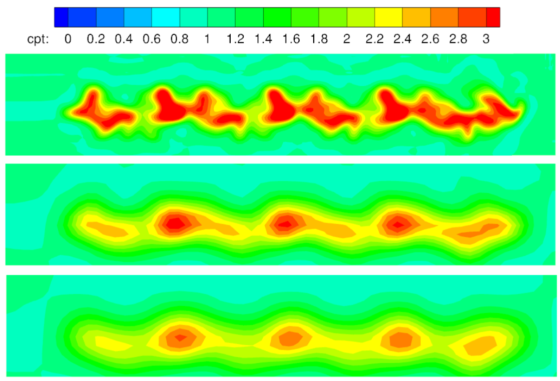

(f) Total pressure contour (counter-rotating2)

Figure B.13: Axial vorticity and total pressure contours downstream of the wing for leading-edge mounted high-lift propellers with different senses of rotation (propeller aligned with free steam, ω_x in s^{-1}, C_{p_t} dimensionless, $\alpha = 5.5$ deg, $N_p = 16$, $T/A = 1000$ N/m^2)

B.3.2. OVER-THE-WING PROPELLERS

The axial vorticity contours and total pressure contours of the over-the-wing configurations are shown in Figure B.14. The slipstreams, in this case, are not largely deformed as could be expected since the slipstreams do not directly impinge on the wing and can simply travel downstream. However, it can be seen that the more aft-mounted propellers result in less vorticity and less total pressure in the wake. This is a direct result of the much higher efficiency of the aft-mounted propeller with lower induced velocities.

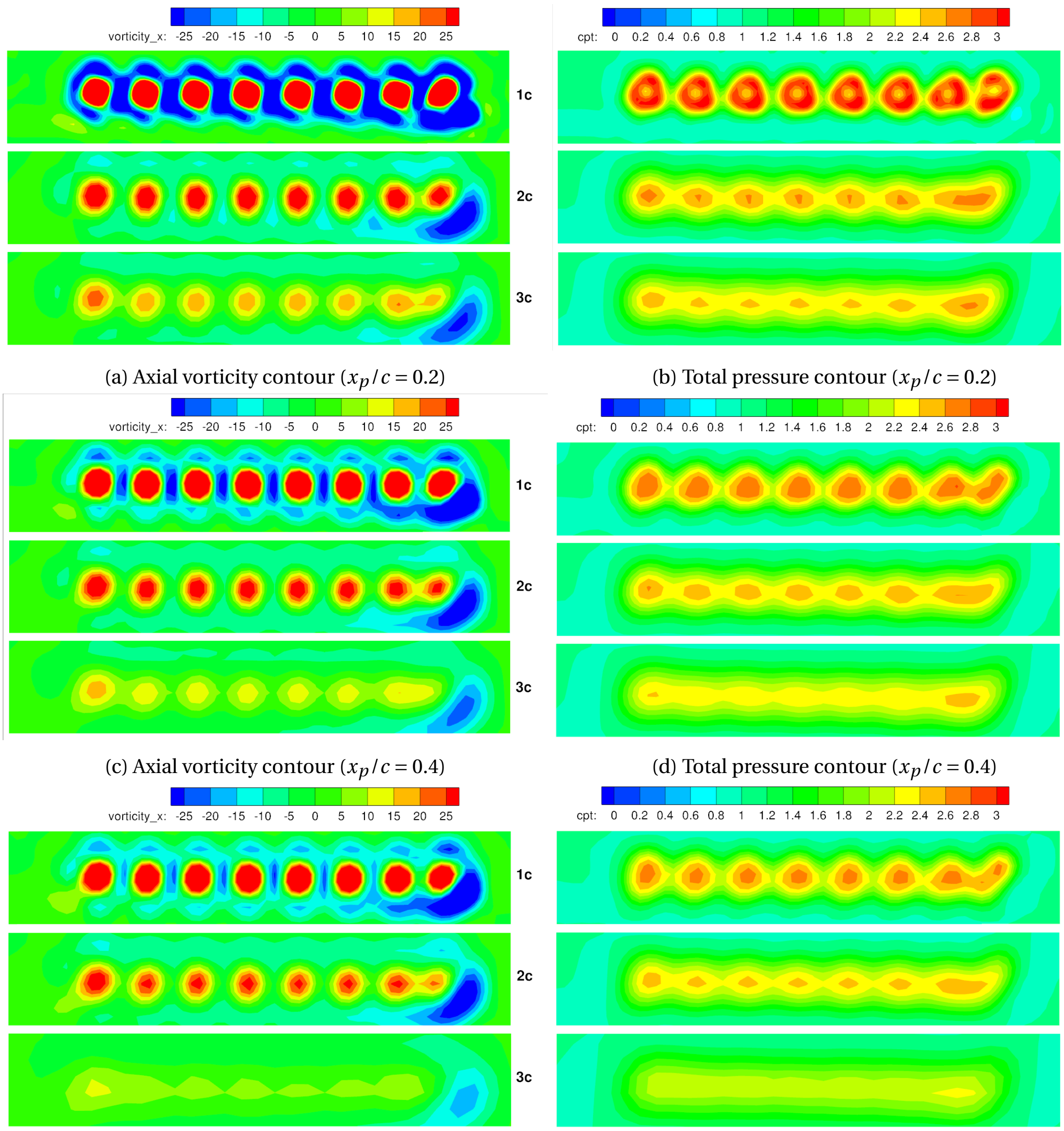

(a) Axial vorticity contour ($x_p/c = 0.2$)

(b) Total pressure contour ($x_p/c = 0.2$)

(c) Axial vorticity contour ($x_p/c = 0.4$)

(d) Total pressure contour ($x_p/c = 0.4$)

(e) Axial vorticity contour ($x_p/c = 0.6$)

(f) Total pressure contour ($x_p/c = 0.6$)

Figure B.14: Axial vorticity and total pressure contours downstream of the wing for over-the-wing mounted high-lift propellers (propeller aligned with free steam, $\alpha = 5.5$ deg, $N_p = 16$, $T/A = 1000\ \mathrm{N/m^2}$)